47

RECEIVED
APR 22 1998
OSTI

IS-T-1821

X-ray Resonant Exchange Scattering of Rare-earth Nickel Borocarbides

by

Detlefs, Carsten

PHD Thesis submitted to Iowa State University

Ames Laboratory, U.S. DOE
Iowa State University
Ames, Iowa 50011

Date Transmitted: October 8, 1997

PREPARED FOR THE U.S. DEPARTMENT OF ENERGY
UNDER CONTRACT NO. W-7405-Eng-82.

DISCLAIMER

This report was prepared as an account of work sponsored by an agency of the United States Government. Neither the United States Government nor any agency thereof, nor any of their employees, makes any warranty, express or implied, or assumes any legal liability or responsibility for the accuracy, completeness or usefulness of any information, apparatus, product, or process disclosed, or represents that its use would not infringe privately owned rights. Reference herein to any specific commercial product, process, or service by trade name, trademark, manufacturer, or otherwise, does not necessarily constitute or imply its endorsement, recommendation, or favoring by the United States Government or any agency thereof. The views and opinions of authors expressed herein do not necessarily state or reflect those of the United States Government or any agency thereof.

This report has been reproduced directly from the best available copy.

AVAILABILITY:

To DOE and DOE contractors: Office of Scientific and Technical Information
P.O. Box 62
Oak Ridge, TN 37831

prices available from: (615) 576-8401
FTS: 626-8401

To the public: National Technical Information Service
U.S. Department of Commerce
5285 Port Royal Road
Springfield, VA 22161

TABLE OF CONTENTS

LIST OF TABLES

LIST OF FIGURES

1 INTRODUCTION

The purpose of this thesis is to investigate the systematics of the microscopic magnetic order within a series of isostructural compounds and, at the same, to develop the relatively young experimental method of x-ray resonant exchange scattering (XRES) [Nam85, Gib88, Isa89, Blu85, Han88, Car95, Mat94a].

This technique utilizes x-ray absorption edges to obtain large enhancements of the magnetic scattering cross section. In the scattering process, an electron-core hole pair is created by electric dipolar or quadrupolar transitions and coherently recombines under emission of a photon. Although the experimental procedures for this technique are not as fully developed as for the more traditional magnetic neutron scattering techniques [Nee32, Shu49, Wil61, Moo66, Lov84], XRES can offer distinct advantages: Compared to the nonresonant magnetic x-ray scattering regime [deB81b], the resonant enhancement yields higher scattered beam intensities and better signal to noise ratios. It occurs at distinct x-ray absorption edges, where the incident photon energy equals the binding energy of a core level electron. These binding energies are element-specific so that XRES allows the separate investigation of the magnetism of sublattices associated with specific elemental constituents in compounds, alloys and multilayers. The high collimation of x-ray beams at synchrotron sources yields an order-of magnitude higher reciprocal space resolution than typical neutron experiments, and thus allows investigations over mesoscopic length scales (on the order of 0.1 μm). In cases where the natural isotopes strongly absorb neutrons, e.g. Sm, Gd and Eu, it is not necessary to perform the costly isotopic substitution. The downside, of course, is that large enhancements of the scattering at the magnetic Bragg peaks are observed at the $L_{2,3}$ and $M_{2,3,4,5}$ absorption edges only. This means that the technologically important $3d$-elements, including Mn, Fe, Co, and Ni, are not amenable to this technique, since their L-edges lie below 1 keV. The $4f$-elements, however, are ideally suitable for XRES experiments, since their L-edges lie between 5 and 11 keV, an energy regime very convenient for x-ray scattering experiments.

Traditionally, XRES has been used to measure the antiferromagnetic modulation wave vector, $\mathbf{q}$ [Gib88], the variation of its position, and intensity with temperature [Gib88]. In isolated cases, polarization analysis of the scattered beam has been used to clarify details of the scattering process [Gib91]. Attempts to separate the contributions of spin- and orbital magnetic moment [Luo93] to the $L_{2,3}$ resonant scattering, are still under way. In most earlier experiments, however, the emphasis was to develop a better understanding of the technique, and therefore the authors chose to study well known model systems. Few ab-initio magnetic structure determinations have been attempted.

In this thesis, we present XRES studies of several rare-earth nickel borocarbides, $R\mathrm{Ni_2B_2C}$. We show that XRES, similar to the neutron techniques, allows the determination of the orientation of the magnetic moment [Det96, Det97] by measuring the $\mathbf{Q}$-dependence of the scattered intensity of magnetic Bragg reflections.

As samples in this study, we chose the recently discovered [Nag94, Cav94a, Sie94a, Cav94b, Eis94] family of rare-earth nickel borocarbides, $R\mathrm{Ni_2B_2C}$, which display a wide variety of magnetic structures. Furthermore, in several of these materials, long range magnetic order coexists with superconductivity over some temperature range. The $R\mathrm{Ni_2B_2C}$ family crystallize in a body-centered tetragonal structure (space group $I4/mmm$), similar to the $\mathrm{ThCr_2Si_2}$ structure, but with an additional carbon atom in the center of the basal plane [Sie94a], as shown in Fig. 1.1. A high temperature $\mathrm{Ni_2B}$ flux growth [Can94, Cho95b] or a float zone method [Tak96] can be used to grow sizable

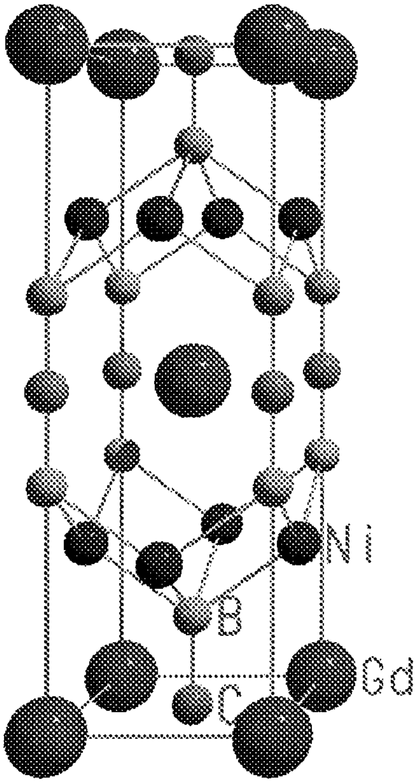

Figure 1.1 The crystal structure of the rare-earth nickel borocarbides, $R\mathrm{Ni}_2\mathrm{B}_2\mathrm{C}$. The structure is body-centered tetragonal (space group $D_{4h}^{17} = I4/mmm$) and consists of RC layers and $\mathrm{Ni}_2\mathrm{B}_2$ sheets stacked along the (0, 0, 1) direction, similar to the cuprate high-T_C superconductors. The atomic positions are: (0, 0, 0), $(\frac{1}{2}, \frac{1}{2}, \frac{1}{2})+$

R	$2a$	$(0, 0, 0)$
Ni	$4d$	$(\frac{1}{2}, 0, \frac{1}{4})$, $(0, \frac{1}{2}, \frac{1}{4})$
B	$4e$	$(0, 0, z)$, $(0, 0, \bar{z})$; $z \approx 0.36$
C	$2b$	$(\frac{1}{2}, \frac{1}{2}, 0)$

Typical lattice constants are (for $\mathrm{LuNi}_2\mathrm{B}_2\mathrm{C}$): a = 3.464 Å, c = 10.631 Å, and $z = 0.3621$ [Sie94a].

Table 1.1 Lattice parameters for the $R\mathrm{Ni}_2\mathrm{B}_2\mathrm{C}$ series at room temperature. In the rightmost column we list the boundary of the first Brillouin zone along the $\mathbf{a}^\star$ direction in units of the reciprocal lattice.

R	a (Å)	c (Å)	z	Ref.	Zone boundary ($\mathbf{a}^\star$)
Y	3.52	10.54		[Sie94a]	0.5558
La	3.79	9.86		[Sie94a]	0.5739
Ce	3.6378	10.227	0.354	[Lyn97]	0.5633
Pr	3.7066	9.999	0.352	[Lyn97]	0.5687
Nd	3.6780	10.081	0.353	[Lyn97]	0.5666
Pm					
Sm	3.62	10.24			0.5625
Eu					
Gd	3.588	10.392	0.357	[Sie94b]	0.5590
Tb	3.5536	10.435	0.357	[Lyn97]	0.5580
Dy	3.5342	10.488	0.358	[Lyn97]	0.5568
Ho	3.5177	10.528	0.359	[Lyn97]	0.5558
Er	3.5019	10.558	0.360	[Lyn97]	0.5550
Tm	3.4866	10.586	0.360	[Lyn97]	0.5540
Yb	3.4782	10.607	0.359	[Lyn97]	0.5538
Lu	3.4639	10.631	0.362	[Sie94a]	0.5531

single crystals, mostly in the form of thin platelets (typically $4 \times 3 \times 0.5$ mm^3 large) with the **c**-axis perpendicular to their flat face [Can94, Cho95b].

Systematic structure parameter refinements, based on neutron and x-ray powder diffraction data, reveal that the volume of the unit cell increases smoothly with the lanthanide radius, as does the **a**-axis lattice parameter [Sie94a, Sie94b, Lyn97] (see Table 1.1). The **c**-axis lattice parameter, on the other hand, shows an anomalous decrease with increasing R-radius[1]. This anomaly seems to be driven by strong B–C and B–Ni bonds with bond lengths that are essentially independent of the rare earth constituent of the crystal. A substitution of a smaller rare earth in the basal plane decreases the **a**-axis lattice parameter accordingly. In order to keep the aforementioned B–C and B–Ni

---

[1] The only apparent exception to this smooth variation appears to be for Ce, which did not fall on the curve unless we adjusted the radius by admixing Ce^{4+}, suggesting that this is mixed valent. Indeed, mixed valent behavior for Ce has already been suggested [Gup95, Mas95].

distances constant, the unit cell expands along the **c**-direction [Lyn97]. A similar trend is found for the lattice parameter as a function of temperature [Lyn97]

Superconductivity is observed [Cav94a, Cho95a, Cho95b, Rat96, Cho95c, Lin95, Tom95] not only for non-magnetic compounds, like $R =$ Lu ($T_C = 16.6$ K) and Y ($T_C = 15.6$ K), but also for some of the heavy rare earths with non-vanishing magnetic moment, for example $R =$ Tm ($T_C = 10.8$ K), Er ($T_C = 10.5$ K), Ho ($T_C = 8.5$ K), and Dy ($T_C = 6.2$ K). At low temperatures, these compounds display both superconductivity and long range magnetic order, while for the lighter rare earths no superconductivity above 2 K is observed. The relatively high superconducting and magnetic transition temperatures make these compounds more readily accessible to experimental studies than the previously examined $R\mathrm{Rh_4B_4}$, $R\mathrm{Mo_6S_8}$ and $R\mathrm{Mo_6Se_8}$ families of magnetic superconductors ([Fis75, She76, Fer77], for more recent overviews see [She81, Map82, Sin82, Sin84]).

Electronic band structure calculations [Pic94, Mat94b, Coe94] indicate that these materials are conventional superconductors with a relatively high density of states at the Fermi level. Mattheiss *et al.* suggested [Mat94c] that superconductivity in these systems can be attributed to a conventional electron-phonon mechanism that couples the *sp*-like conduction electrons to a high-frequency A_{1g} phonon mode in which the boron atoms move along the **c**-axis relative to the other atoms[2].

Throughout the series, the Néel temperatures, T_N, scale well with the de Gennes factor, $(g-1)^2 J(J+1)$ (see Fig. 1.2), where g is the Landé factor and J is the total angular momentum of the Hund's rule ground state of the rare earth ion, R^{3+}. This is consistent with long range order of localized magnetic moments coupled via a RKKY-type interaction. Calculations of the generalized electronic susceptibility, $\chi(\mathbf{q})$ (without matrix elements), based on the normal-state electric band structure of $\mathrm{LuNi_2B_2C}$, show

---

[2] The position of the B atoms is not completely determined by the symmetry of the structure. Their z-coordinate is a free parameter and may vary from compound to compound. All other atoms are occupying sites of higher local symmetry with no free parameters.

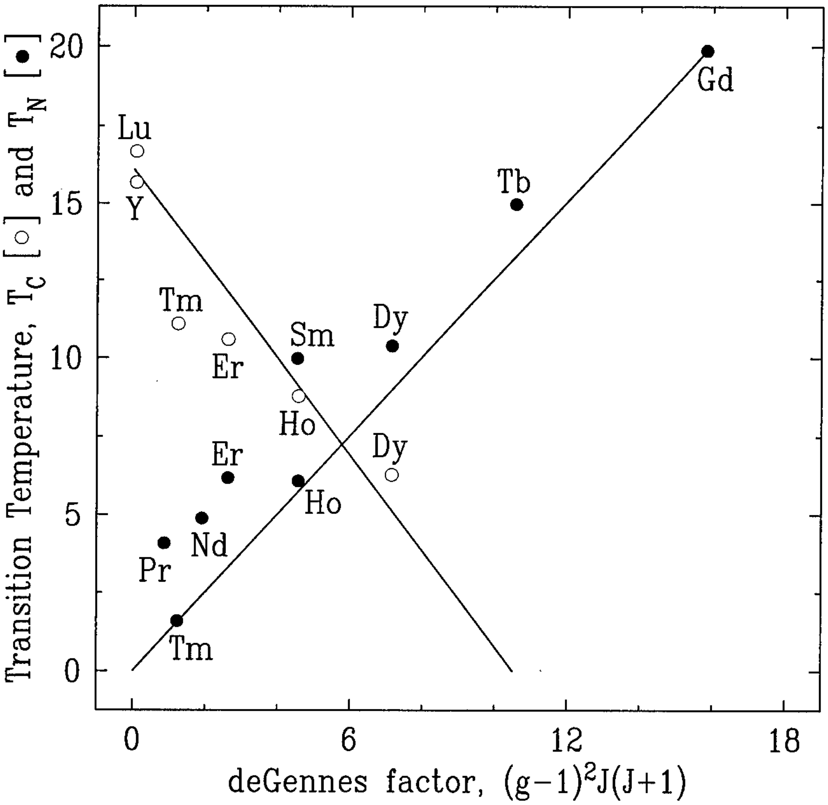

Figure 1.2 The magnetic and superconducting transition temperatures for the $R\mathrm{Ni}_2\mathrm{B}_2\mathrm{C}$ series as a function of the de Gennes factor. The solid lines are intended as a guide to the eye.

a pronounced peak near **q** = (0.6, 0, 0) which is due to Fermi surface nesting [Rhe95]. Indeed, inelastic neutron scattering experiments observed softening of the two lowest Δ_4-phonon branches close to this wave vector [Der95a, Sta97]. The fact that these effects were observed in the Lu-based compound indicates that the aforementioned nesting feature is not correlated to the $4f$ electrons and that therefore it can be expected in all members of the $R\mathrm{Ni_2B_2C}$ family. It should also be pointed out that this wave vector is remarkably close the the boundary of the first Brillouin zone at $\mathbf{q} = (\frac{1}{2}(1 + \frac{a^2}{c^2}),\ 0,\ 0)$. The room temperature position of the zone boundary is also listed in Table 1.1.

The strong anisotropic magnetic behavior found in some members of the family indicate that crystalline electric field energies (CEF) play an important role in the formation of the magnetically ordered state [Can94, Cho95b, Rat96, Cho95d].

The superconducting and magnetic properties of most members of the family[3] have been studied by a large variety of techniques, including macroscopic anisotropic magnetization, resistivity, thermal conductivity, nuclear magnetic resonance (NMR), muon spin rotation (μSR), magnetic neutron scattering and magnetic x-ray scattering measurements, the latter within the framework of this thesis. A detailed discussion of the results of all these experiments is beyond the scope of this work (for an overview see refs. [Cho95d, Can00a, Sta00, Lyn00a]). However, we would like to summarize the main features of the antiferromagnetic structures that were observed in these experiments:

- $\mathrm{LuNi_2B_2C}$: This compound has the highest superconducting transition temperature within the series[4], $\mathrm{T}_C = 16.6$ K [Nag94, Cav94a, Cav94b, Eis94]. No magnetic ordering above 2 K was observed.

---

[3] Exceptions are $\mathrm{PmNi_2B_2C}$ and $\mathrm{EuNi_2B_2C}$. Pm is radioactive which makes both the growth and the characterization of the samples troublesome. Efforts to obtain single crystals of the Eu compound are complicated by the oxygen sensitivity, the high vapor pressure and the possible divalency of Eu [Can97b, Cav97, Gup97]. To the best of our knowledge, neither powder or single crystal samples of this material are available to date.

[4] Recently, a superconducting transition temperature as high as $\mathrm{T}_C = 23$ K was observed [Fuj94, Zan94] in $\mathrm{YPd_2B_2C}$.

- $YbNi_2B_2C$: Above 0.34 K, neither superconductivity nor long range magnetic order have been found in this compound. However, it displays moderate heavy fermion behavior with a Sommerfeld coefficient of γ = 530 mJ/mol K^2 indicative of a Kondo temperature, T_K, around 10 K [Yat96, Dha96]. De Gennes scaling predicts a magnetic ordering temperature of $T_N \approx 0.4$ K and superconducting transition temperature of $T_C \approx 10$ K. Neither magnetic order nor superconductivity has been observed above 0.34 K.

- $TmNi_2B_2C$: The critical temperature for superconductivity in this compound was found to be $T_C = 11$ K [Cav94a, Eis94, Cho95a]. Long range antiferromagnetic order develops below the Néel temperature, $T_N = 1.5$ K [Mov94, Cho95a, Lyn97], coexisting with superconductivity. An incommensurate magnetic structure with modulation wave vector $\mathbf{q} = (0.093, 0.093, 0)$ was determined by neutron diffraction [Cha96, Lyn97, Ste97]. These experiments indicate that the magnetic moment direction, $\hat{z}_n$, is parallel to the (0, 0, 1)-axis of the sample. There are also indications for weak ferromagnetism below T_N.

- $ErNi_2B_2C$: Superconductivity is observed below $T_C = 10.5$ K [Cav94a, Eis94, Cho95b]. The onset of antiferromagnetic order below $T_N = 6.0$ K lowers the upper critical field, H_{C2}, especially if the field is applied perpendicular to the (0, 0, 1)-axis [Cho95b]. Again, the antiferromagnetic structure was investigated by neutron scattering [Sin95, Zar95]. The modulation wave vector was determined to be $\mathbf{q} = (0.55, 0, 0)$, and appears to be independent of temperature [Sin95]. The magnetic moments are aligned parallel to the (0, 1, 0)-axis of the crystal, perpendicular to the modulation wave vector[5]. There are indications for magnetostriction below T_N and weak ferromagnetism at very low temperatures [Can96, Yar96], $T < 2.3$ K.

---

[5] Note that the tetragonal symmetry of the system implies the existence of domains with modulation wave vectors $\mathbf{q} = (\pm 0.55, 0, 0)$ and $\mathbf{q} = (0, \pm 0.55, 0)$.

- $HoNi_2B_2C$: In the absence of external magnetic fields, two distinct magnetic phases, with transitions temperatures $T_N = 6$ K and $T_{IC-C} = 5.1$ K, are observed in coexistence with superconductivity ($T_C = 8.7$ K) [Cav94a, Eis94, Can94, Rat96]. Neutron [Gol94, Gri94, Vog95b, Vog95b] and, as part of this thesis (see chapter 5), XRES experiments [Hil96a] revealed an incommensurate structure characterized by two modulation wave vectors, $\mathbf{q}_a = (0.585, 0, 0)$ and $\mathbf{q}_c = (0, 0, 0.915)$, between 6.1 K and 5.1 K. This magnetic structure strongly suppresses superconductivity ($H_{C2} \leq 200$ G!). Below 5.1 K, the magnetic moments order in a simple antiferromagnetic structure with modulation wave vector $\mathbf{q} = (0, 0, 1)$. This transition from the incommensurate into the commensurate magnetic phase is accompanied by an recovery of the superconducting properties ($H_{C2} > 1000$ G).

  Anisotropic magnetization measurements strongly indicate that in all phases the magnetic moments are aligned along one of the four crystallographic (1, 1, 0) directions [Can97a].

- $DyNi_2B_2C$: In this material, the onset of superconductivity ($T_C = 6.2$ K) [Cho95c, Lin95, Tom95] is observed *below* the antiferromagnetic ordering temperature ($T_N = 10.3$ K) [Eis94]. Neutron scattering experiments [Der95b, Lyn96, Lyn97] observed the same magnetic structure as in $HoNi_2B_2C$ at the lowest temperatures: The magnetic moments are aligned within the basal plane, and the modulation wave vector is $\mathbf{q} = (0, 0, 1)$. Again, anisotropic magnetization measurements indicate an alignment of the magnetic moment parallel to the $(1, 1, 0)$ direction [Can00b].

- $TbNi_2B_2C$: Anisotropic magnetization measurements [Tom96, Cho96a] down to 2 K revealed no superconductivity in this compound. It does, however, order antiferromagnetically below $T_N = 14.9$ K. In neutron scattering experiments [Der96] the magnetic modulation wave vector was found to increase from $\mathbf{q} = (0.51, 0, 0)$ at

T = 14.9 K to (0.545, 0, 0) at T = 2.3 K, the lowest temperature reached in these experiments. Contrary to other members of this series, the magnetic moments are aligned parallel to the modulation wave vector, forming a longitudinal spin wave.

- $GdNi_2B_2C$: While powder magnetization measurements [ElM94, Bud95] observed only the onset of antiferromagnetic order at T_N = 19.8 K[6], a second phase transition at 13.6 K was revealed in magnetization experiments on single crystals [Can95], suggesting that a continuous spin reorientation takes place at this temperature. No superconductivity has been observed down to 2 K.

  As natural Gd strongly absorbs neutrons, XRES was used to study the microscopic magnetic structure of this compound [Det96]. These measurements were also carried out within the framework of this thesis. Experimental procedure and results are therefore described in detail in chapter 5. In summary, below the antiferromagnetic ordering temperature, T_N = 19.8 K, $GdNi_2B_2C$ forms an incommensurate structure with modulation wave vector $\mathbf{q} \approx (0.55, 0, 0)$ and magnetic moments aligned parallel to the crystallographic (0, 1, 0) axis, similar to the Er compound. With decreasing temperature, the modulation wave vector varies from (0.551, 0, 0) at T = 19.8 K to (0.549, 0, 0) at T = 13.6 K, where the trend is reversed and the modulation wave vectors increases continuously with decreasing temperature up to (0.553, 0, 0) at 3.7 K, the lowest temperature reached in the experiments. Below 13.6 K, an additional component of the ordered magnetic moment along the crystallographic (0, 0, 1) direction was observed.

- $EuNi_2B_2C$: To the best of our knowledge, this compound has not been studied yet [Can97b, Cav97, Gup97]. This is very unfortunate, since we expect interesting properties, due to the small magnetic moment of the Eu^{3+} ion.

---

[6] These experiments also observed a phase transition around 45 K. However, this is the onset of magnetic order in GdB_2C_2, which was apparently contaminating the samples.

- $SmNi_2B_2C$: μSR [Pra95] and magnetization measurements [Can00c] observed the onset of antiferromagnetic order below $T_N = 9.9$ K. As in the Gd compound, the large absorption cross section of natural Sm makes neutron experiments difficult. Instead, XRES measurements were applied [Det97], as detailed in chapter 5. The magnetic structure was found to be commensurate, with modulation wave vector $\mathbf{q} = (\frac{1}{2}, 0, \frac{1}{2})$ and magnetic moment direction parallel to (0, 0, 1).

- $PmNi_2B_2C$: Since natural Pm is radioactive, no samples of this compound are available. Although ^{145}Pm has a relatively long half-life time of $T_{1/2} = 17.7$y, it is extremely expensive to obtain and uncomfortable to handle. All other Pm isotopes have shorter half-life times.

- $NdNi_2B_2C$: Magnetization measurements determined the the Néel temperature as $T_N = 4.8$ K. Both neutron [Gol97, Lyn97] and XRES techniques [Det97] were used to study the magnetic structure of this compound. Details of the XRES experiments can be found in chapter 5. While the modulation wave vector is the same as in $SmNi_2B_2C$, $\mathbf{q} = (\frac{1}{2}, 0, \frac{1}{2})$, the magnetic moments are aligned in a different direction, parallel to the (1, 1, 0)-axis of the crystal.

- $PrNi_2B_2C$: Below T_N=4.0, the same magnetic structure as in $HoNi_2B_2C$ (at the lowest temperatures) and $DyNi_2B_2C$ develops [Lyn97]. The modulation wave vector is $\mathbf{q} = (0, 0, 1)$, and the magnetic moments are aligned within the basal plane.

- $CeNi_2B_2C$: Neither superconductivity, nor long range magnetic order have been observed.

- $LaNi_2B_2C$: Neither superconductivity, nor long range magnetic order have been observed.

- YNi_2B_2C: This compound does not exhibit any long range magnetic order. However, it is superconducting with a relatively high transition temperature, T_C = 15.6 K.

In summary, three families of magnetic structures are observed in the $R$$Ni_2B_2C$ compounds: 1) Simple antiferromagnets with $\mathbf{q} = (0,\ 0,\ 1)$, as in $DyNi_2B_2C$, the low temperature phase of $HoNi_2B_2C$ and $PrNi_2B_2C$. 2) Commensurate antiferromagnets with $\mathbf{q} = (\frac{1}{2},\ 0,\ \frac{1}{2})$, as in $NdNi_2B_2C$ and $SmNi_2B_2C$. 3) Incommensurate antiferromagnets with $\mathbf{q} \approx (0.55,\ 0,\ 0)$, as in $GdNi_2B_2C$, $TbNi_2B_2C$, $ErNi_2B_2C$, and with some modifications, in the intermediate temperature range of $HoNi_2B_2C$. In addition to these three groups, there are the non-magnetic compounds, and a few "black sheep" ($YbNi_2B_2C$ and $TmNi_2B_2C$) that refuse to fit into any of the above categories.

From this overview, we see that in the compounds with larger rare-earth deGennes factor, superconductivity is destroyed by magnetic scattering. The onset of long range magnetic order in $DyNi_2B_2C$ with $\mathbf{q} = (0,\ 0,\ 1)$ significantly reduces this cross section [Cho96c], while the even larger deGennes factors suppress superconductivity completely in the Tb and Gd members of the family. Apparently, the commensurate magnetic structure with $\mathbf{q} = (0,\ 0,\ 1)$ observed in the Dy and Ho compounds does not interfere with superconductivity, while the incommensurate magnetic structures with $\mathbf{q} \approx (0.55,\ 0,\ 0)$ seem to weaken the superconducting order parameter in $ErNi_2B_2C$ and $HoNi_2B_2C$, as evidenced by a decrease of H_{c2} at the magnetic ordering temperature in these compounds. This suggests that the origins of superconductivity in these compounds are indeed strongly related to the nesting feature found in band structure calculations and seen as phonon softening in $LuNi_2B_2C$.

No superconductivity is observed in the light rare earth compounds. While the deGennes factors for these materials are small, and the Néel temperatures are comparable to the heavy rare earth members, they differ from them in their ratio of the lattice parameters, a/c, which is much larger for the light rare earths (La: 0.385, Gd: 0.345, Lu: 0.326). Along with the variation of the Boron z position (La: 0.349, Gd: 0.357, Lu: 0.362 [Sie94b]), this leads to a strong deviation of the B–Ni–B bonding angle from the ideal tetrahedral angle, 109.47°, in the lighter rare earth compounds (Lu: 108.7°, Gd: 106.1°, La: 102.1°). These structural changes are believed to influence the density of states, especially the large contribution from the Ni 3d electrons close to the Fermi energy and thus suppress superconductivity in the light rare earth compounds [Sie94b].

2 MAGNETIC INTERACTIONS IN THE RARE-EARTH NICKEL BOROCARBIDES

The magnetic structures of the rare-earth nickel borocarbides are determined by several competing interactions: The intra-atomic coulomb and spin-orbit interactions, the inter-atomic coulomb (crystalline electric fields, CEF) and magnetic interactions (direct and indirect exchange interactions, magnetic dipole-dipole interaction) with neighboring atoms, and the Zeeman interaction with externally applied magnetic fields:

$$H = H_{\text{Coulomb}} + H_{\text{Spin-Orbit}} + H_{\text{Magnetic}} + H_{\text{CEF}} + H_{\text{Zeeman}}. \qquad (2.1)$$

In the case of rare earths, the intra-atomic coulomb and the spin-orbit interactions are the dominant terms in the Hamiltonian. Therefore the other terms can be treated as a perturbation to the Hund's rule ground state[1] of the rare-earth ion, usually[2] R^{3+}. Furthermore, only the Zeeman interaction of the rare earth $4f$ electrons has to be taken into account. In the following sections, we will briefly discuss the magnetic and CEF interactions, their competition, and the effects on the magnetic structure upon the rare-earth nickel borocarbides.

---

[1] In the case of Eu and Sm, low lying states of the j-multiplet can cause complications.

[2] Ce, Sm, Eu, and Yb may also occur in other ionization states: Ce^{4+}, Sm^{2+}, Eu^{2+}, Yb^{2+}.

Magnetic interactions

Most important for the formation of a magnetically ordered state is, of course, the nature of the magnetic interaction between unpaired electrons. Possible mechanisms that may induce long range magnetic order are direct exchange, indirect exchange and the magnetic dipole–dipole interaction.

Direct exchange interaction occurs if the orbits of unpaired "magnetic" electrons overlap between neighboring atoms. It requires that the magnetic electrons are — at least partially — delocalized. This situation occurs frequently in $3d$ transition metals. In order to minimize their electrostatic coulomb energy, the electrons arrange themselves in a certain symmetry that dictates the orientation of the magnetic moments and may lead to an ordered magnetic structure, similar to the magnetic alignment in partially filled shells given by Hund's rules.

Ruderman-Kittel-Kasuya-Yosida-Interaction

The $4f$ electrons in rare-earth compounds, on the other hand, are strongly localized. Therefore there is essentially no overlap between the $4f$ electrons of two neighboring atoms. In this case the exchange interaction may be transmitted indirectly through spin polarization of the conduction band. The resulting net exchange between two separated, localized magnetic atoms is called RKKY (Ruderman-Kittel-Kasuya-Yosida) interaction [Rud54, Kas56, Yos57, Ded93].

RKKY energy of modulated magnetic systems

To first order, the RKKY interaction energy between two localized magnetic moments, $\boldsymbol{\mu}_j$ and $\boldsymbol{\mu}_k$ at the positions $\mathbf{r}_j$ and $\mathbf{r}_k$, respectively, is given by [Ded93]:

$$\Delta E_{j,k} = -\frac{1}{4}\boldsymbol{\mu}_j \cdot \boldsymbol{\mu}_k \int \mathrm{d}^3\mathbf{r} \int \mathrm{d}^3\mathbf{r}'\, I_j(\mathbf{r})\chi_0(\mathbf{r},\mathbf{r}')I_k(\mathbf{r}'). \tag{2.2}$$

In this approximation the interaction energy depends only on the magnitude of the moments and their *relative* orientation. No conclusions about the orientation with respect to crystallographic directions may be drawn[3].

$$\chi_0(\mathbf{r},\mathbf{r}') = -\frac{2}{\pi}\int_{-\infty}^{\infty} \mathrm{d}E\, f(E)\Im\left[G_0(\mathbf{r},\mathbf{r}',E)G_0(\mathbf{r}',\mathbf{r},E)\right] \tag{2.3}$$

is the linear susceptibility of the electronic system. According to this definition [Ded93], it is symmetric and real. Typically, it depends only on the *relative* position, $\mathbf{r}_j - \mathbf{r}_k$, of the interacting points. $f(E)$ is the Fermi function, and $G_0(\mathbf{r},\mathbf{r}',E)$ is the Greens function of the unperturbed system (without magnetic interaction), such that $(E-H_0)G_0(\mathbf{r},\mathbf{r}',E) = \delta(\mathbf{r}-\mathbf{r}')$, where $H_0 = H_{\mathrm{Coulomb}} + H_{\mathrm{Spin-Orbit}}$ is the Hamiltonian of the unperturbed system. $I_j(\mathbf{r})$ is the exchange interaction between the localized moments and the conduction electrons. We assume these interactions to be contact interactions, i.e. $I_j(\mathbf{r}) = I\delta(\mathbf{r}_j - \mathbf{r})$. The interaction energy, equation (2.2), then reduces to

$$\Delta E_{j,k} = -\frac{I^2}{4}\boldsymbol{\mu}_j \cdot \boldsymbol{\mu}_k\, \chi_0(\mathbf{r}_j - \mathbf{r}_k). \tag{2.4}$$

We now try to estimate the average RKKY interaction energy per atom for a periodically modulated magnetic structure with wave vector $\mathbf{q}$. Let the local magnetic moment at the position $\mathbf{r}_j$ be given by $\boldsymbol{\mu}_j = \Re\left[\boldsymbol{\mu}\, e^{i\mathbf{r}_j\cdot\mathbf{q}}\right]$. We first calculate the total interaction energy for an atom at position $\mathbf{r}_j$.

$$\begin{aligned}
\Delta E_j &= \sum_{k\neq j} \Delta E_{j,k}; && (2.5)\\
\Delta E_j + \Delta E_{j,j} &= -\frac{I^2}{4}\sum_k \boldsymbol{\mu}_j \cdot \Re\left[\boldsymbol{\mu} e^{i\mathbf{r}_k\cdot\mathbf{q}}\right] \chi_0(\mathbf{r}_j - \mathbf{r}_k) && (2.6)\\
&= -\frac{I^2}{4}\boldsymbol{\mu}_j \cdot \sum_k \Re\left[\boldsymbol{\mu} e^{i\mathbf{r}_k\cdot\mathbf{q}}\right] \int \mathrm{d}^3\mathbf{q}'\, \tilde{\chi}_0(\mathbf{q}')\, e^{i\mathbf{q}'\cdot(\mathbf{r}_j-\mathbf{r}_k)} && (2.7)
\end{aligned}$$

---

[3] However, higher orders of the RKKY interaction energy may well include terms that do show explicit dependence upon the moment's orientation relative to crystallographic directions.

$$\begin{aligned}
&= -\frac{I^2}{8}\boldsymbol{\mu}_j \cdot \int \mathrm{d}^3\mathbf{q}'\tilde{\chi}_0(\mathbf{q}')e^{i\mathbf{q}'\mathbf{r}_j} \sum_k \left[\boldsymbol{\mu}\, e^{i\mathbf{r}_k\cdot(\mathbf{q}-\mathbf{q}')} + \boldsymbol{\mu}^\dagger\, e^{i\mathbf{r}_k\cdot(\mathbf{q}+\mathbf{q}')}\right] && (2.8)\\
&= -\frac{I^2}{8} \int \mathrm{d}^3\mathbf{q}'\tilde{\chi}_0(\mathbf{q}')e^{i\mathbf{q}'\mathbf{r}_j}\, \boldsymbol{\mu}_j \cdot \left[\boldsymbol{\mu}\, \delta(\mathbf{q}'-\mathbf{q}) + \boldsymbol{\mu}^\dagger\, \delta(\mathbf{q}'+\mathbf{q})\right] && (2.9)\\
&= -\frac{I^2}{8}\boldsymbol{\mu}_j \cdot \left[\boldsymbol{\mu}\, \tilde{\chi}_0(\mathbf{q})\, e^{i\mathbf{q}\mathbf{r}_j} + \boldsymbol{\mu}^\dagger\, \tilde{\chi}_0(-\mathbf{q})\, e^{-i\mathbf{q}\mathbf{r}_j}\right]; && (2.10)\\
\Delta E_j &= fracI^2 4 \left[\tilde{\chi}_0(\mathbf{q}) - \chi_0(\mathbf{0})\right] \boldsymbol{\mu}_j \cdot \boldsymbol{\mu}_j. && (2.11)
\end{aligned}$$

Here we replaced the susceptibility by its Fourier transform, $\tilde{\chi}_0(\mathbf{q})$, and used $\tilde{\chi}_0(\mathbf{q}) = \tilde{\chi}_0(-\mathbf{q})$, since χ_0 is real and symmetric. The average RKKY energy per atom is then (assuming $\mathbf{q} \neq \mathbf{0}$):

$$\langle \Delta E_j \rangle = \frac{1}{2N}\sum_j \Delta E_j = -\frac{I^2}{16}\left[\tilde{\chi}_0(\mathbf{q}) - \chi_0(\mathbf{0})\right] |\boldsymbol{\mu}|^2 . \tag{2.12}$$

We see that only the Fourier component of the magnetic modulation wave vector, $\mathbf{q}$, appears in the total RKKY energy. Reversing our argument, we can therefore conclude that, for a given susceptibility, the system will order with a modulation wave vector where, or at least close to where, the Fourier component of this susceptibility reaches its maximum.

In a band structure picture of the indirect exchange between the localized $4f$ electrons and the conduction band, such a peak in the Fourier spectrum of the susceptibility may be related to a nesting of the Fermi surface. This causes a singularity in the susceptibility with a wave vector equal to the "distance" in reciprocal space between the parallel segments of Fermi surface. The resulting instability may be resolved by a spontaneous modulation of the crystal, either in the form of a charge density wave, spin wave, a helical magnetic modulation or similar effects. Such a nesting feature, however, is not the only requirement for long range magnetic order.

Indeed, band structure calculations for $\mathrm{LuNi_2B_2C}$ show a maximum in the susceptibility at a wave vector of $\mathbf{q} = (0.6, 0, 0)$ [Rhe95], while inelastic neutron scattering measurements of the phonon spectrum in the same compound revealed a low temperature softening of the two lowest Δ_4 branches at approximately the same wave vector [Der95a]. The fact that these features were observed in the non-magnetic Lu-based compound indicates that this nesting feature is not correlated to the $4f$ electrons and that therefore it can be expected in all members of the $R\mathrm{Ni}_2\mathrm{B}_2\mathrm{C}$ family.

To first order, the RKKY interaction dictates only the modulation wave vector, but not the orientation of the moments. In rare earth systems, these are usually determined by the crystalline electric fields (CEF), a local phenomenon that reflects the symmetry of the electrostatic fields in the crystal [Bet29, Wig31]. In cases where a specific high-symmetry direction is strongly preferred due to its low CEF energy, the competition between CEF and RKKY energies may lead to distortions of helical spin modulations (lock-in transitions), as, for example, in Ho metal [Gib88, Gib91].

Magnetic dipole–dipole interaction

The magnetic dipole–dipole interaction is typically the weakest of the magnetic interactions and is therefore usually neglected. However, it has the longest range among the aforementioned interactions and can cause macroscopic effects, such as the formation of domains in ferromagnets. It is also important in cases where the stronger interactions leave degeneracies, e.g. in the case of an **a**-modulated tetragonal structure, where the CEF energies for longitudinal and transverse spin waves are identical.

Anisotropy induced by crystalline electric fields

The pronounced anisotropy in the macroscopic magnetic behavior of the rare-earth borocarbides indicates that crystalline electric fields (CEF) play an important role in the formation of the magnetically ordered state. In this section, we will briefly review the physical principles of CEF-splittings in tetragonal systems and then describe the specific case of the $R\mathrm{Ni}_2\mathrm{B}_2\mathrm{C}$ family.

Table 2.1 Character table for the point group $D_4 = 422$, after Altmann and Herzig [Alt94]. The first 5 irreducible representations, the singlets $A_{1,2}$ and $B_{1,2}$, and the doublet E describe states with integer angular momentum (boson states), j, while the "extra" representations, the doublets $E_{1/2,3/2}$, describe states with half-integer angular momentum (fermion states).

	Γ_i	E	$2C_4$	$C_2 = C_4^2$	$2C_2'$	$2C_3''$
Γ_1	A_1	1	1	1	1	1
Γ_2	A_2	1	1	1	-1	-1
Γ_3	B_1	1	-1	1	1	-1
Γ_4	B_2	1	-1	1	-1	1
Γ_5	E	2	0	-2	0	0
Γ_6	$E_{1/2}$	2	$\frac{1}{\sqrt{2}}$	0	0	0
Γ_7	$E_{3/2}$	2	$-\frac{1}{\sqrt{2}}$	0	0	0

CEF levels in tetragonal systems

For a free ion, all Zeeman levels of an unfilled shell are degenerate. If the ion is placed into a crystalline environment, this is generally not the case: The presence of electrostatic fields, due to neighboring ions, induces a splitting (CEF splitting). These splittings can be interpreted geometrically, since the orbitals of partially filled shells are not spherical, and their shape depends on their angular momentum quantum numbers, l, s, j and m_j. Obviously, the symmetries and degeneracies of the CEF-split eigenfunctions depends on the symmetry of the crystalline electric fields, i.e. the point symmetry of the lattice site the ion occupies. The most convenient mathematical treatment of these effects is through the application of group theoretical methods [Bet29, Wig31, Tin64]. A direct result of a group theoretical analysis is that all eigenfunctions of the Hamiltonian belong to representations of the symmetry group, where the degeneracy of the state is given by the dimension of this representation [Bet29]. The irreducible representations for tetragonal symmetry and their characters are listed in Table 2.1.

The CEF energy of a magnetic ion located at a lattice site with tetragonal point symmetry can be written as [Whi83]:

$$H_{\text{CEF}} = B_2^0 O_2^0 + B_4^0 O_4^0 + B_4^4 O_4^4 + B_6^0 O_6^0 + B_6^4 O_6^4, \tag{2.13}$$

where the B_n^m are the CEF parameters determining the scale of the splittings. They have been studied extensively for cubic symmetry ($B_2^0 = 0$, $B_4^4 = 5B_4^0$, and $B_6^4 = 21B_6^0$), [Hut64, Lea62]. A rigorous discussion for tetragonal symmetry is difficult because of the large number of independent parameters. The Stevens' operator equivalents, O_n^m, are given by [Ste52, Ble53]:

$$\begin{aligned}
O_2^0 &= 3J_z^2 - j(j+1) && (2.14)\\
O_4^0 &= 35J_z^4 - [30j(j+1) - 25]J_z^2 - 6j(j+1) + 3j^2(j+1)^2 && (2.15)\\
O_4^4 &= \frac{1}{2}(J_+^4 + J_-^4) && (2.16)\\
O_6^0 &= 231J_z^6 - 105[3j(j+1) - 7]J_z^4 && \\
&\quad +[105j^2(j+1)^2 - 525j(j+1) + 294]J_z^3 && \\
&\quad -5j^3(j+1)^3 + 40j^2(j+1)^2 - 60j(j+1) && (2.17)\\
O_6^4 &= \frac{1}{4}[11J_z^2 - j(j+1) - 38](J_+^4 + J_-^4) && \\
&\quad +\frac{1}{4}(J_+^4 + J_-^4)[11J_z^2 - j(j+1) - 38]. && (2.18)
\end{aligned}$$

Due to its electrostatic nature, eq. (2.13) is invariant under time reversal, therefore the angular momentum expectation value, $\langle\psi\,|\mathbf{J}|\,\psi\rangle$, of all non-degenerate (singlet) eigenstates $|\psi\rangle$, has to vanish. This leads to the aforementioned competition between CEF and magnetic interactions, as demonstrated below. It also means that all CEF levels of an ion with half-integer total angular momentum are two- or fourfold degenerate (Kramers theorem, [Kra30]).

Table 2.2 Decomposition of the free ion ($O(3)$) ground state of the rare earth ions, R^{3+}. Notice that for the ions with half integer total angular momentum, j, all levels are twofold degenerate (Kramers theorem, [Kra30]).

R^{3+}	$^{2s+1}L_j$	D_4 irreducible representations	Parity
La^{3+}	$^1S_0$	A_1	g
Ce^{3+}	$^2F_{5/2}$	$E_{1/2} \oplus 2E_{3/2}$	u
Pr^{3+}	$^3H_4$	$2A_1 \oplus A_2 \oplus B_1 \oplus B_2 \oplus 2E$	u
Nd^{3+}	$^4I_{9/2}$	$3E_{1/2} \oplus 2E_{3/2}$	g
Pm^{3+}	$^5I_5$	$A_1 \oplus 2A_2 \oplus B_1 \oplus B_2 \oplus 3E$	g
Sm^{3+}	$^6H_{5/2}$	$E_{1/2} \oplus 2E_{3/2}$	u
Eu^{3+}	$^7H_0$	A_1	u
Gd^{3+}	$^8S_{7/2}$	$2E_{1/2} \oplus 2E_{3/2}$	g
Tb^{3+}	$^7F_6$	$A_1 \oplus 2A_2 \oplus 2B_1 \oplus 2B_2 \oplus 3E$	u
Dy^{3+}	$^6H_{15/2}$	$4E_{1/2} \oplus 4E_{3/2}$	u
Ho^{3+}	$^5I_8$	$3A_1 \oplus 2A_2 \oplus 2B_1 \oplus 2B_2 \oplus 4E$	g
Er^{3+}	$^4I_{15/2}$	$4E_{1/2} \oplus 4E_{3/2}$	g
Tm^{3+}	$^3H_6$	$A_1 \oplus 2A_2 \oplus 2B_1 \oplus 2B_2 \oplus 3E$	u
Yb^{3+}	$^2F_{7/2}$	$2E_{1/2} \oplus 2E_{3/2}$	u
Lu^{3+}	$^1S_0$	A_1	g

Table 2.3 CEF parameters, A_{nm}, for some rare-earth nickel borocarbides after Gasser *et al.* [Gas96].

Compound	A_{20} [meV]	A_{40} [meV]	A_{44} [meV]	A_{60} [meV]	A_{64} [meV]
$HoNi_2B_2C$	-14.5±6.0	2.3 ±0.8	-71.4±3.1	-0.42±0.1	11.7±1.4
$ErNi_2B_2C$	- 6.3±1.3	3.3 ±0.3	-73.9±1.3	-0.61±0.12	10.1±3.1
$TmNi_2B_2C$	-13.0±0.3	2.16±0.14	-63.1±1.2	-1.32±0.05	15.6±1.1

For the case of rare earth elements, the "magnetic" $4f$ electrons are shielded by the $5s^2 5p^6$ shells so that the CEF energies are smaller than the spin orbit interaction. Therefore the CEF Hamiltonian, eq. (2.13), can be treated as a perturbation. Usually it is sufficient to consider the splitting of the free ion's ground state. The number and degeneracies of the split levels can again be determined by group theory (see Table 2.2). To determine the energy eigenvalues, the symmetry of the ground state, and the magnitude of the splittings however one needs to know the CEF parameters, B^n_m.

CEF measurements of borocarbides

For several of the borocarbides, the CEF parameter B_2^0 was estimated from the difference in the Weiss-temperatures, $\theta_{x,y}$ and θ_z [Cho95b, Cho96a, Cho96b], using the leading term in an expansion in $1/T$ of the Curie-Weiss susceptibility, χ [Bou73]. A complete set of CEF parameters for Ho^{3+} in $\mathrm{Lu_{0.976}Ho_{0.024}Ni_2B_2C}$ was obtained from a fit to the static susceptibility in external fields of 0.1 T applied parallel and perpendicular to the **c**-axis at low temperatures[Cho96b].

For the Ho, Er and Tm members of the $R\mathrm{Ni_2B_2C}$ family, the CEF parameters have been determined by inelastic neutron scattering of powder samples [Gas96]. The values obtained by Gasser *et al.* are listed in Table 2.3. The CEF parameters, A_{mn}, used by these authors are related to the one used in the current work by $B^m_n = \langle r^n \rangle \alpha_n A_{nm}$, where $\langle r^n \rangle$ is the quantum mechanical expectation value of r^n for the "magnetic" (4f) electrons. The values of the proportionality factors, α_n, have been tabulated by Judd [Jud57] and Elliott *et al.* [Ell57].

Competition between CEF and magnetism

We will now study the structure of the CEF levels in the presence of an external magnetic field, **B**. In the high-temperature paramagnetic phase, **B** is a macroscopic, externally applied field, while in the antiferromagnetically ordered phase, **B** is an "exchange field" used to approximate the RKKY- and other magnetic interactions.

In the presence of an magnetic field, **B**, the eigenvalues, E_i, and corresponding eigenfunctions, ψ_i, are determined by diagonalizing the sum of the CEF and Zeeman Hamiltonian[4]:

$$E_i \psi_i = (H_{\mathrm{CEF}} - \mathbf{B} \cdot \mu_B g_j \mathbf{J}) \psi_i, \tag{2.19}$$

where **J** is the total angular momentum operator, $g_j = 1 + \frac{j(j+1)+s(s+1)-l(l+1)}{2j(j+1)}$ is the Landé factor, and the eigenfunctions of the combined Hamiltonian are a linear combination of the degenerate spin-orbit eigenfunctions, $\psi_i = \sum_{m_j=-j}^{j} b_{i,m_j} \left| j, m_j \right\rangle$. Due to the anisotropy in the CEF Hamiltonian, H_{CEF} (eq. (2.13)), the quantization direction and the direction of the applied external field may not be chosen in an arbitrary fashion, therefore the Zeeman energy has to be included in *vector* form. Because of the aforementioned competition between CEF and magnetic interactions, the energy eigenvalues, E_i, and the coefficients, b_{i,m_j}, will vary as a function of strength and direction of the magnetic field, **B**.

The system's magnetization is given by thermodynamic average of the angular momentum operator, **J**:

$$\mathbf{M}(T, \mathbf{B}) = \langle \mu_B \mathbf{J} \rangle = \frac{\sum_i \langle i \left| \mu_B g_j \mathbf{J} \right| i \rangle \, e^{-\beta E_i}}{\sum_i e^{-\beta E_i}}, \tag{2.20}$$

where $\beta = \frac{1}{k_B T}$ is the inverse temperature in units of meV.

To demonstrate the magnetic anisotropy caused by the CEF splitting, we now consider the simplest non-trivial example, an ion with $j = l = 1$ and $s = 0$ in a crystal where CEF parameters vanish, except B_2^0 (Unfortunately, no rare earth ion has these

---

[4] As mentioned above, both CEF and Zeeman Hamiltonian are treated as a small perturbation to the (degenerate) ground state, $\left| j, l, s, m_j \right\rangle$, of the free ion Hamiltonian.

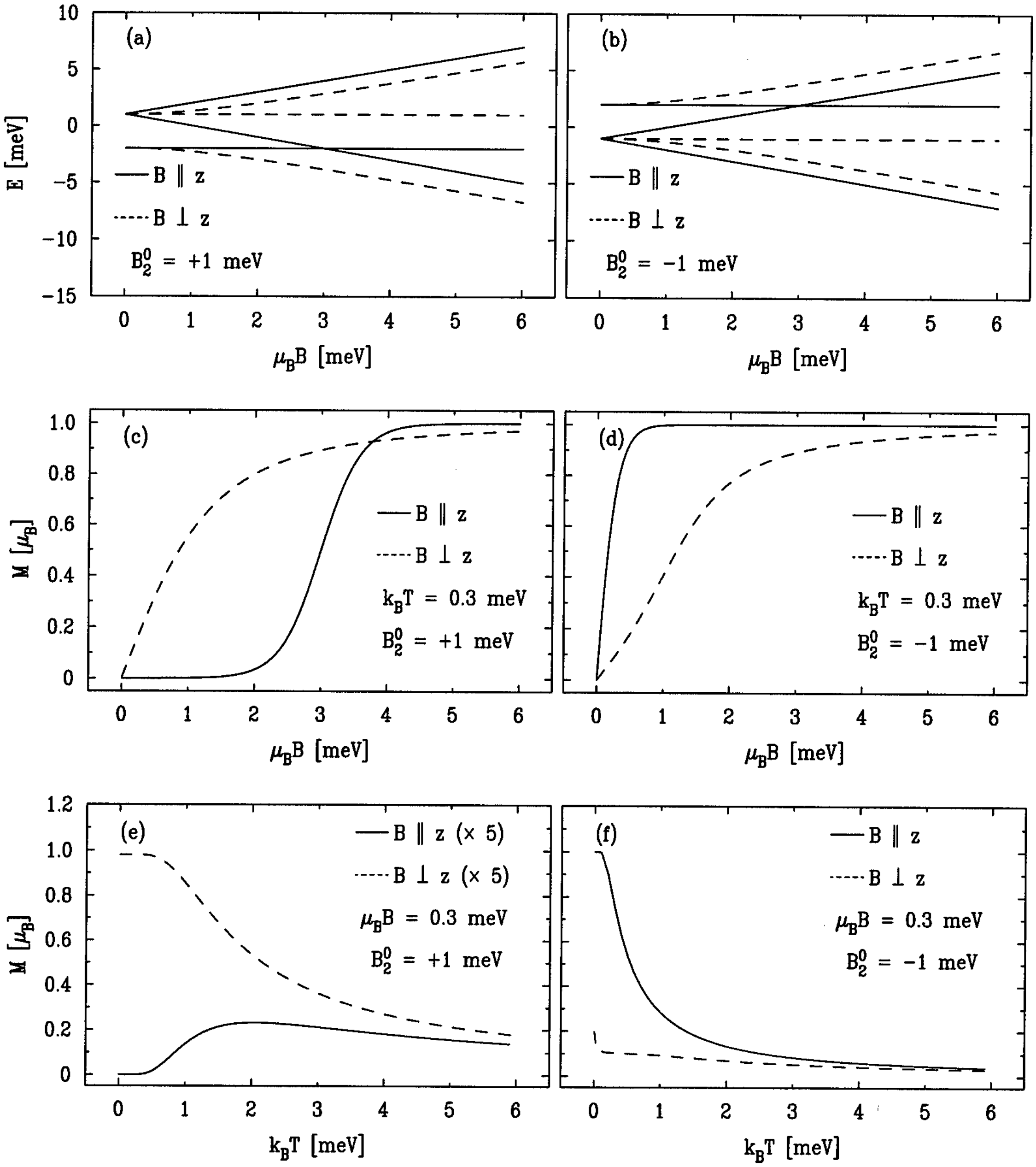

Figure 2.1 Variation of the energy eigenvalues of the Hamiltonian, eq. (2.19), for positive, (a), and negative, (b), values of B_2^0, and the magnetization, eq. (2.20), at constant temperature (c, d) and constant external field (e, f) for this model.

properties in its Hund's rule ground state). The eigenvalues and eigenvectors for this system can be calculated analytically, but the expressions are lengthy. Figure 2.1 plots the energy eigenvalues for this model as a function of the external field. Also displayed are the result of a numerical simulation of the magnetization, eq. (2.20). Our little toy model beautifully reveals the anisotropy induced by the CEF interaction.

Fig. 2.1(a) shows that, in the absence of external fields, for $\mathrm{B}_2^0 > 0$ the ground state is the singlet. For an external field along the z-axis, the energy of this state remains constant, indicating that it has a vanishing magnetic moment. At low temperatures this state dominates the thermodynamic average, and the resulting magnetization is low, as seen in Fig. 2.1(c) and (e). As the field is increased, the Zeeman splitting becomes larger than the CEF splitting, leading to the level crossing shown in Fig. 2.1(a) and the resulting the change in the "easy" magnetization direction (Fig. 2.1 (c)). In a simple mean field model, a mechanism like this may lead to magnetic-magnetic phase transitions or changes of the moment direction as the effective exchange field, $\mathbf{B}_{\text{eff}}$, increases with decreasing temperature. When the field is applied perpendicular to the z-axis, however, the singlet hybridizes with one of the doublet states, so that the ground state has a finite magnetic moment. At low temperatures, again, this level is preferentially populated and therefore the magnetization is mainly determined by the degree of hybridization.

For a negative CEF-coefficient, $\mathrm{B}_2^0 < 0$, the situation is reversed (Fig. 2.1(b),(d), and (f)). For an external field along the z-axis, the high-lying non-magnetic singlet can be neglected and the magnetization resembles that of a free ion with $j = \frac{1}{2}$. When the field is applied perpendicular to the z-axis, the magnetization is lowered by the close proximity of the hybridized-magnetic and non-magnetic partners of the doublet, which cannot be neglected in the thermodynamic average.

The ground state of the free Ho^{3+} ion is $^5I_8$, i.e. it is 17-fold degenerate. In the presence of an electrostatic field with tetragonal symmetry, the ground state splits into

9 singlets ($3A_1$, $2A_2$, $2B_1$ and $2B_2$) and 4 doublets ($4E$, see Table 2.2). These doublets split in the presence of a magnetic field, so that all 17 eigenstates are non-degenerate. The changes of the magnetic behavior upon variation of the CEF parameters and/or the magnetic field are too complex to be discussed here.

3 THEORY OF X-RAY RESONANT EXCHANGE SCATTERING

Resonant effects in the hard x-ray energy range ($\approx 5-20$ keV) appear when the energy of the incident photon, $\hbar\omega_{\mathbf{k}}$, is close to the binding energy of a core level electron. The dominant effect is resonant absorption (see Fig. 3.1), where the core level electron is promoted into an unoccupied state above the Fermi level. This process is exploited in x-ray absorption near edge spectroscopy (XANES), extended x-ray absorption fine structure (EXAFS), circular magnetic x-ray dichroism (CMXD) and related spectroscopic techniques (see ref. [Mat94a] for a recent overview).

Resonant x-ray scattering [Nam85, Gib88, Isa89, Pla70, Blu85, Han88, Car95, Hil96b] occurs when the core level hole and the excited electron recombine under emission of a coherent photon (see Fig. 3.2). Although several inelastic processes involving the recombination of the core hole with other electrons are also possible (Raman scattering)[1], we will consider only elastic scattering.

Due to the localized nature of the core level electron excited in the process, x-ray resonant scattering and absorption techniques probe the local structure of the unoccupied electronic bands above the Fermi level. The discrete binding energies of these low lying electronic states, usually $1s_{1/2}$ (K-edge), $2s_{1/2}$ (L_1-edge), or $2p_{1/2,3/2}$ ($L_{2,3}$ edges) allow element selective measurements of compounds and alloys.

---

[1] Whether these processes are coherent or not is currently subject of intense theoretical and experimental studies [Häm91, Car94]

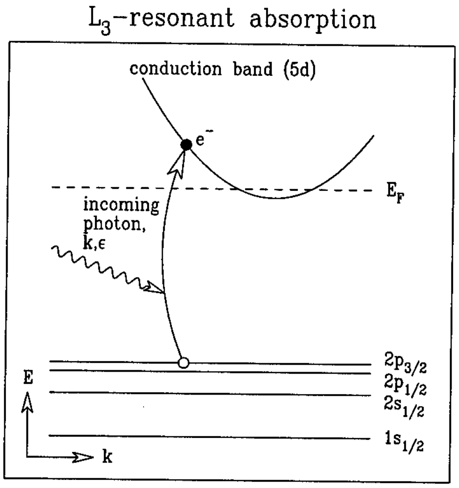

Figure 3.1 Resonant absorption at the L_3 edge of an rare earth element. In the absorption process, an incoming photon with wave vector **k** and polarization ϵ is annihilated and a electron-hole pair is created.

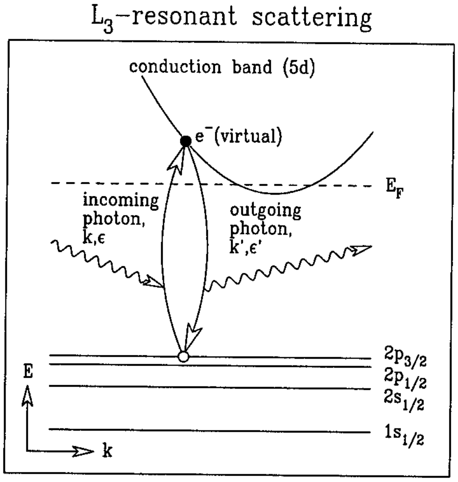

Figure 3.2 Resonant scattering at the L_3 edge of an rare earth element. In the scattering process, an incoming photon with wave vector **k** and polarization ϵ is annihilated and creates a virtual electron-hole pair, which decays under emission of a photon with wave vector $\mathbf{k}'$ and polarization ϵ'.

Fundamentals of magnetic x-ray scattering

The purpose of this section is to explore the x-ray resonant exchange scattering (XRES) cross section and its relation to the magnetic structure of the sample. Our main focus will be directed towards two aspects that have the largest impact on current experiments: The "branching ratio" in rare-earths, i.e. the relative strength of the L_2 and L_3 resonant enhancement in these elements, and the dependence of the intensity and polarization of the scattered beam upon the polarization of the incoming beam and the orientation of the sample.

The bulk of this work is not new. However, we show the intermediate steps in more detail that the original papers [Blu85, Han88, Luo93, Car94], so that the reader might find it easier to follow.

The cross section for scattering from an initial state, $|a, \mathbf{k}, \boldsymbol{\epsilon}\rangle$, into a final state, $|b, \mathbf{k}', \boldsymbol{\epsilon}'\rangle$, is given by eq. (13) of Blume's classic paper [Blu85]:

$$\begin{aligned}
\frac{\mathrm{d}^2\sigma}{\mathrm{d}\Omega \mathrm{d}E'} = & \left(\frac{e^2}{mc^2}\right)^2 \Bigg| \left\langle b \left| \sum_n e^{-i\mathbf{Q}\cdot\mathbf{r}_n} \right| a \right\rangle \boldsymbol{\epsilon}'^{\dagger} \cdot \boldsymbol{\epsilon} \\
& -i\frac{\hbar\omega}{mc^2} \left\langle b \left| \sum_n e^{-i\mathbf{Q}\cdot\mathbf{r}_n}\, \mathbf{s}_n \right| a \right\rangle \boldsymbol{\epsilon}'^{\dagger} \times \boldsymbol{\epsilon} \\
& +\frac{\hbar^2}{m} \sum_{|c\rangle} \frac{\left\langle b \left| M^{\dagger}(\mathbf{k}', \boldsymbol{\epsilon}') \right| c \right\rangle \langle c | M(\mathbf{k}, \boldsymbol{\epsilon}) | a \rangle}{E_a - E_c + \hbar\omega_{\mathbf{k}} - i\Gamma/2} \\
& +\frac{\hbar^2}{m} \sum_{|c\rangle} \frac{\langle b | M(\mathbf{k}, \boldsymbol{\epsilon}) | c \rangle \left\langle c \left| M^{\dagger}(\mathbf{k}', \boldsymbol{\epsilon}') \right| a \right\rangle}{E_a - E_c - \hbar\omega_{\mathbf{k}}} \Bigg|^2 \cdot \\
& \delta(E_a + \hbar\omega_{\mathbf{k}} - E_b - \hbar\omega_{\mathbf{k}'})
\end{aligned} \tag{3.1}$$

Here, $\mathbf{k}$ and $\boldsymbol{\epsilon}$ ($\mathbf{k}'$ and $\boldsymbol{\epsilon}'$) describe the wave vector and polarization of the incoming (outgoing) photon. $\mathbf{Q} = \mathbf{k}' - \mathbf{k}$ is the scattering vector, and the initial, final and intermediate electronic states of the sample are described by a, b, and c, respectively. The four terms are interpreted as Thompson scattering, spin scattering, and resonant scattering with emission of the outgoing photon after and before the absorption of the incident photon, respectively. In eq. (3.1) we used the following abbreviation for the resonant interaction operator:

$$M(\mathbf{k},\boldsymbol{\epsilon}) := \sum_{n} \left(\frac{\boldsymbol{\epsilon} \cdot \mathbf{P}_n}{\hbar} - i\,(\mathbf{k} \times \boldsymbol{\epsilon}) \cdot \mathbf{s}_n \right) e^{i\mathbf{k}\cdot\mathbf{r}_n} \tag{3.2}$$

The position, momentum and spin of the n-th electron are respectively given by $\mathbf{r}_n, \mathbf{P}_n$ and $\mathbf{s}_n$. The summation, n, is taken over all electrons of the solid.

Anomalous dispersion effects occur when the incident photon energy is close to the difference in energy between the initial and the intermediate states, $\hbar\omega \approx E_a - E_c$. In this case, the third term in eq. (3.1) dominates over the second and fourth term, although it is still considerably smaller than the first term. However, Thompson scattering is only observed at discrete scattering vectors. For antiferromagnets, the charge and magnetic Bragg reflections are well separated, so that the third term dominates the magnetic scattering and we need not consider interference effects[2]. Furthermore, we will assume that the scattering process is elastic, $\omega_{\mathbf{k}} \equiv \omega_{\mathbf{k}'}$, and that the initial and final electronic states are identical, $|a\rangle \equiv |b\rangle$. The summation over all electrons, n, is then limited to the "resonating" core level electrons with small energy denominator, typically the different Zeeman levels of the states mentioned above.

$$\begin{aligned} \left(\frac{\mathrm{d}^2\sigma}{\mathrm{d}\Omega \mathrm{d}E'} \right)_{\mathrm{XRES}} &=: \left| F_{\mathrm{XRES}} \right|^2 = \\ = \left(\frac{e^2\hbar^2}{m^2c^2} \right)^2 & \left| \sum_{\substack{|c\rangle \\ E_{|c\rangle}>0}} \frac{\left\langle a \left| M^\dagger(\mathbf{k}',\boldsymbol{\epsilon}') \right| c \right\rangle \left\langle c \left| M(\mathbf{k},\boldsymbol{\epsilon}) \right| a \right\rangle}{E_a - E_c + \hbar\omega_{\mathbf{k}} - i\Gamma/2} \right|^2 \end{aligned} \tag{3.3}$$

To calculate the total scattering cross section, we calculate the matrix elements appearing in the second order perturbation term in the "local" coordinate system of atom N at the

---

[2] Interference between charge and magnetic scattering becomes important in the study of ferromagnetism with circularly polarized radiation.

position $\mathbf{R}_N$, with the $\hat{z}$-axis parallel to the atom's magnetic moment. The summation n is now taken over the "resonating" core level electrons of atom N. The index N will be omitted for these local calculations.

The exponential, $e^{i\mathbf{k}\cdot\mathbf{r}}$, is expanded to first order to include electric dipole (E1), magnetic dipole (M1) and electric quadrupole (E2) interactions:

$$M(\mathbf{k},\boldsymbol{\epsilon}) \;:=\; \sum_N \sum_n e^{i\mathbf{k}\cdot\mathbf{R}_N} \left(\frac{\boldsymbol{\epsilon}\cdot\mathbf{P}_n}{\hbar} - i\,(\mathbf{k}\times\boldsymbol{\epsilon})\cdot\mathbf{s}_n \right) (1 + i\mathbf{k}\cdot\mathbf{r}_n) \tag{3.4}$$

To begin with, we will only consider the first order term, the electric dipole (E1) interaction[3]:

$$M(\mathbf{k},\boldsymbol{\epsilon}) = \sum_N \sum_n e^{i\mathbf{k}\cdot\mathbf{R}_N} \frac{\boldsymbol{\epsilon}\cdot\mathbf{P}_n}{\hbar} \tag{3.5}$$

Note that the electric dipole interaction preserves the spin of the electron, i.e. the spin of the initial and intermediate states are identical.

Using this simplified operator, we may write the resonant scattering amplitude as:

$$\begin{aligned} F_{\mathrm{XRES,E1}} &= \frac{e^2}{m^2c^2} \sum_{\substack{|c\rangle \\ E_{|c\rangle}>0}} \frac{\left\langle a \left| \sum_N e^{-i\mathbf{k}'\cdot\mathbf{R}_N} \sum_n \boldsymbol{\epsilon}'^{\dagger}\cdot\mathbf{P}_n \right| c \right\rangle \left\langle c \left| \sum_N e^{i\mathbf{k}\cdot\mathbf{R}_N} \sum_n \boldsymbol{\epsilon}\cdot\mathbf{P}_n \right| a \right\rangle}{E_a - E_c + \hbar\omega_{\mathbf{k}} - i\Gamma/2} && (3.6) \\ &= \frac{e^2}{m^2c^2} \sum_N e^{-i\mathbf{Q}\cdot\mathbf{R}_N} \sum_n \sum_{\substack{|c\rangle \\ E_{|c\rangle}>0}} \frac{\left\langle a \left| \boldsymbol{\epsilon}'^{\dagger}\cdot\mathbf{P}_n \right| c \right\rangle \left\langle c \left| \boldsymbol{\epsilon}\cdot\mathbf{P}_n \right| a \right\rangle}{E_a - E_c + \hbar\omega_{\mathbf{k}} - i\Gamma/2}, && (3.7) \end{aligned}$$

since the core hole in the intermediate state identifies the excited electron (quantum numbers n and N), and the initial and final states are assumed to be identical (compare Fig. 3.2).

---

[3] Typically, these dominate the x-ray resonances at $L_{2,3}$ absorption edges. However, quadrupolar (E2) terms have been observed, for example at the L_3 edges of Ho [Gib88, Gib91] and Sm in $SmNi_2B_2C$ [Det97], and also at the K edge of Ni in NiO [Hil97], where the dipolar resonances are negligible.

It is more instructive to calculate the scattering of one isolated atom, N, and then perform a summation over all scattering atoms.

$$F_{\mathrm{XRES,E1},N} = \frac{e^2}{m^2c^2} \sum_n \sum_{\substack{|c\rangle \\ E_{|c\rangle}>0}} \frac{\left\langle a \middle| \boldsymbol{\epsilon}'^{\dagger} \cdot \mathbf{P}_n \middle| c \right\rangle \left\langle c \middle| \boldsymbol{\epsilon} \cdot \mathbf{P}_n \middle| a \right\rangle}{E_a - E_c + \hbar\omega_{\mathbf{k}} - i\Gamma/2}, \tag{3.8}$$

so that

$$F_{\mathrm{XRES,E1}} = \sum_N e^{-i\mathbf{Q}\cdot\mathbf{R}_N} F_{\mathrm{XRES,E1},N} \tag{3.9}$$

We have now reduced the expression for the resonant scattering amplitude to a form where we can apply the single electron approximation mentioned above. To further clarify this, we will now take a closer look at the electronic wave functions involved.

Initial/final States

For simplicity we will employ a single electron approximation that neglects many body effects such as exciton binding energies. The many-body ground state wave function, $|a\rangle$, is then replaced by the single-particle wave function of the n-th electron. The spin, orbital and linear momentum operators now act on this single particle wave function only, so that all indices of the operators are dropped.

For resonant scattering in the (hard) x-ray regime, the initial/final electronic states are well-localized core level states. The spin and angular momentum of the electron are then LSJ-coupled and the wave function is best described by atomic quantum numbers: $|a\rangle = \left|n, j, l, (\frac{1}{2}), m_j\right\rangle$. It is not possible to resolve the different m_j-sublevels, since the Zeeman spitting is much smaller than the intrinsic broadening due to the core hole life time, Γ (usually several eV). Therefore, the scattering amplitude is a sum of the partial amplitudes for this group of initial/final states.

In our single electron approximation, the wave function of these states may be written as:

$$\Phi_{n,j,l,m_j}(\mathbf{r}) \quad = \quad \mathcal{R}_{n,j,l}(r)\psi_{j,l,m_j}(\hat{r}) \tag{3.10}$$

To calculate the transition matrix elements, we then expand the angular wave functions into spherical harmonics, $Y_{l,m}$, and eigenfunctions of the spin, χ_{m_s}:

$$\psi_{l\pm\frac{1}{2},l,m_j} \quad = \quad \sum_{m_l}\sum_{m_s} C^{l\pm\frac{1}{2},m_j}_{l,m_l;\frac{1}{2},m_s} Y_{l,m_l}\chi_{m_s} \tag{3.11}$$

The Clebsch-Gordan coefficients are given by:

$$C^{l\pm\frac{1}{2},m_j}_{l,m_j-m_s;\frac{1}{2},m_s} = (2m_s)^{\frac{1\mp 1}{2}}\sqrt{\frac{l+\frac{1}{2}\pm 2m_s m_j}{2l+1}} \tag{3.12}$$

Intermediate States

For the intermediate state, we will assume that the spin, m_s, is a good quantum number. This is a good approximation if the states are delocalized, i.e. the spin-orbit splitting is small. We will characterize the intermediate state by a generalized quantum number, Λ (for a band state, Λ might be written as n, k_x, k_y, k_z), and the spin, m_s.

Since we neglect any spin-orbit interaction[4] in the intermediate states, the wave function may be written as a product of a spatial wave function, $\Psi_\Lambda(\mathbf{r})$, and a spin function, χ_{m_s}. The spatial wave function is also expanded into spherical harmonics.

$$\Psi_\Lambda(\mathbf{r})\chi_{m_s} =: \sum_{l'=0}^{\infty}\sum_{m'_l=-l'}^{l'} \mathcal{R}_{\Lambda,l',m'_l}(r) Y_{l',m'_l}\chi_{m_s}, \tag{3.13}$$

---

[4] Spin-orbit coupling in the intermediate state can be included in a more general formalism, see for example Refs. [Car90, Tho92, Car93, Luo93, Luo94]. The result, however, remains the same when the relative orientation between the spin, s, and the orbital momentum, l, as given by the spin-orbit coupling is taken into account in the final result.

with

$$\mathcal{R}_{\Lambda,l',m_l'}(r) := \int_0^{4\pi} \mathrm{d}\hat{r}\, Y^*_{l',m_l'}(\hat{r})\Psi_\Lambda(\mathbf{r}). \tag{3.14}$$

Matrix elements

Using this characterization of initial/final and intermediate states in the scattering process, we obtain a more specific expression for the resonant magnetic scattering amplitude in electric dipole approximation:

$$\begin{aligned} F_{\mathrm{XRES,E1}} &= \\ &= \frac{e^2\hbar^2}{m^2c^2} \cdot \sum_{|c\rangle} \frac{\langle a|\, M^\dagger(\mathbf{k}',\boldsymbol{\epsilon}')\,|c\rangle \,\langle c|\, M(\mathbf{k},\boldsymbol{\epsilon})\,|a\rangle}{E_{|a\rangle} - E_{|c\rangle} + \hbar\omega_{\mathbf{k}} - i\Gamma/2} && (3.15) \\ &= \frac{e^2\omega_{\mathbf{k}}^2}{c^2} \cdot \sum_N e^{-i\mathbf{Q}\cdot\mathbf{R}_N} \cdot \\ &\quad \cdot \sum_{\substack{\Lambda,m_s \\ E_{|\Lambda,m_s\rangle}>0}} \sum_{m_j} \frac{\left\langle n,j,l,m_j \left|\boldsymbol{\epsilon}'^\dagger\cdot\mathbf{r}\right| \Lambda,m_s\right\rangle \langle \Lambda,m_s\,|\boldsymbol{\epsilon}\cdot\mathbf{r}|\,n,j,l,m_j\rangle}{E_{|n,j,l,m_s\rangle} - E_{|\Lambda,m_s\rangle} + \hbar\omega_{\mathbf{k}} - i\Gamma/2} && (3.16) \end{aligned}$$

The second factor under the summation is identified as the scattering amplitude of a single resonating atom, N.

$$\begin{aligned} F_{\mathrm{XRES,E1},N} &= \\ &= \frac{e^2\omega_{\mathbf{k}}^2}{c^2} \cdot \sum_{\substack{\Lambda,m_s \\ E_{|\Lambda,m_s\rangle}>0}} \sum_{m_j} \frac{\left\langle n,j,l,m_j \left|\boldsymbol{\epsilon}'^\dagger\cdot\mathbf{r}\right| \Lambda,m_s\right\rangle \langle \Lambda,m_s\,|\boldsymbol{\epsilon}\cdot\mathbf{r}|\,n,j,l,m_j\rangle}{E_{|n,j,l,m_s\rangle} - E_{|\Lambda,m_s\rangle} + \hbar\omega_{\mathbf{k}} - i\Gamma/2} && (3.17) \end{aligned}$$

In e.g. a spiral antiferromagnet, there is no clearly defined quantization axis, therefore we will use a local coordinate system with the $\hat{z}$-axis parallel to the magnetic moment of that particular atom, N [Hil96b]. All calculations are done in vector form as a function of the photon polarization vectors, $\boldsymbol{\epsilon}$ and $\boldsymbol{\epsilon}'$, so there is no loss in generality and the scattering terms of different atoms can be combined to find the total scattering cross section.

Using the symbols introduced above, we write the el. dipole matrix element as:

$$\begin{aligned}\langle \Lambda, m_s \,| \boldsymbol{\epsilon} \cdot \mathbf{r} |\, n, j, l, m_j \rangle &= \int\limits_0^\infty r^2 \mathrm{d}r \int\limits_0^{4\pi} \mathrm{d}\hat{r} \sum_{l'=0}^{\infty} \sum_{m_l'=-l'}^{l'} \mathcal{R}^\dagger_{\Lambda,l',m_l'}(r) Y^\dagger_{l',m_l'}(\hat{r}) \chi^\dagger_{m_s} \\ &\quad \cdot (\boldsymbol{\epsilon} \cdot \mathbf{r}) \cdot C^{j,m_j}_{l,m_l;\frac{1}{2},m_s} \mathcal{R}_{n,j,l}(r) Y_{l,m_l}(\hat{r}) \chi_{m_s} \qquad (3.18)\end{aligned}$$

The dipole selection rules allow only transitions with $l' = l \pm 1$ and $m_l' = m_l - 1, m_l, m_l + 1$. We will now assume that only the term with $l' = l + 1$ contributes, due to the much smaller radial matrix elements of the $l' = l - 1$-term (e.g. at the L-absorption edges of rare earths, the $2p \to 5d$ contributions dominate over the $2p \to 6s$ transitions). Furthermore, we write the position vector as a linear combination of spherical harmonics. Using the definitions $\epsilon_1 := \frac{1}{\sqrt{2}}(\epsilon_x + i\epsilon_y)$, $\epsilon_0 := \epsilon_z$, and $\epsilon_{-1} := \frac{1}{\sqrt{2}}(\epsilon_x - i\epsilon_y)$, we find:

$$\boldsymbol{\epsilon} \cdot \mathbf{r} = \sqrt{\frac{4\pi}{3}} \sum_{M=-1}^{1} \epsilon_M Y_{1M}(\hat{r}) \qquad (3.19)$$

The radial contributions to the matrix element are combined into a single symbol:

$$\omega^{m_l'}_{m_s} := \int\limits_0^\infty r^2 \mathrm{d}r \, \mathcal{R}^\dagger_{\Lambda,l',m_l'}(r) \cdot r \cdot \mathcal{R}_{n,j,l}(r) \qquad (3.20)$$

Using the dipole selection rules, the matrix element is now written as:

$$\begin{aligned}&\langle \Lambda, m_s \,| \boldsymbol{\epsilon} \cdot \mathbf{r} |\, n, j, l, m_j \rangle = \\ &= \sqrt{\frac{4\pi}{3}} \sum_{M=-1}^{1} \sum_{\substack{m_l \\ m_l'}} \epsilon_M \cdot \omega^{m_l'}_{m_s} \cdot C^{l',m_l'}_{l,m_l;1,M} C^{j,m_j}_{l,m_l;\frac{1}{2},m_s} \qquad (3.21) \\ &= \sqrt{\frac{4\pi}{3}} \sum_{M=-1}^{1} \epsilon_M \cdot \omega^{m_j - m_s + M}_{m_s} \cdot C^{l',m_j-m_s+M}_{l,m_j-m_s;1,M} C^{j,m_j}_{l,m_j-m_s;\frac{1}{2},m_s}, \qquad (3.22)\end{aligned}$$

noticing that the Clebsch-Gordan coefficients vanish unless $m_j = m_l + m_s$ and $m_l' = m_l + M$.

After summation over all initial and final states, we obtain the following expression for the scattering amplitude in the electric dipole approximation of second order perturbation theory:

$$\begin{aligned} F_{\mathrm{XRES,E1},N} &= \sum_{m_s}\sum_{m_j}\sum_{M=-1}^{1} \left({\epsilon'_M}^{\dagger} \cdot \epsilon_M\right) \cdot A_{m_s}^{m_j-m_s+M} \left|C_{l,m_j-m_s;1,M}^{l',m_j-m_s+M}\right|^2 \left|C_{l,m_j-m_s;\frac{1}{2},m_s}^{j,m_j}\right|^2 && (3.23) \\ &= \sum_{M=-1}^{1} \left({\epsilon'_M}^{\dagger} \cdot \epsilon_M\right) \cdot F_{1M}, && (3.24) \end{aligned}$$

with

$$A_{m_s}^{m_l'} = A_{m_s}^{m_j-m_s+M} := \sum_{\substack{\Lambda \\ E_{|\Lambda,m_s\rangle}>0}} \frac{4\pi}{3} \cdot \frac{\left|\omega_{m_s}^{m_j-m_s+M}\right|^2}{E_{|n,j,l,m_j\rangle} - E_{|\Lambda,m_s\rangle} + \hbar\omega_{\mathbf{k}} - i\Gamma/2} \qquad (3.25)$$

and, to make the connection to Hannon's notation [Han88],

$$F_{1M} = \frac{e^2\omega_{\mathbf{k}}^2}{c^2} \sum_{m_s}\sum_{m_j} A_{m_s}^{m_j-m_s+M} \left|C_{l,m_j-m_s;1,M}^{l',m_j-m_s+M}\right|^2 \left|C_{l,m_j-m_s;\frac{1}{2},m_s}^{j,m_j}\right|^2 . \qquad (3.26)$$

We now turn our attention towards the polarization dependence. Notice that, in the "global" coordinate system, the quantization direction, $\hat{z}$, can be a unit vector in any direction.

$$\begin{aligned} \epsilon'^{\dagger}_{1}\epsilon_1 &= \frac{1}{2}\left({\epsilon'_x}^{\dagger}\epsilon_x + {\epsilon'_y}^{\dagger}\epsilon_y + i{\epsilon'_x}^{\dagger}\epsilon_y - i{\epsilon'_y}^{\dagger}\epsilon_x\right) && (3.27) \\ &= \frac{1}{2}\left(\boldsymbol{\epsilon}'^{\dagger} \cdot \boldsymbol{\epsilon} - (\boldsymbol{\epsilon}'^{\dagger} \cdot \hat{z})(\boldsymbol{\epsilon} \cdot \hat{z}) + i(\boldsymbol{\epsilon}'^{\dagger} \times \boldsymbol{\epsilon}) \cdot \hat{z}\right) && (3.28) \\ \epsilon'^{\dagger}_{0}\epsilon_0 &= {\epsilon'_z}^{\dagger}\epsilon_z && (3.29) \\ &= (\boldsymbol{\epsilon}'^{\dagger} \cdot \hat{z})(\boldsymbol{\epsilon} \cdot \hat{z}) && (3.30) \\ \epsilon'^{\dagger}_{-1}\epsilon_{-1} &= \frac{1}{2}\left({\epsilon'_x}^{\dagger}\epsilon_x + {\epsilon'_y}^{\dagger}\epsilon_y - i{\epsilon'_x}^{\dagger}\epsilon_y + i{\epsilon'_y}^{\dagger}\epsilon_x\right) && (3.31) \\ &= \frac{1}{2}\left(\boldsymbol{\epsilon}'^{\dagger} \cdot \boldsymbol{\epsilon} - (\boldsymbol{\epsilon}'^{\dagger} \cdot \hat{z})(\boldsymbol{\epsilon} \cdot \hat{z}) - i(\boldsymbol{\epsilon}'^{\dagger} \times \boldsymbol{\epsilon}) \cdot \hat{z}\right) && (3.32) \end{aligned}$$

Using this vector notation, equation (3.24) is now rewritten as:

$$\begin{aligned} F_{\mathrm{XRES,E1},N} &= (\boldsymbol{\epsilon}'^{\dagger} \cdot \boldsymbol{\epsilon})\left[F_{11} + F_{1-1}\right] \\ &\quad -i(\boldsymbol{\epsilon}'^{\dagger} \times \boldsymbol{\epsilon}) \cdot \hat{z}_N \left[F_{11} - F_{1-1}\right] \\ &\quad +(\boldsymbol{\epsilon}'^{\dagger} \cdot \hat{z}_N)(\boldsymbol{\epsilon} \cdot \hat{z}_N)\left[-F_{11} + 2F_{10} - F_{1-1}\right] \qquad (3.33) \\ &= (\boldsymbol{\epsilon}'^{\dagger} \cdot \boldsymbol{\epsilon})F^{(0)} - i(\boldsymbol{\epsilon}'^{\dagger} \times \boldsymbol{\epsilon}) \cdot \hat{z}_N F^{(1)} + (\boldsymbol{\epsilon}'^{\dagger} \cdot \hat{z}_N)(\boldsymbol{\epsilon} \cdot \hat{z}_N)F^{(2)}. \qquad (3.34) \end{aligned}$$

We have reintroduced the index N to remind ourselves that the unit vector $\hat{z}_N$ describes the local moment direction at the N-th atom. The coefficients $F^{(0,1,2)}$ describe the scattering amplitude proportional to 1, $\hat{z}_N$ and $\hat{z}_N^2$, respectively [Hil96b].

All that is left to do now is to perform the summation over all scattering atoms, eq. (3.9):

$$\begin{aligned} F_{\mathrm{XRES,E1}} &= \sum_N e^{-i\mathbf{Q}\cdot\mathbf{R}_N} F_{\mathrm{XRES,E1},N} \qquad (3.35) \\ &= \sum_N e^{-i\mathbf{Q}\cdot\mathbf{R}_N} \left((\boldsymbol{\epsilon}'^{\dagger} \cdot \boldsymbol{\epsilon})F^{(0)} - i(\boldsymbol{\epsilon}'^{\dagger} \times \boldsymbol{\epsilon}) \cdot \hat{z}_N F^{(1)} + (\boldsymbol{\epsilon}'^{\dagger} \cdot \hat{z}_N)(\boldsymbol{\epsilon} \cdot \hat{z}_N)F^{(2)}\right). \qquad (3.36) \end{aligned}$$

Having completed the math to derive this well-known expression for the resonant scattering amplitude, it is now time to interpret our results. Three points are of major importance: The relation between the amplitude factors, $F^{(0,1,2)}$, and the magnetic properties of the scattering atom, N. The dependence of the scattering amplitude on the local moment directions, i.e. the proportionality of the three terms to 1, $\hat{z}_N$, and $\hat{z}_N^2$, and their dependence on the scattering geometry, i.e. the polarization vectors, $\boldsymbol{\epsilon}$ and $\boldsymbol{\epsilon}'$.

Interpretation of the amplitude terms

Even for the electric dipole scattering amplitude, a complete evaluation of the amplitude terms and their relation to the local magnetic properties is exceedingly complex, and thus beyond the scope of this work. We refer the interested reader to the work of Luo [Luo93, Luo94].

It is possible, however, to illustrate the underlying physical concepts. For this we have to make some approximations that are generally not applicable in real, physical situations.

- To simulate a magnetically polarized conduction band, we assume that orbital momentum is a good quantum number ($\Lambda = l', m_l'$). The spin and orbital momentum of the conduction band are then given by the sum of the m_s' and m_l' quantum numbers over all occupied states in the conduction band:

$$\begin{aligned}
\langle s_z \rangle &= \sum_{\substack{l', m_l', m_s' \\ E_{|l', m_l', m_s'\rangle} < 0}} \hbar m_s' && (3.37) \\
&= \sum_{l', m_l'} \sum_{m_s'} \hbar m_s' \cdot \Theta(-E_{|l', m_l', m_s'\rangle}). && (3.38) \\
\langle l_z \rangle &= \sum_{\substack{l', m_l', m_s' \\ E_{|l', m_l', m_s'\rangle} < 0}} \hbar m_l' && (3.39) \\
&= \sum_{l', m_l'} \sum_{m_s'} \hbar m_l' \cdot \Theta(-E_{|l', m_l', m_s'\rangle}). && (3.40)
\end{aligned}$$

Notice that in the case dipolar XRES of rare earth elements, only the moment of the $5d$ band is probed, while the bulk of the magnetic moment resides in the $4f$ electrons, i.e. the summation over the quantum number l' is omitted. However, the magnetic polarization of the $5d$ band is usually caused through direct exchange with the $4f$ electrons. Furthermore, XRES probes the *unoccupied* states of the conduction band, so that the *negative* magnetic momenta are measured[5].

---

[5] The sum of magnetic momenta of the occupied and unoccupied states vanishes, since the spin and angular momentum of any filled shell is zero.

- We will assume that the band width of intermediate states is much smaller that the intrinsic broadening. This allows us to factor the scattering amplitude into a common resonant energy denominator and a sum of matrix elements.

- The radial matrix elements, $\omega^{m_l'}_{m_s}$, are taken to be *identical* for all transitions.

With these three approximations, the amplitude factors, $A^{m_l'}_{m_s}$, become simple prefactors, multiplied by the number of unoccupied states with quantum numbers $m_l' = m_j - m_s + M$ and $m_s' = m_s$, which is either 0 or 1. We can now further simplify equation (3.26).

$$F_{1M} = \frac{e^2\omega_{\mathbf{k}}^2}{c^2} A \sum_{m_s}\sum_{m_j} \left|C^{l',m_j-m_s+M}_{l,m_j-m_s;1,M}\right|^2 \left|C^{j,m_j}_{l,m_j-m_s;\frac{1}{2},m_s}\right|^2 \Theta(E_{|l',m_l',m_s'\rangle}), \tag{3.41}$$

where $j = l \pm \frac{1}{2}$. In this approximation, the amplitude factor for the first order term, $F^{(1)} = F_{11} - F_{1-1}$ is given by:

$$\begin{aligned} F^{(1)} &= F_{11} - F_{1-1} \qquad (3.42) \\ &= \frac{e^2\omega_{\mathbf{k}}^2}{c^2} A \sum_{m_s}\sum_{m_j} \left|C^{l',m_j-m_s+1}_{l,m_j-m_s;1,1}\right|^2 \left|C^{j,m_j}_{l,m_j-m_s;\frac{1}{2},m_s}\right|^2 \\ &\quad \cdot \left[\Theta(E_{|l',m_l',m_s'\rangle}) - \Theta(E_{|l',-m_l',-m_s'\rangle})\right] \qquad (3.43) \\ &= \frac{e^2\omega_{\mathbf{k}}^2}{c^2} A \sum_{m_s}\sum_{m_j} \frac{(l+m_l')(l+1+m_l')}{2(l+1)(2l+1)} \cdot \frac{(2l+1) \pm 4m_s'(m_l'+m_s'-1)}{2(2l+1)} \\ &\quad \cdot \left[\Theta(E_{|l',m_l',m_s'\rangle}) - \Theta(E_{|l',-m_l',-m_s'\rangle})\right] \qquad (3.44) \end{aligned}$$

where $m_l' = m_j - m_s + 1$.

This expression is — apart from some constant prefactors — identical to the absorption cross section for circular magnetic x-ray dichroism (CMXD), as developed by Carra *et al.* [Car90, Tho92, Car93, Kön96b], so that the CMXD-sum rules also apply for XRES. Unfortunately, the inversion of the sum rules is generally not possible in the antiferromagnetic scattering geometry, since only the magnitude of the scattering amplitude is measured, while it is not possible to determine the sign. However, we may use them to explain the general trend in the magnetic scattering intensities observed at the $L_{2,3}$ absorption edges of rare-earth compounds [Wat96b]:

For $l = 0$ and $j = \frac{1}{2}$, eq. 3.44 reduces to:

$$\begin{aligned} F^{(1)} &= \frac{e^2\omega_{\mathbf{k}}^2}{c^2} A \sum_{m_s} \sum_{m_j} m_l' \Theta(E_{|l',m_l',m_s'\rangle}) && (3.45) \\ &= -\frac{e^2\omega_{\mathbf{k}}^2}{c^2} A \langle l_z \rangle \, . && (3.46) \end{aligned}$$

The electronic transitions at K-absorption edges couple to highly delocalized states in the p-symmetry conduction band. The resonance is sensitive to the orbital momentum — which is typically quenched — but not to the spin polarization, therefore dipolar resonances at K-edges are usually very weak.

At L_3-absorption edges, spin and orbital momentum contribute “in phase”, so that the largest resonances are observed when the components couple parallelly, $j = l + s$, while at L_2-absorption edges, spin and orbital momentum contribute “out of phase”, so that the largest resonances are observed when the components couple antiparallelly, $j = l - s$.

Consequently, in light rare-earths ($j = l - s$), the resonant enhancement at L_2 absorption edges is generally much stronger than at L_3 edges. For the heavy rare-earths ($j = l + s$), the situation is reversed, while for Gd and Eu^{2+} ($l = 0$) the enhancements at the L_2 and L_3 edges are comparable [Det96, Isl00a]. This trend is also observed in CMXD [Fis93].

Formation of satellite peaks

We will now calculate an example to demonstrate the formation of satellites peaks. To do this, we have to perform the summation of the single-atom scattering amplitudes over the whole crystal lattice as given in eq. (3.36).

Let us assume that the antiferromagnetic structure of some material can be characterized by two vectors, a modulation wave vector, $\mathbf{q}$, and a vector that specifies the orientation of the magnetic moments, $\mathbf{z}_0$. Notice that cyclic structures may require a complex orientation vector. The magnetic moment, $\hat{z}_N$, for the N-th atom at the position $\mathbf{R}_N$ is then given by[6]

$$\begin{aligned} \hat{z}_N &= \Re\left[\mathbf{z}_0 e^{i\mathbf{q}\cdot\mathbf{R}_N}\right] && (3.47) \\ &= \frac{1}{2}\left(e^{i\mathbf{q}\cdot\mathbf{R}_N}\mathbf{z}_0 + e^{-i\mathbf{q}\cdot\mathbf{R}_N}\mathbf{z}_0^\dagger\right). && (3.48) \end{aligned}$$

The total E1-resonant scattering amplitude for this case is then given by:

$$\begin{aligned} F_{\mathrm{XRES,E1},N} &= \sum_N e^{-i\mathbf{Q}\cdot\mathbf{R}_N}\Big((\boldsymbol{\epsilon}'^\dagger\cdot\boldsymbol{\epsilon})F^{(0)} \\ &\qquad -i(\boldsymbol{\epsilon}'^\dagger\times\boldsymbol{\epsilon})\cdot\hat{z}_N F^{(1)} \\ &\qquad +(\boldsymbol{\epsilon}'^\dagger\cdot\hat{z}_N)(\boldsymbol{\epsilon}\cdot\hat{z}_N)F^{(2)}\Big) && (3.49) \\ &= F^{(0)}\sum_N e^{-i\mathbf{Q}\cdot\mathbf{R}_N}(\boldsymbol{\epsilon}'^\dagger\cdot\boldsymbol{\epsilon}) \\ &\quad -iF^{(1)}\sum_N e^{-i\mathbf{Q}\cdot\mathbf{R}_N}(\boldsymbol{\epsilon}'^\dagger\times\boldsymbol{\epsilon})\cdot\Re\left[\mathbf{z}_0 e^{i\mathbf{q}\cdot\mathbf{R}_N}\right] \\ &\quad +F^{(2)}\sum_N e^{-i\mathbf{Q}\cdot\mathbf{R}_N}(\boldsymbol{\epsilon}'^\dagger\cdot\Re\left[\mathbf{z}_0 e^{i\mathbf{q}\cdot\mathbf{R}_N})\right]\,(\boldsymbol{\epsilon}\cdot\Re\left[\mathbf{z}_0 e^{i\mathbf{q}\cdot\mathbf{R}_N})\right] && (3.50) \\ &= F^{(0)}\left[\sum_N e^{-i\mathbf{Q}\cdot\mathbf{R}_N}\right](\boldsymbol{\epsilon}'^\dagger\cdot\boldsymbol{\epsilon}) \end{aligned}$$

---

[6] For a collinear structure, this formula gives an amplitude modulation of the "unit" vector, $\hat{z}_N$. The proper treatment would be to assume a modulation of the amplitude terms, $F_N^{(1)} \propto \mu_N$ and $F_N^{(2)} \propto \mu_N^2$, at a constant $\hat{z}_N$. For our treatment here we absorb the amplitude modulation into $\hat{z}_N$ and implicitly take $F^{(}1)$ and $F(2)$ as their maximum values.

$$
\begin{aligned}
&+\frac{1}{4}F^{(2)}\left[\sum_N e^{-i\mathbf{Q}\cdot\mathbf{R}_N}\right]\left[\left(\boldsymbol{\epsilon}'^{\dagger}\cdot\mathbf{z}_0^{\dagger}\right)\left(\boldsymbol{\epsilon}\cdot\mathbf{z}_0\right)+\left(\boldsymbol{\epsilon}'^{\dagger}\cdot\mathbf{z}_0\right)\left(\boldsymbol{\epsilon}\cdot\mathbf{z}_0^{\dagger}\right)\right]\\
&-\frac{i}{2}F^{(1)}\left[\sum_N e^{-i(\mathbf{Q}-\mathbf{q})\cdot\mathbf{R}_N}\right]\left(\boldsymbol{\epsilon}'^{\dagger}\times\boldsymbol{\epsilon}\right)\cdot\mathbf{z}_0\\
&-\frac{i}{2}F^{(1)}\left[\sum_N e^{-i(\mathbf{Q}+\mathbf{q})\cdot\mathbf{R}_N}\right]\left(\boldsymbol{\epsilon}'^{\dagger}\times\boldsymbol{\epsilon}\right)\cdot\mathbf{z}_0^{\dagger}\\
&+\frac{1}{4}F^{(2)}\left[\sum_N e^{-i(\mathbf{Q}-2\mathbf{q})\cdot\mathbf{R}_N}\right]\left(\boldsymbol{\epsilon}'^{\dagger}\cdot\mathbf{z}_0\right)\left(\boldsymbol{\epsilon}\cdot\mathbf{z}_0\right)\\
&+\frac{1}{4}F^{(2)}\left[\sum_N e^{-i(\mathbf{Q}+2\mathbf{q})\cdot\mathbf{R}_N}\right]\left(\boldsymbol{\epsilon}'^{\dagger}\cdot\mathbf{z}_0^{\dagger}\right)\left(\boldsymbol{\epsilon}\cdot\mathbf{z}_0^{\dagger}\right)
\end{aligned}
\tag{3.51}
$$

Looking at the exponential factors summed over all atoms in the crystal, we can now see the emergence of satellite peaks. The scattering amplitude vanishes, unless a generalized Bragg condition is fulfilled: $\mathbf{Q} = \mathbf{G} - 2\mathbf{q}$; $\mathbf{G} - \mathbf{q}$, $\mathbf{G}$, $\mathbf{G} + \mathbf{q}$, or $\mathbf{G} + 2\mathbf{q}$, where $\mathbf{G}$ is a reciprocal lattice vector. Thus, the electric dipole contributions to the resonant scattering amplitude give rise to satellites up to second harmonic order, even if the magnetic structure is perfectly sinusoidal. The amplitude factor $F^{(1)}$ contributes only to the fundamental satellites, while the second order factor, $F^{(2)}$, contributes to both the second harmonic satellites and the scattering at the charge peak's position — even for incommensurate systems.

We also point out, but do not show, that the quadrupolar (E2) XRES cross section [Hil96b] contains terms of up to fourth order in $\hat{z}_N$. Thus interference between the first order ($F^{(1)}_{E2}$) and third order ($F^{(3)}_{E2}$) terms, with a relative weight[7] of 4 : 3, will be observed at the position of the fundamental satellite, $\mathbf{G} \pm \mathbf{q}$ [Det97]. Similarly, second ($F^{(2)}_{E2}$) and fourth ($F^{(4)}_{E2}$) order terms (relative weight 1:1) contribute to the second harmonic satellite peak at $\mathbf{G} \pm 2\mathbf{q}$.

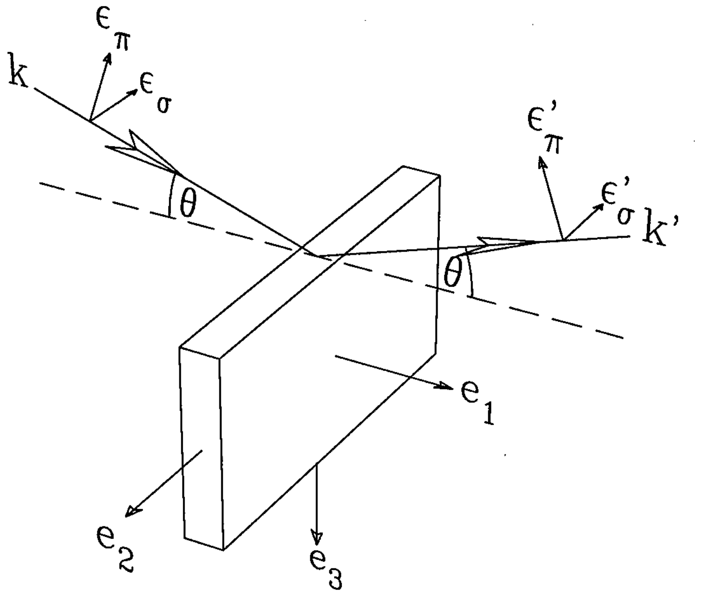

Figure 3.3 The coordinate system used for our calculations of the resonant scattering amplitude. $\mathbf{k}$ and $\mathbf{k}'$ are the incident and scattered wave vectors and 2θ is the scattering angle. $\boldsymbol{\epsilon}_\sigma$ and $\boldsymbol{\epsilon}_\pi$ are the components of the polarization perpendicular and parallel to the diffraction plane (spanned by $\mathbf{k}$ and $\mathbf{k}'$). The coordinate system, $\mathbf{e}_{1,2,3}$, is defined by the incident and scattered wave vectors: $\mathbf{e}_1 := (\hat{\mathbf{k}} + \hat{\mathbf{k}}')/2\cos\theta$, $\mathbf{e}_2 := \hat{\mathbf{k}} \times \hat{\mathbf{k}}'/\sin 2\theta$, and $\mathbf{e}_3 = (\hat{\mathbf{k}} - \hat{\mathbf{k}}')/2\sin\theta$.

Scattering geometry

We now choose an appropriate coordinate system, according to the convention of Blume and Gibbs [Blu88, Hil96b], as displayed in Fig. 3.3. The unit vectors $\hat{\mathbf{e}}_1$ and $\hat{\mathbf{e}}_3$ define the scattering plane, with $\mathbf{Q} := \mathbf{k}' - \mathbf{k} \parallel \hat{\mathbf{e}}_3$. In this coordinate system, the relevant vectors can be written as:

$$\mathbf{k} = k \cdot \begin{pmatrix} \cos\theta \\ 0 \\ -\sin\theta \end{pmatrix} \tag{3.52}$$

$$\mathbf{k}' = k \cdot \begin{pmatrix} \cos\theta \\ 0 \\ \sin\theta \end{pmatrix} \tag{3.53}$$

$$\boldsymbol{\epsilon} = \epsilon_\sigma \begin{pmatrix} 0 \\ -1 \\ 0 \end{pmatrix} + \epsilon_\pi \begin{pmatrix} -\sin\theta \\ 0 \\ -\cos\theta \end{pmatrix} \tag{3.54}$$

$$\boldsymbol{\epsilon}' = \epsilon'_\sigma \begin{pmatrix} 0 \\ -1 \\ 0 \end{pmatrix} + \epsilon'_\pi \begin{pmatrix} \sin\theta \\ 0 \\ -\cos\theta \end{pmatrix} \tag{3.55}$$

ϵ_σ and ϵ_π describe the components perpendicular and parallel to the scattering plane, with $|\epsilon_\sigma|^2 + |\epsilon_\pi|^2 = 1$. Note that, in the case of circular or elliptical polarization, these parameters assume complex values.

Any bilinear function of the two polarization vectors may be written in matrix form:

---

[7] The relative weight of 4:3 is only valid if the local moment direction is defined as in eq. (3.47). If the prefactor $\frac{1}{2}$ in eq. (3.48) is absorbed into $\mathbf{z}_0$, the relative weight becomes 1:3 for the fundamental satellite, and 1:4 for the second harmonic satellite.

$$f\left[\boldsymbol{\epsilon}'^{\dagger}, \boldsymbol{\epsilon}\right] = \begin{pmatrix} \epsilon'^{\dagger}_{\sigma} \\ \epsilon'^{\dagger}_{\pi} \end{pmatrix}^{T} \cdot \begin{pmatrix} M_{\sigma\to\sigma} & M_{\pi\to\sigma} \\ M_{\sigma\to\pi} & M_{\pi\to\pi} \end{pmatrix} \cdot \begin{pmatrix} \epsilon_{\sigma} \\ \epsilon_{\pi} \end{pmatrix} \tag{3.56}$$

In this geometry, we find the following geometry matrices:

$$M\left[\boldsymbol{\epsilon}'^{\dagger} \cdot \boldsymbol{\epsilon}\right] = \begin{pmatrix} 1 & 0 \\ 0 & \hat{k}' \cdot \hat{k} \end{pmatrix} \tag{3.57}$$

$$= \begin{pmatrix} 1 & 0 \\ 0 & \cos 2\theta \end{pmatrix} \tag{3.58}$$

$$M\left[(\boldsymbol{\epsilon}'^{\dagger} \times \boldsymbol{\epsilon}) \cdot \hat{z}\right] = \begin{pmatrix} 0 & -\hat{k}' \cdot \hat{z} \\ \hat{k} \cdot \hat{z} & (\hat{k} \times \hat{k}') \cdot \hat{z} \end{pmatrix} \tag{3.59}$$

$$= \begin{pmatrix} 0 & z_1 \cos\theta + z_3 \sin\theta \\ -z_1 \cos\theta + z_3 \sin\theta & -z_2 \sin 2\theta \end{pmatrix} \tag{3.60}$$

$$M\left[(\boldsymbol{\epsilon}'^{\dagger} \cdot \hat{z})(\boldsymbol{\epsilon} \cdot \hat{z})\right] =$$

$$= \frac{1}{\sin^2 2\theta} \begin{pmatrix} \left[(\hat{k}' \times \hat{k}) \cdot \hat{z}\right]^2 & \begin{matrix}\left[\hat{k}'\cdot\hat{z} - (\hat{k}'\cdot\hat{k})\hat{k}\cdot\hat{z}\right]\cdot \\ (\hat{k}'\cdot\hat{k})\cdot\hat{z}\end{matrix} \\ \begin{matrix}\left[(\hat{k}'\cdot\hat{k})\hat{k}'\cdot\hat{z} - \hat{k}\cdot\hat{z}\right]\cdot \\ (\hat{k}'\cdot\hat{k})\cdot\hat{z}\end{matrix} & \begin{matrix}(\hat{k}'\cdot\hat{k})\left[(\hat{k}'\cdot\hat{z})^2 + (\hat{k}\cdot\hat{z})^2\right] \\ -\left[1 + (\hat{k}'\cdot\hat{k})^2\right]\left[(\hat{k}'\cdot\hat{z})(\hat{k}\cdot\hat{z})\right]\end{matrix} \end{pmatrix}$$

$$= \begin{pmatrix} z_2^2 & z_2\left(-z_1 \sin\theta + z_3 \cos\theta\right) \\ z_2\left(z_1 \sin\theta + z_3 \cos\theta\right) & z_1^2\left(\cos^2\theta - 1\right) + z_3^2 \cos^2\theta \end{pmatrix} \tag{3.61}$$

Note that these geometry terms depend on the orientation and polarization of the incoming and outgoing beams with respect to the sample. This is a manifestation of the more complicated interaction giving rise to resonant scattering. Charge scattering is only sensitive to the charge density in the sample. The interaction is scalar, so that the scattering amplitude depends on the scattering vector, $\mathbf{Q} = \mathbf{k}' - \mathbf{k}$, only[8]. Electric dipole resonant scattering, on the other hand, arises from a combination of two vector

---

[8] Explicit dependence on the azimuthal angle, ψ, appears when multiple scattering effects are taken into account (dynamical theory, see refs. [Ewa17, Ewa37, Bat64, Ewa65]).

densities, $\mathbf{P}_n$. It therefore contains scalar, pseudo-vector and second-rank tensor terms. These are observed at the position of charge reflections, fundamental and second order harmonic satellites, respectively. Electric quadrupole resonant scattering originates in a combination of two second rank tensors that combine to tensors of rank up to four. Accordingly, magnetic satellites up to fourth harmonic order are observed.

Time reversal symmetry

Upon time reversal, the incident and scattered wave vectors and polarizations are switched, $\mathbf{k}' \leftrightarrow \mathbf{k}$, $\boldsymbol{\epsilon}' \leftrightarrow \boldsymbol{\epsilon}$, and the local moment direction is reversed, $\hat{z} \rightarrow -\hat{z}$. The $\sigma \rightarrow \sigma$ and $\pi \rightarrow \pi$ elements of the geometry matrices have to be invariant, while the transformation switches the $\sigma \rightarrow \pi$ and $\pi \rightarrow \sigma$ elements. Eq. (3.36) evidently satisfies time reversal symmetry, as can be verified using the vector notation of the geometry matrices.

Non-resonant magnetic x-ray scattering

Compared to the non-resonant x-ray scattering regime [deB72, Gib86, Blu88], the resonant enhancement yields higher scattered beam intensities and better signal to noise ratios. However, large resonant enhancements can be utilized only at $L_{2,3}$ and $M_{2,3,4,5}$ absorption edges. While the rare-earth elements are ideally suitable for this technique — their $L_{2,3}$-edges lie between 5 and 11 keV — it cannot be applied to the technologically important 3*d* transition metals, e.g. V, Mn, Fe, Co, Ni and Cu, for which the L absorption edges lie below 1.2 keV. Materials of current interest based on these elements are, for example, the CMR (Collosal magneto-resistance) manganites, magnetic multilayers for data storage devices, and the cuprate high-T_C superconductors. A further disadvantage of resonant x-ray techniques is that, since the resonances occur at *absorption edges*, the penetration depth of the x-rays is very small. Therefore resonant scattering probes only the magnetic structure near the surface, while most of the incident x-ray intensity is absorbed in the same volume. In samples with very small thermal conductivity, like superconductors, this may lead to local heating problems, as we experienced in our studies of $HoNi_2B_2C$ [Hil96a]. Finally, E1-XRES measurements of rare-earth materials are sensitive only to the magnetization of the $5d$ electrons, not to the $4f$ states where the bulk of the magnetic moment originates.

These drawbacks can be avoided by a different choice of the photon energy, i.e. using non-resonant magnetic x-ray scattering [deB72, deB81b, Gib85, Blu88, Brü96]. In particular, the penetration depth can be greatly increased by using hard x-rays with photon energies in the range from 40 to 80 keV [Str96].

The scattering cross section for non-resonant scattering have been calculated in detail by Blume and Gibbs [Blu88]. The magnetic scattering amplitude is given by [Blu88]:

$$F_{\text{mag}} = -i\frac{\hbar\omega}{mc^2} \cdot \left(\frac{e^2}{mc^2}\right) \cdot \sum_N e^{-i\mathbf{Q}\cdot\mathbf{R}_N} \left[\frac{1}{2}\mathbf{L}(\mathbf{Q}) \cdot \mathbf{A} + \mathbf{S}(\mathbf{Q}) \cdot \mathbf{B}\right], \qquad (3.62)$$

where $\mathbf{R}_N$ is the position of the N-th unit cell. $\mathbf{S}(\mathbf{Q})$ and $\mathbf{L}(\mathbf{Q})$ are the Fourier transforms [Tra53] of the spin and orbital magnetization densities in the unit cell, respectively. They may be approximated by:

$$\mathbf{S}(\mathbf{Q}) = \sum_n \mathbf{S}_n f_{n,S}(Q) e^{i\mathbf{Q}\cdot\mathbf{r}_n} \qquad (3.63)$$

$$\mathbf{L}(\mathbf{Q}) = \sum_n \mathbf{L}_n f_{n,L}(Q) e^{i\mathbf{Q}\cdot\mathbf{r}_n}, \qquad (3.64)$$

where $\mathbf{r}_n$ is the position of the n-th magnetic atom in a unit cell, $f_{n,S(L)}(Q)$ are the magnetic spin (angular) momentum form factors, and $\mathbf{S}_n$ ($\mathbf{L}_n$) is the total spin (orbital) angular momentum of the n-th atom. The vectors $\mathbf{A}$ and $\mathbf{B}$ describe the scattering geometry:

$$\begin{aligned}
\mathbf{A} &= 2(1-\hat{k}\cdot\hat{k}')(\boldsymbol{\epsilon}'^{\dagger}\times\boldsymbol{\epsilon})-(\hat{k}\cdot\boldsymbol{\epsilon}'^{\dagger})(\hat{k}\times\boldsymbol{\epsilon})+(\hat{k}'\times\boldsymbol{\epsilon}'^{\dagger})(\hat{k}'\cdot\boldsymbol{\epsilon}) && (3.65)\\
\mathbf{B} &= \boldsymbol{\epsilon}'^{\dagger}\times\boldsymbol{\epsilon}+(\hat{k}'\times\boldsymbol{\epsilon}'^{\dagger})(\hat{k}'\cdot\boldsymbol{\epsilon})-(\hat{k}\cdot\boldsymbol{\epsilon}'^{\dagger})(\hat{k}\times\boldsymbol{\epsilon})-(\hat{k}'\times\boldsymbol{\epsilon}'\dagger)\times(\hat{k}\times\boldsymbol{\epsilon}), && (3.66)
\end{aligned}$$

As for the case of resonant scattering (eq. 3.56), the bilinear dependence on the incident and scattered polarizations may be expressed in matrix form [deB81a, deB81b]:

$$\begin{aligned}
\mathbf{M}[\mathbf{A}] &= 2\sin^2(\theta)\begin{pmatrix} 0 & -(\hat{k}+\hat{k}') \\ \hat{k}+\hat{k}' & 2\hat{k}\times\hat{k} \end{pmatrix}, && (3.67)\\
\mathbf{M}[\mathbf{B}] &= \begin{pmatrix} \hat{k}\times\hat{k}' & -\hat{k}'(1-\hat{k}\cdot\hat{k}') \\ \hat{k}(1-\hat{k}\cdot\hat{k}') & \hat{k}\times\hat{k}' \end{pmatrix}, && (3.68)
\end{aligned}$$

and [Blu88]

$$\begin{aligned}
&M[\frac{1}{2}\mathbf{L}\cdot\mathbf{A}+\mathbf{S}\cdot\mathbf{B}] = \\
&= \begin{pmatrix} \mathbf{S}\cdot(\hat{k}\times\hat{k}') & -2\sin^2(\theta)\left((\tfrac{1}{2}\mathbf{L}+\mathbf{S})\cdot\hat{k}'+\tfrac{1}{2}\mathbf{L}\cdot\hat{k}\right) \\ 2\sin^2(\theta)\left((\tfrac{1}{2}\mathbf{L}+\mathbf{S})\cdot\hat{k}+\tfrac{1}{2}\mathbf{L}\cdot\hat{k}'\right) & (\tfrac{1}{2}\mathbf{L}+\mathbf{S})\cdot(\hat{k}\times\hat{k}') \end{pmatrix} && (3.69)\\
&= \begin{pmatrix} \sin(2\theta)S_2 & \substack{-2\sin^2(\theta)\cdot \\ (\cos(\theta)(L_1+S_1)-\sin(\theta)S_3)} \\ \substack{2\sin^2(\theta)\cdot \\ (\cos(\theta)(L_1+S_1)+\sin(\theta)S_3)} & \sin(2\theta)(2\sin^2(\theta)L_2+S_2) \end{pmatrix}. && (3.70)
\end{aligned}$$

Since the angular dependencies for spin and orbital momentum are different, it is possible to experimentally determine their ratio, L/S, and, for example, draw conclusions about the ionization state of the magnetic species.

The signal to noise ratio for non-resonant magnetic x-ray scattering can be estimated by comparing the magnetic and charge scattering amplitudes, e.g. for the $\sigma \rightarrow \sigma$ channel. For simplicity we assume only one atom per unit cell.

$$\frac{F_{\mathrm{mag}}}{F_{\mathrm{charge}}} = -i\frac{\hbar\omega}{mc^2}\sin(2\theta)\frac{S_2(\mathbf{Q})}{\rho(\mathbf{Q})} \tag{3.71}$$

$$\approx -i\frac{\hbar Q}{mc}\cos(\theta)\cdot\frac{S_2}{Z}\cdot\frac{f_S(Q)}{f(Q)}\cdot\frac{f_{\mathrm{mag}}(h,k,l)}{f(h,k,l)}, \tag{3.72}$$

where we have used $\sin(2\theta) = \frac{Qc}{\omega}\cos(\theta)$. $\rho(\mathbf{Q})$ is the Fourier transform of the charge density in the unit cell, Z is the number of electrons per unit cell, $f(Q)$ is the charge form factor, and $f(h,k,l)$ ($f_{\mathrm{mag}}(h,k,l)$) is the (magnetic) structure factor for a Bragg reflection. We see that the signal to noise ratio of a given Bragg reflection, (h,k,l), is increased at higher photon energies, due to the factor $\cos(\theta)$, since the Bragg angle, θ, decreases with increasing photon energy. This enhancement is most notable for reflections with large scattering vectors, $\mathbf{Q}$, and large Bragg angles for low energy x-rays.

4 PRACTICAL CONSIDERATIONS ON MAGNETIC X-RAY SCATTERING

Description of the synchrotron beamline

The synchrotron experiments were carried out at the bending magnet beamline X22C of the National Synchrotron Light Source. A Ni-coated toroidal focusing mirror upstream of the monochromator was used to eliminate higher harmonics in the incident beam. While this greatly improved the signal to noise ratio, especially for strong, allowed Bragg peaks where several layers of aluminum foil had to be used to attenuate the beam, it caused problems when photon energies above the Ni-K edge (8.333 keV) were required, due to strong absorption in the mirror itself. The beam was then passed through a Ge$(1,1,1)$ double crystal monochromator. The orientation of the second monochromator crystal could be fine-adjusted with computer controlled piezo actuators. No active feedback was used, instead the automated adjustment procedure had to repeated approximately once per hour[1]. A set of computer controlled horizontal and vertical slits, called "upstream slits", after the monochromator was used as scatter shield and, if a beam spot smaller than achieved by the focusing mirror was desired, to define the beam size. In order to monitor the incident x-ray intensity, a NaI counter detected radiation that was scattered of a thin Kapton foil positioned after these slits. An additional set of manually adjustable slits just upstream of the sample position was used to

---

[1] It is advisable to run the adjustment macro several times consecutively after the synchrotron beam was dumped, until the temperature of the first monochromator crystal has reached equilibrium.

further reduce the background radiation.

The samples were mounted on the cold finger of a Heliplex closed cycle refrigerator (base temperature 3.5 K) and oriented so that the $(h0l)$-zone was coincident with the vertical scattering plane of the diffractometer. Typically, two samples were mounted approximately 4mm apart. This separation was larger that the size of the beam at the sample position (≈ 1.5mm). This arrangement allowed us to switch samples by a simple translation of the cryostat along its axis, without the need to warm up the cryostat, change samples and then cool down again[2].

For studies with high **Q**-resolution, an asymmetrically cut Ge $(1,1,1)$ analyzer was used. The crystal was misscut by approximately 7° and aligned in the magnifying geometry to improve the acceptance angle. A set of computer controlled slits, called "detector slits", was used as scatter shield and to define the beam size. A NaI detector was then used as photon counting device.

Measurement of integrated intensities

For any experimental verification of the theoretical scattering cross section, it is necessary to measure the reflectivity of the sample at different (magnetic) Bragg reflections. It is difficult to perform absolute reflectivity measurements, because one would have to determine the *x-ray flux incident* on the sample, as well as the *absolute value of the absorption coefficient*, μ. It is usually possible to estimate the variation of the incident flux with changes of the sample orientation (geometric cross section correction). In the case of strong absorption — which is generally the case for resonant x-ray scattering — the absorption coefficient enters the reflectivity calculations only as a common prefactor. It is therefore much easier to perform *relative* reflectivity measurements, and to allow for a constant amplitude factor when comparing the experimental data to theoretical

---

[2] The typical turnaround time for this warming and cooling cycle was approximately 12 hours.

models.

The measured reflectivity depends on a multitude of experimental details, e.g. the divergence of the incident beam, the mosaic structure of the sample, and the instrumental resolution. Since it is virtually impossible the model all these dependencies, the common approach is to eliminate them experimentally by "integrating" the reflectivity over these variables — this procedure is called measuring the *integrated intensity* of a Bragg reflection.

In a reciprocal space picture, the reflectivity of the sample is a function of all three reciprocal space coordinates. The integrated intensity is the integral over all three of these coordinates. The hardware angles of a typical four-circle diffractometer with an Eulerian cradle may be interpreted as follows: The magnitude of the scattering vector is determined by the scattering angle, 2θ. A scan of the 2θ-circle is therefore, to first approximation, a longitudinal scan through reciprocal space. χ- and θ-scans, on the other hand, do not vary the scattering angle, therefore they are, to first order, transverse scans along orthogonal axes (since the θ- and χ-circles are perpendicular) through reciprocal space. We conclude that the integrated intensity can be measured by integrating over the three hardware parameters 2θ, χ and θ.

The experimental procedure for this type of measurement was to remove the analyzer crystal, and to open the detector slits until 2θ- and χ-scans showed flat tops, indicating the slits are not cutting the diffracted beam. For the first experiments of this type, a NaI detector was used [Det96]. However, since the incident photon energy is very close to an absorption edge of the sample, the background is dominated by fluorescence which, due to the coarse energy resolution of NaI detectors, cannot be filtered out. Therefore later experiments [Det97] employed an liquid N_2 cooled intrinsic Ge detector. Here, the energy resolution was high enough to allow discrimination between the elastically scattered signal and several fluorescence lines. In particular, it was possible to use several single channel analyzers[3] to simultaneously record the elastically scattered and the L_β fluorescence signal. Since for constant sample orientation the fluorescence yield is proportional to the incident x-ray flux on the sample, it could also be used as a normalization signal, e.g. during the measurements of order parameters. However, one has to remember that the absorption coefficients for elastically scattered radiation and the lower energy fluorescence are different so that, e.g. in an asymmetric geometry or for rough sample surfaces, the proportionality factor may vary with the sample orientation.

The integrated intensity of a Bragg reflection was then calculated by numerical integration over a *mosaic scan*, i.e. measurement of the reflected beam intensity as a function of the θ hardware angle of the diffractometer. Typically, a set of at least two θ-scans with different ranges and density of data points was combined to obtain a both good estimate of the background level off the Bragg condition and good resolution of the mosaic structure around the peak position. The mosaic structures of the measured reflections were then compared to verify that the reflectivity of the same grain had been measured.

Bragg scattering in asymmetric geometry

For many systems, only very small single crystals are available, so that it is not always possible to prepare a polished surface perpendicular to the magnetic modulation wave vector, **q**. However, it is usually possible to select a scattering plane that contains both the surface normal vector and the magnetic modulation wave vector.

The rare earth nickel borocarbides, for example, grow in the form of very thin platelets. Their flat face is perpendicular to the crystallographic (0, 0, 1) direction while the as-grown edges typically are parallel to the crystallographic (1, 0, 0) directions. For most of these systems the modulation wave vector of the magnetic structures

---

[3] No multi-channel analyzer was available during these experiments.

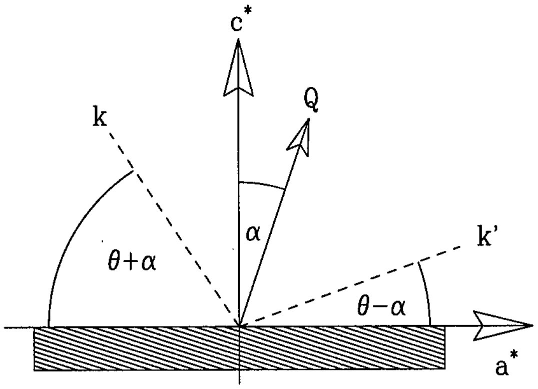

Figure 4.1 Scattering in the asymmetric geometry. The sample surface is perpendicular to the **c**-axis, while the scattering vector, **Q**, is in the **a**-**c** plane.

is **not** perpendicular to the flat face of the sample.

In these cases an asymmetric scattering geometry has to used to measure magnetic and charge reflections at a general position $(h,\ 0,\ l)$ in reciprocal space while scattering of a polished $(0,\ 0,\ 1)$ surface of a crystal, as illustrated in figure 4.1. Several complications arise in this geometry, namely:

- Not all positions in reciprocal space are accessible with this technique, since both the incoming and the scattered beam must form a positive angle with the crystal surface.

- An absorption correction has to be made due to the different lengths in the beam paths of the incoming and scattered beam within the sample.

- In all cases, the size of our samples was smaller than the beam size, so that a correction for the geometric cross section as a function of the scattering angle and the asymmetry angle has to be applied. This complication also arises in the symmetric scattering geometry. However, the asymmetry angle has to be taken into account.

Accessibility criterium for asymmetric reflections

As illustrated in figure 4.1, we consider an asymmetric reflection with $\mathbf{Q} = \mathbf{Q}_{||} + \mathbf{Q}_{\perp}$ with components parallel, $Q_{||}$, and perpendicular, $Q_{\perp}$, to the surface normal of a single crystal. Let α be the "asymmetry angle", i.e. the angle between the crystal surface normal and the scattering vector.

$$\sin\alpha = \frac{Q_{\perp}}{|\mathbf{Q}|} \tag{4.1}$$

The scattering angle, 2θ, is given by Bragg's law,

$$\frac{4\pi}{\lambda}\sin\theta = |\mathbf{Q}|\,, \tag{4.2}$$

where λ is the wavelength of the scattered radiation.

Both the incoming and the scattered beam have to from a positive angle with the crystal surface, so that $\theta + \alpha > 0$ and $\theta - \alpha > 0$. Since both angles have to be between 0° and 90°, these conditions may be written as $\cos(\theta) < \cos(\alpha)$, so that the accessibility criterium may be phrased as:

$$\left|Q_{||}\right| > \sqrt{\left(\frac{4\pi}{\lambda} - |Q_{\perp}|\right)|Q_{\perp}|}. \tag{4.3}$$

Reflections within a circle of radius $\frac{2\pi}{\lambda}$ around the point $(\frac{2\pi}{\lambda}, 0)$ in the $\mathbf{Q}_{\perp}$-$\mathbf{Q}_{||}$ plane of reciprocal space cannot be observed in this geometry.

For our specific geometry, an asymmetric $(h,\ 0,\ l)$ reflection with the surface normal to the $(0,\ 0,\ 1)$ axis, we find $\mathbf{Q}_{||} = l\mathbf{c}^{\star}$ and $\mathbf{Q}_{\perp} = h\mathbf{a}^{\star}$, so that only reflections are accessible that satisfy

$$|lc^{\star}| > \sqrt{\left(\frac{4\pi}{\lambda} - |ka^{\star}|\right)|ka^{\star}|} \tag{4.4}$$

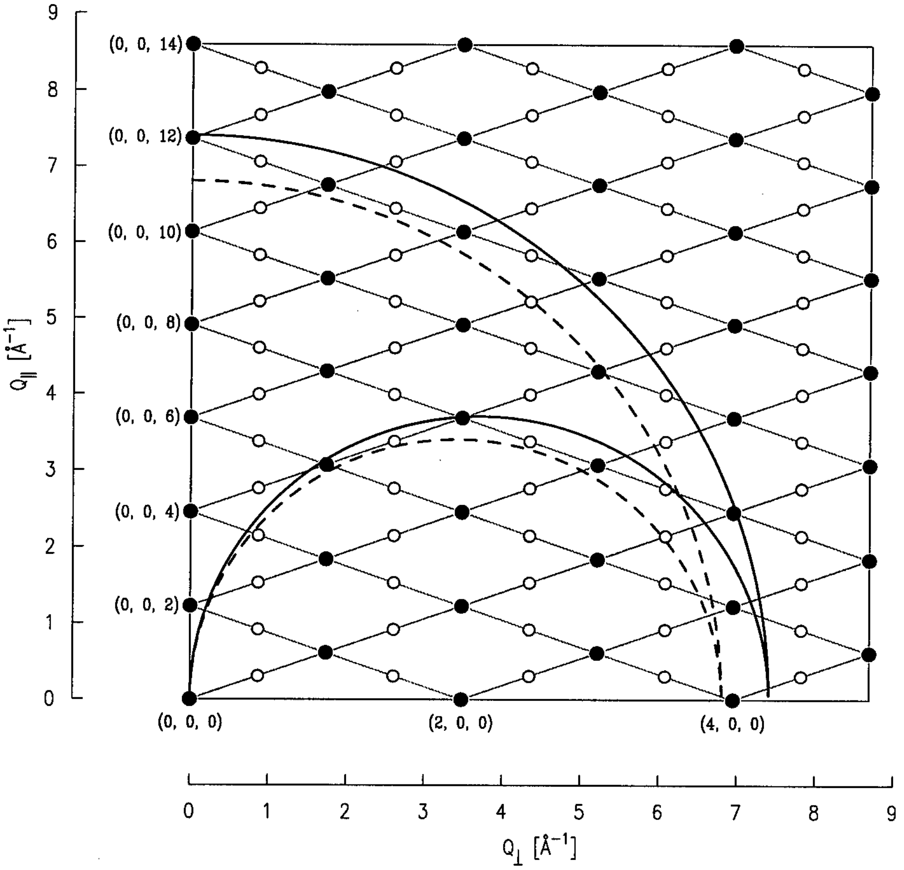

Figure 4.2 Charge (•) and magnetic (∘) reflections of SmNi$_2$B$_2$C in the **a-c** plane of reciprocal space that are geometrically accessible by asymmetric scattering of a sample polished perpendicular to the *c*-axis. Observable reflections must lie within a circle of radius $\frac{4\pi}{\lambda}$ around $(0,0)$, so that $2\theta \leq 180°$, and outside a circle of radius $\frac{2\pi}{\lambda}$ around $(\frac{2\pi}{\lambda},0)$ so that $\alpha < \theta$. The solid (dashed) lines indicate the limits for the Sm L$_2$ (L$_3$) resonant wavelengths.

Figure 4.2 displays the area in reciprocal space that is accessible by this technique for the case of $SmNi_2B_2C$ at the Sm $L_{2,3}$ resonant x-ray wavelengths.

Absorption in the asymmetric geometry

The absorption factor in the case of a symmetric reflection is treated in detail by Cullity [Cul78]. The generalization for the asymmetric case is straightforward.

We consider a large single crystal illuminated by an incoming beam of cross section A and intensity I_0. The intensity of a beam scattered by a volume element at a depth z is proportional to the number of illuminated scatterers, $\frac{An}{\sin(\theta+\alpha)}\mathrm{d}z$, where n is the density of scatterers. At a depth z, the incoming beam is attenuated by a factor of $e^{-\mu z/\sin(\theta+\alpha)}$, while the outgoing beam is attenuated by $e^{-\mu z/\sin(\theta-\alpha)}$. The total scattered intensity is obtained by integration of the product of these factors over all depths:

$$
\begin{aligned}
I(\theta,\alpha) &\propto \int_0^\infty \mathrm{d}z \frac{An}{\sin(\theta+\alpha)} e^{-\frac{\mu z}{\sin(\theta-\alpha)}} e^{-\frac{\mu z}{\sin(\theta+\alpha)}} && (4.5)\\
&\propto \frac{An}{2\mu}\frac{\sin(\theta-\alpha)}{\sin(\theta)\cos(\alpha)}. && (4.6)
\end{aligned}
$$

For a symmetric reflection, $\alpha = 0$, this obviously reduces to Cullity's [Cul78] result, $I(\theta, \alpha = 0) \propto \frac{An}{2\mu}$.

Surface sensitivity

Equation (4.6) may be interpreted as

$$
\begin{aligned}
I(\theta,\alpha) &\propto \text{(density of scatterers)} \times \text{(scattering volume)} && (4.7)\\
&\propto \text{(density of scatterers)} \times \text{(surface area)} \times \text{(penetration depth)}, && (4.8)
\end{aligned}
$$

where the penetration depth is given by $\frac{1}{2\mu} \cdot \frac{\sin(\theta+\alpha)\sin(\theta-\alpha)}{\sin(\theta)\cos(\alpha)}$. It is particularly small for grazing incident beam ($\theta + \alpha \approx 0$) and grazing scattered beam ($\theta - \alpha \approx 0$) geometries, so that these measurements are very sensitive to surface variations of magnetic structure. In resonant scattering experiments, this effect is enhanced by the large absorption coefficient, μ, at the resonant photon energies slightly above absorption edges.

Geometric cross section correction

In the limit of a small flat sample illuminated by a large beam, the number of photons incident on the sample surface is proportional to the projection of the sample surface along the incident beam direction, and the whole sample surface is illuminated.

In the limit of a large flat illuminated by a small beam, as considered above, the "footprint" of the beam on the sample is proportional to $\frac{1}{\sin(\theta+\alpha)}$.

Lorentz factor

Finally, the Lorentz factor, $1/\sin(2\theta)$ has to be included, so that, after dropping the constant factor An, the final expression for the integrated intensity is given by:

$$I(\theta, \alpha) \propto \frac{1}{2\mu} \cdot \frac{\sin(\theta-\alpha)\sin(\theta+\alpha)}{\sin(\theta)\cos(\alpha)} \cdot \frac{1}{\sin(2\theta)}. \tag{4.9}$$

In the symmetric case, this reduces to [Det96]:

$$I(\theta, \alpha = 0) \propto \frac{1}{2\mu} \cdot \frac{\sin(\theta)}{\sin(2\theta)}. \tag{4.10}$$

For a charge reflection with a scalar interaction, $F(\mathbf{Q}) \propto \rho(\mathbf{r})$, the intensity does not depend on the sign of the asymmetry angle, i.e. the reflections (h, 0, l) and ($-h$, 0, l) will have the same intensities.

In the case of XRES, the interaction is not of a simple scalar form [Blu85, Han88, Luo93, Hil96b] and therefore depends on the relative orientation of the sample and the incoming and outgoing beams [Hil96b]. As mentioned above, in the electric dipole approximation with the incoming beam polarized perpendicular to the scattering plane (σ-polarization), the magnetic structure factor of the fundamental satellite may be written as $F(\mathbf{Q}) \propto -\hat{k}' \cdot \hat{z}$, where $\hat{k}'$ is a unit vector in the direction of the outgoing beam and $\hat{z}$ is a unit vector in the magnetic moment direction of the scattering atom.

5 EXPERIMENTAL PROCEDURES AND RESULTS

Sample preparation and characterization

Single crystals of the $R\mathrm{Ni_2B_2C}$ compounds were grown at Ames Laboratory using a high-temperature flux growth technique [Can94, Cho95b]. Boron enriched in the isotope $^{11}\mathrm{B}$ was used to reduce the neutron absorption cross section. Platelets extracted from the flux were examined with x-rays and were found to be single crystals of high quality with the **c**-axis perpendicular to their flat surface as well as facets perpendicular to the **a**- and **b**-axes. Magnetization measurements as a function of temperature and magnetic field were performed using a Quantum Design superconducting quantum interference device (SQUID) magnetometer on single crystals from the same batches as those used in the x-ray experiments. The details of these measurements have been reported elsewhere [Can94, Cho95a, Cho95b, Cho95c, Can95, Cho96a, Rat96, Can00c]. One flat face and one edge (perpendicular to one of the in-plane axes) of each sample – except for the Sm and Nd compounds, where the crystals were too thin to scatter of the edges – was mechanically polished to remove any residual flux from the surface and to obtain a flat surface for x-ray diffraction. After polishing, the crystals were annealed, typically at 900°C in a vacuum of 10^{-7} torr for 36 hours.

$HoNi_2B_2C$

In this section we focus on the magnetic phase behavior of one member of the RNi$_2$B$_2$C series, $HoNi_2B_2C$ (T_C = 8.5 K, $T_N \approx$ 6.1 K) [Rat96]. This compound is particularly interesting because it exhibits a large reduction, or extinction, of the superconducting order parameter [Eis94, Can94, Rat96] in the incommensurate antiferromagnetic phase. The low-temperature commensurate spin structure is well understood and consists of moments aligned ferromagnetically within the **a**-**c** planes. These ferromagnetic sheets are stacked in alternating direction along the **c**-axis [Gol94, Gri94]. The ordered moment, as determined by powder neutron diffraction, is 8.7 μ_B [Gri94] while the macroscopic magnetization data indicate a moment of $\approx 9.9\mu_B$ [Can97a]. In terms of the competition with the superconductivity, the incommensurate phase is more interesting, though determining the spin structure has proven problematic [Gol94, Gri94]. Here, we present a detailed study of the incommensurate modulations. Our data allow a simplification of the phenomenology of these structures and we discuss the implications for the competition with the superconducting phase.

We have chosen to investigate the antiferromagnetic order using the technique of x-ray magnetic scattering, complemented by high-resolution magnetic neutron diffraction. This approach has a number of advantages. First, the reciprocal space resolution achievable with x-rays is an order of magnitude better than commonly obtained with neutron diffraction, greatly facilitating the investigation of large length scale magnetic phenomena. The polarization dependences of the x-ray and neutron scattering cross sections are different and therefore the techniques provide a useful complement to one another in determining spin structures. Resonant x-ray magnetic scattering is element specific and therefore can separate (in this case) the Ho ordered moment from that of the Ni. Each of these advantages plays a role in this study, revealing an incommensurate antiferromagnetic state that is considerably more complex than was previously realized.

On cooling through the transition at $T_C = 8.5$ K the superconducting order parameter is seen to increase, as measured by the upper critical field (H_{C2}) [Eis94, Can94, Gol94, Rat96], until $T_N \approx 6.1$ K. when it decreases, coincident with the appearance of the IC satellites. In earlier studies, two ordering wave vectors were reported, $\mathbf{q}_c = 0.915\ \mathbf{c}^\star$ [Gol94, Gri94] and $\mathbf{q}_a = 0.585\ \mathbf{a}^\star$ [Gol94]. A third harmonic of the **c**-axis modulation indicates that it is not perfectly sinusoidal [Gol94]. At $T_{IC-C} = 5.2$ K, a first-order transition into the commensurate phase is observed.

The x-ray experiments were performed at beamline X22C of the National Synchrotron Light Source, as described above. The sample was wrapped in aluminum foil to eliminate local heating effects[1]. A sample from the same batch was used for the neutron work, and mounted similarly. The mosaic spread of this sample was resolution limited, as determined by neutron diffraction, that is less than 0.2° (FWHM). The neutron-scattering data reported here were taken on the H9 spectrometer at the High Flux Beam Reactor operating at an incident energy $E_i = 3.5$ meV. The collimation was set to 60-40-15-S-5-10, resulting in a longitudinal resolution of 0.008 Å (FWHM). A pyrolytic graphite $(0, 0, 2)$ monochromator and analyzer determined the initial and final energies, respectively. For both the x-ray and neutron work reciprocal-lattice vectors of the form $(h, 0, l)$ were accessible.

The central results of these experiments are summarized in Fig. 5.1, in which x-ray scattering scans taken along the $(0, 0, l)$ axis in the vicinity of the $(0, 0, 3)$ antiferromagnetic Bragg peak are shown. At low temperatures (top panel) a single, sharp peak is observed at the $(0, 0, 3)$ position, corresponding to a well ordered antiferromagnetic structure. Data analysis, outlined below, show a **c**-axis correlation length of ≈5300 Å. The bottom panel shows data taken in the IC phase at $T = 5.4$ K. The high resolution

---

[1] Without such precautions, beam heating was sufficient to drive the sample from the commensurate phase into the incommensurate phase, a temperature rise of ≈ 2 K. The aluminum foil improved the thermal contact between the copper sample holder and the sample surface where the x-ray beam locally heated the sample. X-ray absorption in the foil was negligible.

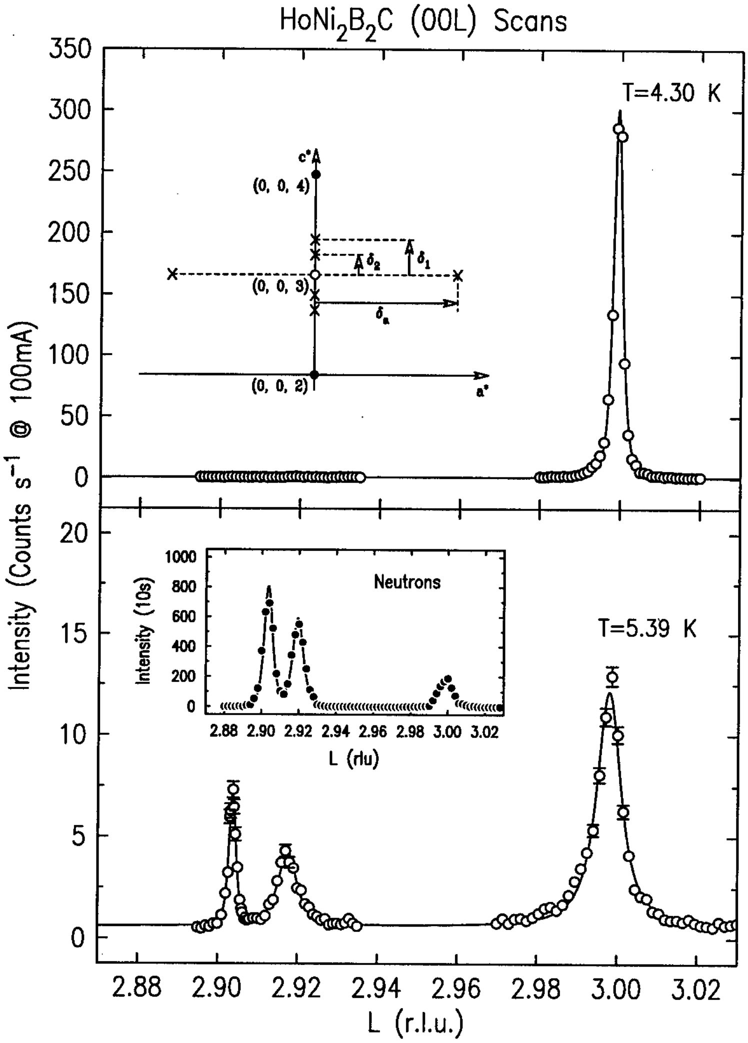

Figure 5.1 Longitudinal x-ray scans in the vicinity of the $(0, 0, 3)$ antiferromagnetic reciprocal-lattice point. These data were taken with the incident photon energy tuned to the Ho L_3 edge. (Top) $T = 4.3$ K. Only the commensurate peak is present. Inset. Schematic of reciprocal space. Closed (open) circles represent charge (antiferromagnetic) Bragg peaks. The crosses correspond to the incommensurate satellites present for temperatures above $T = 5.2$ K. Higher-order incommensurate peaks are not shown. (Bottom) Data taken at $T = 5.39$ K, in the incommensurate phase. The IC peak is comprised of two satellites at $(0, 0, 2 + q_1)$ and $(0, 0, 2 + q_2)$. The $(0, 0, 3)$ commensurate peak is still present but significantly reduced and broadened. Inset. High-resolution neutron-scattering data taken at an equivalent temperature confirming that the splitting of the IC satellite is a bulk effect.

of x-ray scattering reveals that the IC **c**-axis satellite around $\mathbf{Q} = 2.915\ \mathbf{c}^\star$ consists of two peaks, one at $\mathbf{q}_1 = 0.906\ \mathbf{c}^\star$ and the other at $\mathbf{q}_2 = 0.919\ \mathbf{c}^\star$. In addition, an **a**-axis satellite with $\mathbf{q}_a = 0.585\ \mathbf{a}^\star$ (not shown here) is also observed at these temperatures, in agreement with the neutron scattering results of ref. [Gol94]. A schematic of reciprocal space is shown in the inset of the top panel of Fig. 5.1. Here $\delta_1 = 1 - q_1$, etc. To discount the possibility that the splitting is in some way due to the sensitivity of x-rays to the near-surface region of the sample, high-resolution neutron diffraction was also performed. These data are shown in the inset to the bottom panel of Fig. 5.1. The incommensurate satellite is again seen to be split, confirming that this behavior is representative of the bulk. The difference in the relative intensities of the commensurate and incommensurate peaks in the neutron and x-ray data may be due to small discrepancies in the thermometry, or the differences in the angular dependences of the scattering cross sections. In the x-ray data, the satellite peak at $(2 + q_1, 0, 0)$ is extremely sharp, implying that this ordering extends over regions well in excess of 5000 Å in size. To extract estimates of correlation lengths, the $(2 + q_1, 0, 0)$ peak was taken to be resolution limited and fitted to a Lorentzian squared line shape. To analyze other **c**-axis data we then convolved this line shape with a Lorentzian signal function in a one-dimensional integral. In the IC phase, the $(0, 0, 3)$ peak and the $(2 + q_2, 0, 0)$ satellite are both broadened, indicating the presence of disorder in these structures.

The temperature dependence of the $(0, 0, 3)$ magnetic peak intensity is shown in Fig. 5.2(a). At low temperatures the intensity is approximately constant, suggestive of a saturated order parameter. At $T = 5.2$ K, the intensity abruptly falls, indicating a transition temperature of $T_{IC-C} = 5.2 \pm 0.2$ K, consistent with the transition temperatures observed in thermodynamic and transport measurements [Can94, Rat96]. This coincides with the appearance of incommensurate satellite peaks, and marks the first-order C-IC transition. The $(0, 0, 3)$ intensity decays more slowly as the temperature is increased

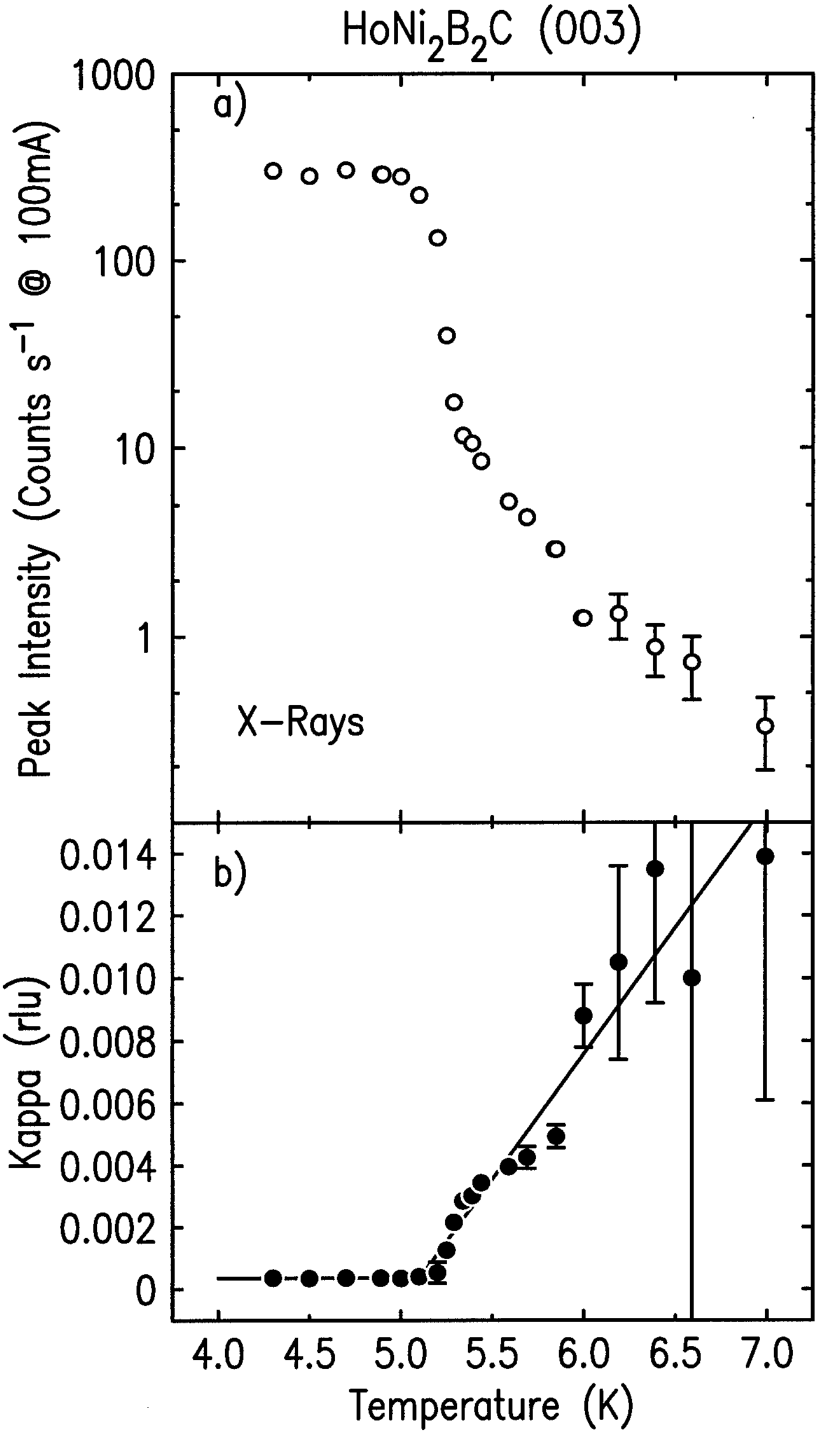

Figure 5.2 Temperature dependence of the $(0, 0, 3)$ commensurate antiferromagnetic Bragg peak. (a) The peak intensity. (b) The deconvolved width (see text), κ, of a Lorentzian line shape. The solid line is a guide to the eye.

further. The deconvolved width of the Lorentzian fit is plotted in Fig. 5.2(b). Below the transition it is almost resolution limited. Above T = 5.2 K the peak broadens, reaching a correlation length of $\xi_c = 500$ Å at T = 5.44 K. Our inelastic neutron-scattering data suggest that the broadening is not due to dynamic fluctuations, but to static or quasi-static disorder. Interestingly, the size of these commensurate regions is approximately the same as the incommensurate domains discussed below.

The peak intensities of the three incommensurate satellites are plotted in Fig. 5.3(a). No incommensurate scattering is observed below T = 5.2 K. Above this temperature the incommensurate satellites abruptly appear with relatively large intensities. As the temperature is raised, all three satellites exhibit similar behaviors, peaking at, or near, T = 5.3 K before decreasing slowly, so that, in the absence of any suitable model function, it is difficult to determine an ordering temperature from these data. Considering the variation of width and intensity, we estimate the Néel temperature to be $T_N \approx 6.1 \pm 0.4$ K. Above 5.5 K only one **c**-axis satellite, in addition to the **a**-axis satellite, can be resolved. Consequently a single Lorentzian signal function is used and these data are plotted as shaded symbols. We emphasize that these data were taken at the Ho L_3 edge and therefore the observation of both the **a**- and **c**-axis satellites is evidence that the Ho moments participate in both modulations.

The widths of the IC satellites are plotted in Fig. 5.3(b). The **c**-axis peak widths were obtained using the deconvolution procedure outlined above. However, the **a**-axis satellite width is dominated by sample mosaic and these data were not deconvolved. There is no observable change in this width, to within errors. The temperature dependence of the $\mathbf{q}_1$ and $\mathbf{q}_2$ satellite widths, κ_1 and κ_2, is intriguing. κ_1 remains resolution limited at all temperatures for which it may be resolved, indicative of an extremely well-ordered structure. Indeed there is some evidence that it is more highly ordered than the low-temperature commensurate structure (perhaps reflecting a coupling of the commensurate

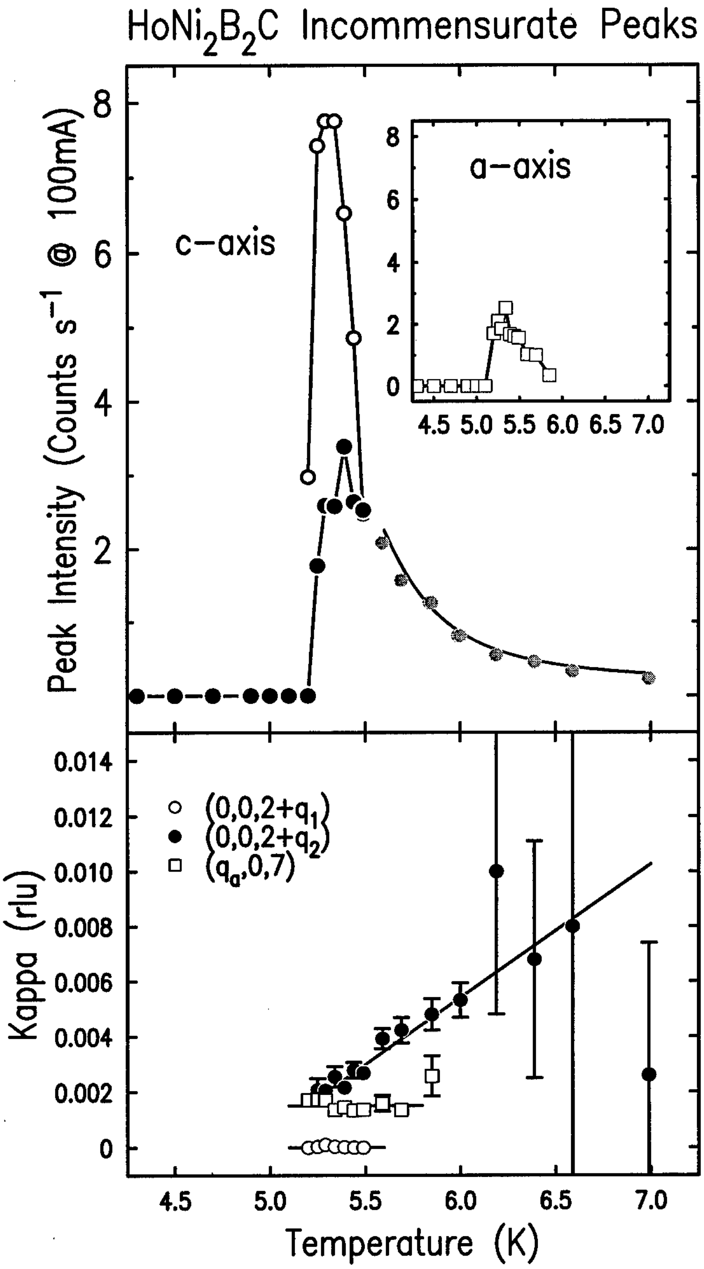

Figure 5.3 Temperature dependence of the incommensurate satellites. (Top) Peak intensities. The open (closed) circles represent the $\mathbf{q}_1$ ($\mathbf{q}_2$) satellites. The shaded circles represent data for which the two could not be resolved and were consequently fit to a single peak. The open squares represent the peak intensity of the **a**-axis satellite as measured at $(q_a, 0, 7)$. (Bottom) The widths, κ, of Lorentzian fits to the **c**-axis satellites. The **a**-axis satellite widths are the result of Lorentzian-squared fits.

order parameter in $HoNi_2B_2C$ to random strains in the sample, as has been observed for the spiral order parameter in pure Ho [Hel94]). The $\mathbf{q}_2$-modulation is disordered with a correlation length similar to the $(0, 0, 3)$ domains at similar temperatures, e.g. $\psi_c(\mathbf{q}_2) =$ 600 Å at T = 5.44 K.

In Fig. 5.4, the modulation wave vectors, $\mathbf{q}_1$, $\mathbf{q}_2$, and $\mathbf{q}_a$, are plotted as a function of temperature. The **c**-axis modulations were calculated with respect to the $(0, 0, 4)$ Bragg peak position, which remains fixed over this temperature range; the thermal expansion of the **c**-axis lattice constant is minimal and was ignored in this analysis. The **a**-axis modulation, $\mathbf{q}_a$, is plotted in units of $\mathbf{a}^\star$ and again thermal expansion is assumed negligible. We find all three modulations to be temperature dependent (Interestingly, in the temperature region in which both $\mathbf{q}_1$ and $\mathbf{q}_2$ are resolved, there is a linear relationship between the two; the change in $\mathbf{q}_2$ is five times that of $\mathbf{q}_1$, a result also seen in our high-resolution neutron data. The significance of this correlation is not clear.). At high temperature the **c**-axis modulation wave vector appears to lock-in to a value close to 0.09.

We now turn to a discussion of the spin structure in the incommensurate phase. This is seemingly complex, with four independent wave vectors to account for. However, our data allow some simplification.

First, the scattering that is the apparent remnant of the $(0, 0, 3)$ commensurate peak is in fact no longer commensurate with the average bulk lattice, but shifts to progressively smaller l as the temperature is raised (see Fig. 5.1). In addition, the peak becomes weaker and broader. Similar behavior was observed in the x-ray magnetic scattering near the first-order antiferromagnetic transition of UO_2 [Wat96a]. In this case, the effect of near-surface strains nucleating finite-sized ordered domains was considered to explain the shift and broadening observed above T_N, the so-called "two-length scale problem" [Alt95]. A similar explanation may apply here. A surface bias to the location of such strains

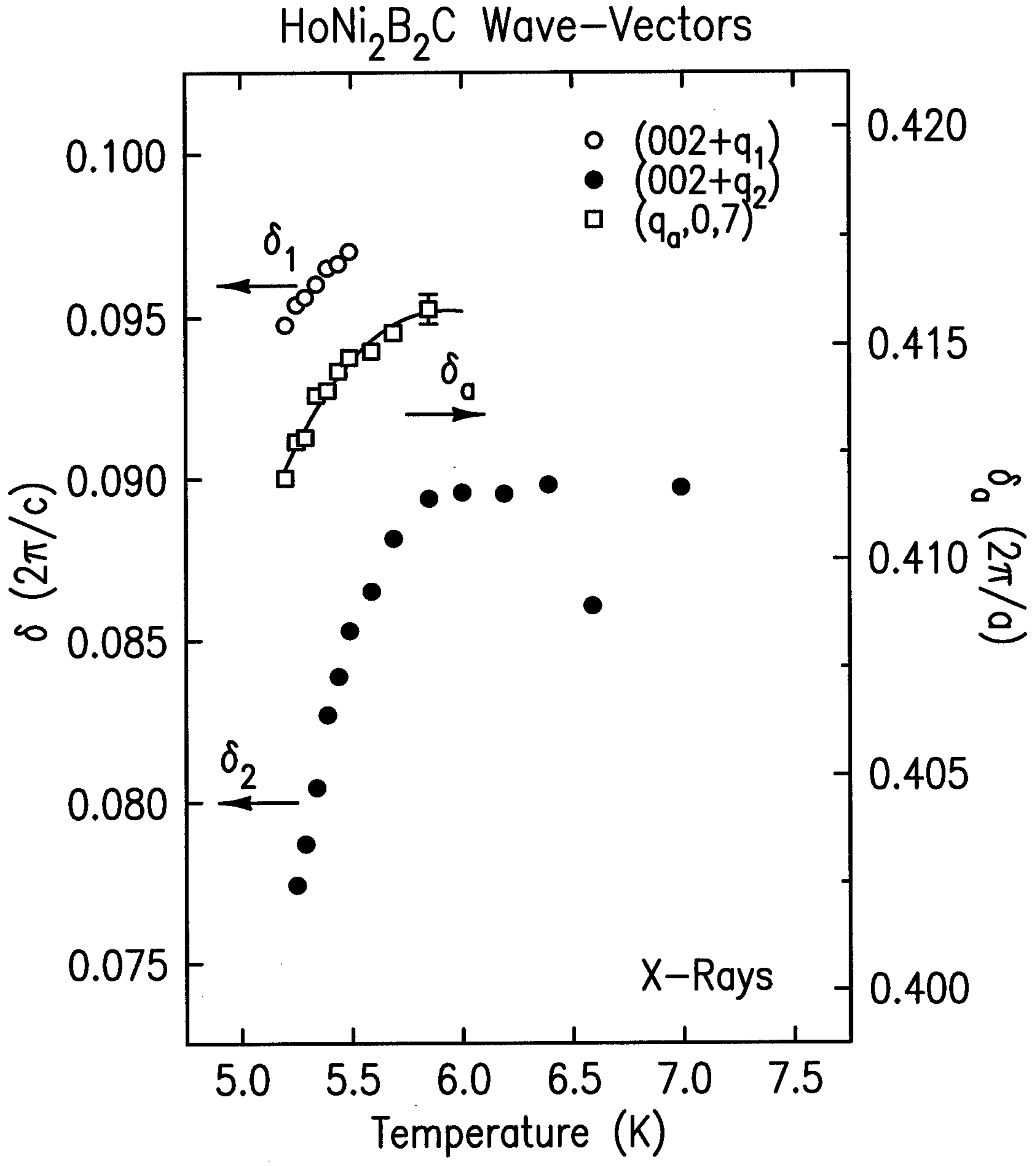

Figure 5.4 Temperature dependence of the incommensurate wave vectors. The **c**-axis satellite wave vectors, $\mathbf{q}_1$ and $\mathbf{q}_2$ (open and closed circles, respectively), are referred to the left-hand scale. The open squares represent the **a**-axis satellite position and have not been corrected for any expansion of the lattice. They are referred to the right-hand scale. Note the y-axis scale size is identical for the left- and right-hand axes.

would explain the relatively weak $(0, 0, 3)$ intensity in the neutron data. In this picture, the remnant commensurate scattering arises from domains of the low-temperature phase and does not coexist microscopically with th IC modulations, that is the IC domains do not simultaneously support the commensurate remnants.

The next question to address is whether the **c**- and **a**-axis modulations correspond to distinct domains, of if they form a double-**q** structure. An extensive search was carried out for third order satellites of the form $2\mathbf{q}_c + \mathbf{q}_a$ or $\mathbf{q}_c+2\mathbf{q}_a$, using neutron diffraction. These can only be present if the modulations arise from a single spin structure. No such peaks were observed, leading to an upper bound on their intensity of 2×10^{-4} of the fundamental. In contrast, the intensity of the $3\mathbf{q}_c$ peak is 3×10^{-2} of the fundamental. We also find that the phase behaviors of the two modulations are different in a **b**-axis applied field. Therefore we tentatively conclude that the **a**- and **c**-axis modulations correspond to separate domains.

One is now left with two distinct IC spin structures to describe. Taking the **a**-axis modulation first, we note that modulations of similar wave vector have been observed in the Er ($\mathbf{q}_a = 0.553\ \mathbf{a}^\star$ [Sin95, Zar95]), Tb ($\mathbf{q}_a = 0.555\ \mathbf{a}^\star$ [Lyn97, Der96]) and Gd ($\mathbf{q}_a = 0.55\ \mathbf{a}^\star$, [Det96]) members of the series. Both compounds form transversely polarized sinusoidal modulations. The similarity of the wave vectors in the four materials, together with band-structure calculations [Rhe95] which show a peak in the susceptibility new $\mathbf{q} = 0.6\ \mathbf{a}^\star$ in $LuNi_2B_2C$, due to a nesting of the Fermi surface, suggest a common origin to this modulation. In $HoNi_2B_2C$, the apparent coexistence of the **a**- and **c**-axis modulations implies that the two structures have closely similar free energies. In such a situation, regions of each phase may be stabilized by, e.g., strain, lattice defects, or impurities. Given the large correlation length observed in the x-ray experiments, these regions must be relatively large in agreement with previous single-crystal neutron scattering measurements. The influence of strain may help explain some of the discrepancies between the single crystal and powder neutron work [Gol94, Gri94].

The complementarity of the x-ray and neutron scattering data provide constraints on the structure of the **a**-axis modulation. The neutron cross section is sensitive to the components of the moment perpendicular to the momentum transfer, hence the presence of the $(q_a, 0, 0)$ satellite requires a transverse ordered moment. At the same time, the resonant cross section [Hil96b] requires an ordered moment in the **a**–**c**-plane to produce the observed $(1 - q_a, 0, 7)$ satellite. These observations, together with magnetization measurements which imply that the moments lie in the basal plane [Can94], suggest the existence of a longitudinal component (i.e. along $\mathbf{a}^*$) as well as the transverse component $(\| \mathbf{b}^*)$ seen in the Er and Gd compounds. Depending on the relative phase of the two components, the resulting structure is either an in-plane spiral, or a linear modulation with the moments at a fixed angle to the **b**-axis. More recent studies of the dependence of the magnetization upon the strength and direction of an external magnetic field indicate that the moments are locked into one of the 4 $[1, 1, 0]$ directions [Can97a], consistent with a linear modulation as mentioned above.

The **c**-axis structure consists of a well ordered incommensurate structure together with a disordered structure of slightly different wavelength. Both neutron (see also [Gol94, Gri94]) and x-ray polarization dependences are consistent with a basal plane spiral, with a temperature-dependent turn angle of $\approx 163°$ per layer. Even though these structures from at slightly higher temperatures, it is likely that the CEF fields still lock the magnetic moments into the $[1, 1, 0]$ directions, so that the modulation is either of a spin-slip type as observed in pure Ho[Gib88, Gib91], or a linear transverse wave. In the latter case, the presences of domains with moments orientations along different, but symmetry equivalent directions leads to polarization- and **Q** dependences very similar to spiral magnetic structures.

As mentioned in the introduction, the incommensurate phase coincides with a deep suppression of H_{C2}. Such a suppression, although not common, has been seen before near antiferromagnetic transitions of some $R\text{Mo}_6\text{S}_8$ compounds. [Fis90] and cannot be explained in terms of the multiple pair-breaking theory of Fulde and Maki [Ful66]. An additional pair-breaking mechanism has been postulated [Fis90] which appears to scale like the antiferromagnetic order parameter. Such a mechanism may be in effect here, perhaps associated with the incommensurate order parameter [Rat96, Gol94, Can94, Cho95b]. Alternatively, it is possible that the origin of the dip lies in the incommensurate modulations. Previously, IC structures have been associated with the competition between superconductivity and ferromagnetism. However, this is not the case in $R\text{Ni}_2\text{B}_2\text{C}$, as the presence of such modulations in non-superconducting members of the series demonstrates. If this state is responsible for the reduction in H_{C2}, then it may be connected with the Fermi-surface nesting mentioned above. Indeed, pair-breaking mechanisms based on nesting properties do exist [Ram81, Mac80]. A caveat to such speculations, however, is the richness of the temperature and magnetic field phase diagram [Rat96] which suggests that the energy balance between the numerous competing ground states is quite delicate. Subtle details in the Fermi surface, or even lattice defects, may then be important and may result in changes in the electronic structure. This would preclude qualitative arguments and detailed calculations specific to $\text{HoNi}_2\text{B}_2\text{C}$ may be required.

The Néel temperature, $T_N = 6.1 \pm 0.4$ K, and the IC-C transition temperature, $T_{IC-C} = 5.2 \pm 0.2$ K agree well with the transition temperatures observed in thermodynamic measurements [Can94, Rat96] and single crystal neutron scattering experiments [Gol94], although there is considerable uncertainty in the Néel temperature determined from the present single crystal diffraction experiments. Powder neutron diffraction experiments, on the other hand, observed the onset of antiferromagnetic order at a higher temperature, $T_N \approx 8$ K [Gri94]. In powder samples, however, the transition temperatures may be influenced by strain and surface defects. The thermodynamic data indicates another transition at T = 5.5 K [Can94, Rat96]. This temperature is close to where the two **c**-axis satellites become indistinguishable, but neither the x-ray nor the neutron data indicate a phase transition at this temperature.

In summary, we have performed high-resolution x-ray and neutron-scattering studies of the antiferromagnetism of $HoNi_2B_2C$. We find that the incommensurate state consists of a number of coexisting phases. They include an in-plane modulation with propagation vector along the **a**-axis, which shares some common features with the low-temperature structures of $ErNi_2B_2C$ and $GdNi_2B_2C$; a **c**-axis basal plane spiral-like structure, which is highly ordered; and some residual short-range ordered, static, commensurate regions, perhaps resulting from strain. The close interplay between the C and IC antiferromagnetic states and the superconductivity remain to be understood, even qualitatively, and should provide an interesting test case for theories of antiferromagnetic superconductors.

$GdNi_2B_2C$

Here, we report the results of x-ray resonant exchange scattering (XRES) [Gib88, Han88] and non-resonant [deB81b, Blu85, Blu88] x-ray magnetic diffraction measurements on $GdNi_2B_2C$. While this compound is not superconducting above T = 2 K, it presents interesting behavior below its magnetic ordering temperature [Can95]. Specifically, magnetization measurements on powder samples exhibit a single phase transition at about 20 K to a magnetic state, while the measurements on oriented single crystals show two distinct transitions, the first at $T_N \approx 20$ K and the second at $T_R \approx 14$ K, as shown in Fig. 5.5. The polycrystalline average, $\chi_{\text{poly}} = \frac{1}{3}\chi_{H\|c} + \frac{2}{3}\chi_{H\perp c}$, of the single crystal data is in good agreement with the powder measurements, suggesting that the transition at about 14 K arises from a spin-reorientation that preserves the sublattice magnetization [Can95]. Based on the data shown in Fig. 5.5, it was hypothesized that between 14 K and 20 K the Gd moments are aligned in the basal plane. An overall

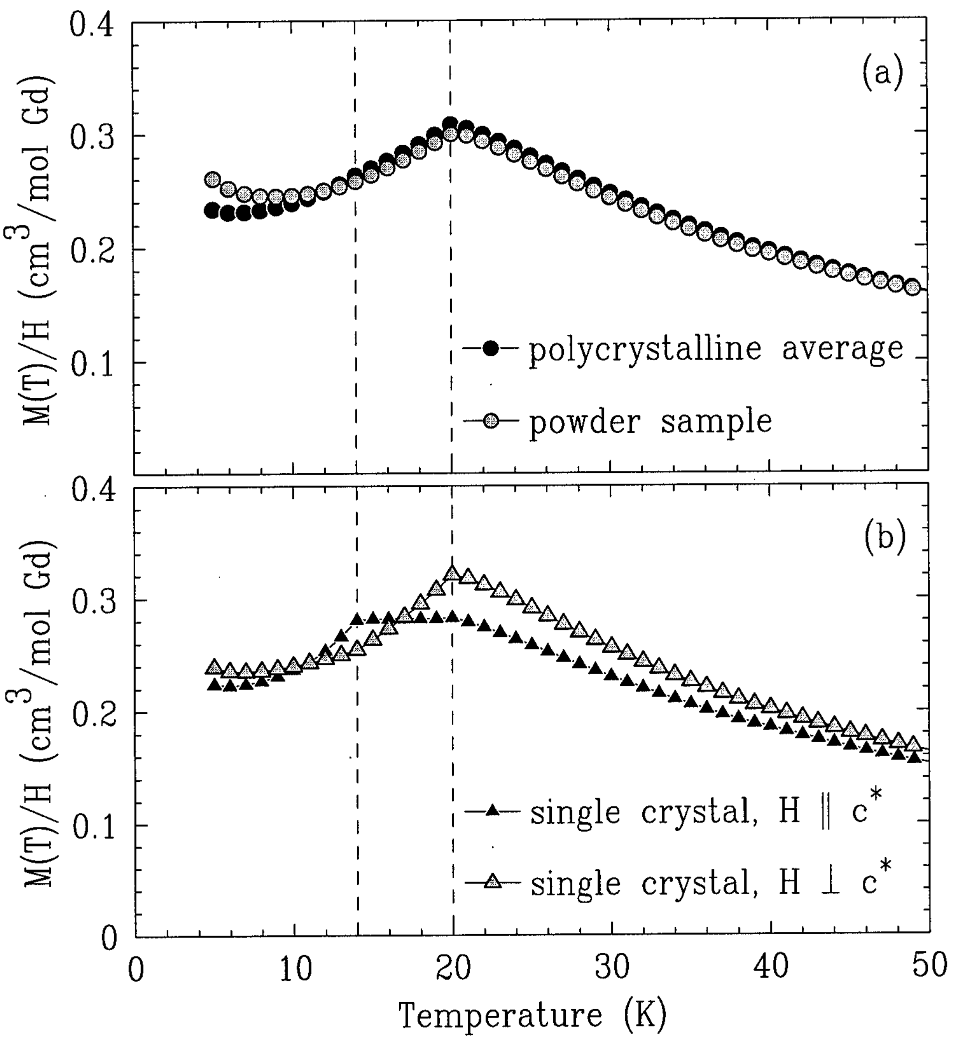

Figure 5.5 (a) The magnetization data taken on powdered single crystal samples are in good agreement with the polycrystalline average over the two single crystal measurements with H ∥ **c** and H ⊥ **c**, respectively. The antiferromagnetic ordering at the Néel temperature $T_N \approx 20$ K is clearly visible. (b) The single crystal magnetization data reveals a second phase transition at $T_R \approx 14$ K. The constant susceptibility for H ∥ **c** between the two transitions suggests that, in this temperature range, the magnetic moments are perpendicular to the **c**-axis. The dashed lines indicate the two transition temperatures.

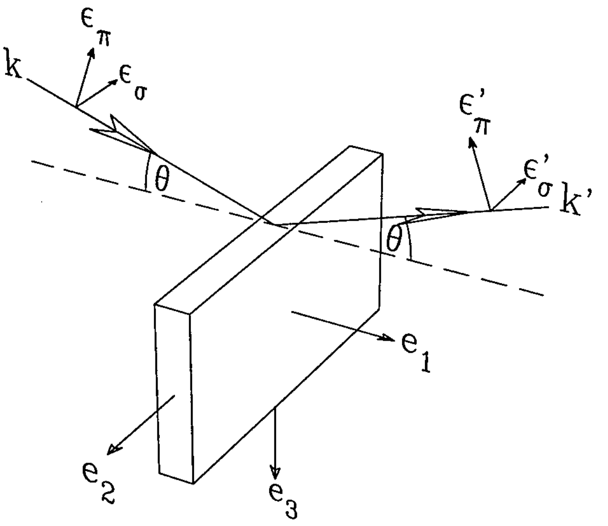

Figure 5.6 The scattering geometry used in the present measurements with respect to the **a**-, **b**- and **c**-axes of the sample, using the convention of Blume and Gibbs [Blu88]. The incident x-ray polarization is directed out of the scattering plane (σ polarization), along the **b**-axis.

decrease of the magnetic ordering temperatures was observed when Co was substituted for Ni [Bud95].

Our experiments show that below $T_N = 19.4$ K, $GdNi_2B_2C$ undergoes a transition to an incommensurate magnetic state characterized by a wave vector $\mathbf{q}_a = 0.55\ \mathbf{a}^\star$ ($\mathbf{b}^\star$), similar to the in-plane incommensurate ordering found in the Ho- and Er-based compounds [Gol94, Gri94, Sin95, Zar95]. Between 19.4 K and 13.6 K, the direction of the ordered magnetic moment is along the **b**- (**a**-) axis. As the temperature is lowered, the magnetic wave vector decreases continuously from 0.551 reciprocal lattice units (rlu) to 0.550 rlu until, at approximately 13.6 K, it starts to increase. At 3.5 K, the lowest temperature reached in this experiment, the wave vector of the modulation was determined to be 0.553 rlu. This rather dramatic reversal in direction of the temperature dependence of the wave vector is coincident with the appearance of a component of the ordered moment along the **c**-axis.

The resonant scattering technique [Gib88, Han88] utilizes atomic absorption edges to obtain large enhancements in the magnetic scattering cross section. For the sample orientation shown in Fig. 5.6, and the incident x-ray beam linearly polarized perpendicular to the scattering plane, the XRES cross section for dipole transitions (i. e. $2p \leftrightarrow 5d$) may be related to the components of the magnetic moment in the scattering plane [Hil96b] by:

$$I \propto \frac{(M_a \sin\theta - M_c \cos\theta)^2 \cdot \sin\theta}{\sin 2\theta}, \tag{5.1}$$

where M_a and M_c represent the components of the magnetic moment along the **a**- and **c**-axes, respectively, and 2θ is the scattering angle. The Lorentz factor, $1/\sin 2\theta$, as well as an angular factor required to correct for the fraction of the incident beam intercepted by the edge of the sample, $\sin\theta$, are included to allow a comparison between the calculated cross section and the measured integrated intensity, I. Note that in the present geometry and in the absence of an in-plane (π) polarized component of the incident beam, the resonant scattering measurements are insensitive to the component of the ordered moment along the **b**-axis, perpendicular to the scattering plane.

For the scattering arrangement described above, the non-resonant intensity may be written as [deB81b, Blu85, Blu88]:

$$\begin{aligned}\frac{I}{|f_{\mathrm{mag}}(\mathbf{Q})|^2} &\propto \frac{\sin\theta}{\sin 2\theta} \cdot \Big(S_b^2 \sin^2 2\theta \\ &+4\sin^4\theta \cdot (S_a \sin\theta + (L_c + S_c)\cos\theta)^2\Big) \end{aligned} \tag{5.2}$$

$S_{a,b,c}$ and $L_{a,b,c}$ denote the components of the spin and orbital angular momentum along the corresponding axes, respectively. We assume here that the Ni moments, even if present, make a negligible contribution to the magnetic scattering [Sin95, Bud95]. Therefore, the non-resonant magnetic form factor, $f_{\mathrm{mag}}(\mathbf{Q})$, should be determined by

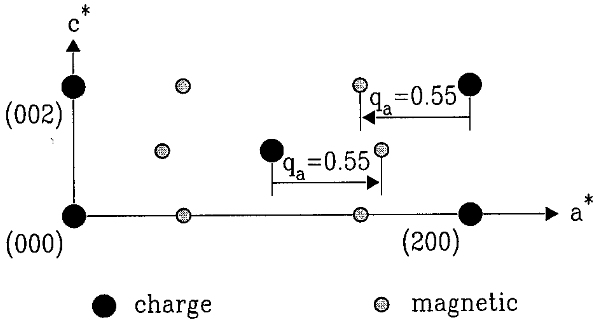

Figure 5.7 The $(h0l)$ reciprocal space plane showing the points associated with charge scattering (filled circles), and the points associated with the wave vector of the magnetic modulation $\mathbf{q}_a \approx 0.55\ \mathbf{a}^\star$ (shaded circles).

the $4f$-electrons of Gd, for which the orbital momentum $L_{a,b,c}$ can be neglected. For our analysis, we have used calculations of the Gd-$4f$ magnetic form factor based on a relativistic Dirac-Fock model [Fre72].

The important point here is that, in contrast to the XRES cross section, non-resonant scattering primarily probes the **b**-component of the moment at low-**Q** satellites (small 2θ) and all three components at high-**Q** satellites (large 2θ). Thus, with a judicious choice of satellites, all components of the moment may be studied with a single orientation of the crystal by combining resonant and non-resonant scattering data.

Above the Néel temperature, as determined from the magnetization measurements, only charge reflections (h, k, l) with $h+k+l = 2n$ were observed. As the temperature was lowered below 19.4 K, additional scattering developed as satellites of the charge peaks at $(h \pm q_a, k, l)$ (Fig. 5.7) with q_a ranging from 0.550 to 0.553 over the temperature range studied. The equivalence of the $\mathbf{a}^\star$- and $\mathbf{b}^\star$-directions in the tetragonal system also implies the existence of magnetic satellites at $(h, k \pm q_b, l)$ with $q_b = q_a$. However, the alignment of the crystal in the $(h0l)$-zone did not allow us to investigate these peaks. Careful scans along the in-plane and out-of-plane directions did not reveal any additional scattering below 19.4 K that is not associated with the satellite reflections mentioned

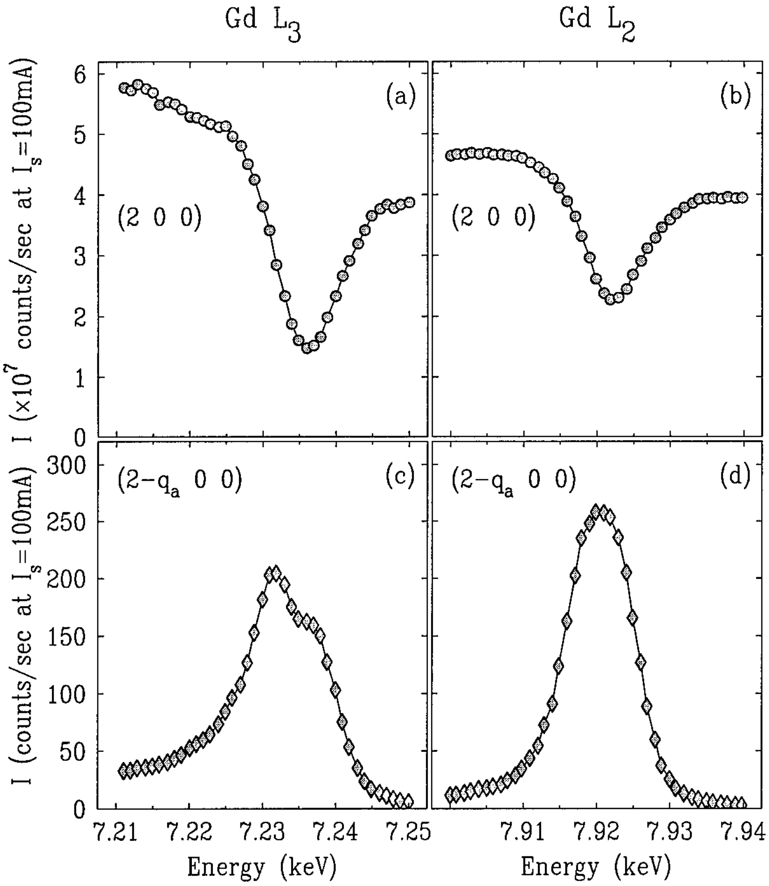

Figure 5.8 Energy scans of the $(2,0,0)$ charge (a,b) and the $(2-q_a,0,0)$ magnetic reflections (c,d) across the Gd L_3 and Gd L_2 absorption edges. In both cases, the maximum resonant enhancement lies slightly above the corresponding absorption edge observed in the charge reflections. This indicates the electric dipole character of the associated electronic transitions.

above.

Fig. 5.8 shows energy scans of the (2,0,0) charge reflection and the $(2-q_a,0,0)$ magnetic satellite across the Gd $L_{2,3}$ absorption edges at T = 4 K. In both cases, the maximum resonant enhancement is observed slightly above the corresponding absorption edge (defined by the maximum slope in the charge reflection data), indicating the electric dipole character of the electronic transitions involved. In the case of electric quadrupole transitions ($2p \leftrightarrow 4f$) the maximum resonant enhancement is generally observed several eV below the absorption edge [Gib88, Han88] due to the stronger coulomb interaction between the $4f$-electrons and the $2p$ core hole. No resonant enhancement was observed at the Gd L_1 edge. All the resonant data presented in this paper were taken at the Gd L_2 resonance where the maximum count rate in the magnetic reflection was achieved. For the "non-resonant" scans we chose an incident energy of 7.0 keV, which lies below all three Gd L-absorption edges, to minimize absorption and the fluorescence background. It is worth noting that although this energy is approximately 200 eV below the L_3 edge, there may still be resonant contributions to the scattering. We estimate that these interference effects are < 4 % of the signal, based upon simple numerical models [Gib88].

Figures 5.9, 5.10 and 5.11 summarize the results of our study of the temperature dependence of the magnetic scattering from $GdNi_2B_2C$. Figs. 5.9 and 5.10 show selected scans of the non-resonant and resonant scattering at the $(2 - q_a, 0, 0)$ satellite, respectively, while Fig. 5.11 summarizes the full data set by plotting the position, q_a, peak intensity, P, and longitudinal width, w, of the satellite as a function of temperature from fits to the data. Before describing the details of these data and the fits, we point out some of the essential features of the magnetic structure of $GdNi_2B_2C$ as determined by these measurements.

As shown in figs. 5.8, 5.10 and 5.11, the low temperature ($T \leq 13.6$ K) scans of the $(2 - q_a, 0, 0)$ peak taken at the Gd L_2 energy exhibit a strong resonant scattering contribution. Above approximately 13.6 K, however, the resonant enhancement of the magnetic scattering is essentially absent (see Fig. 5.11e) so that the intensity and line shape of the magnetic scattering observed at the Gd L_2 edge is comparable to the non-resonant data set taken at 7.0 keV. Energy scans showed only a slight resonant enhancement above 13.6 K which we attribute to a small π-polarized component in the incident x-ray beam [San94]. The non-resonant magnetic scattering persists up to 19.4 K, the Néel temperature determined from magnetization measurements.

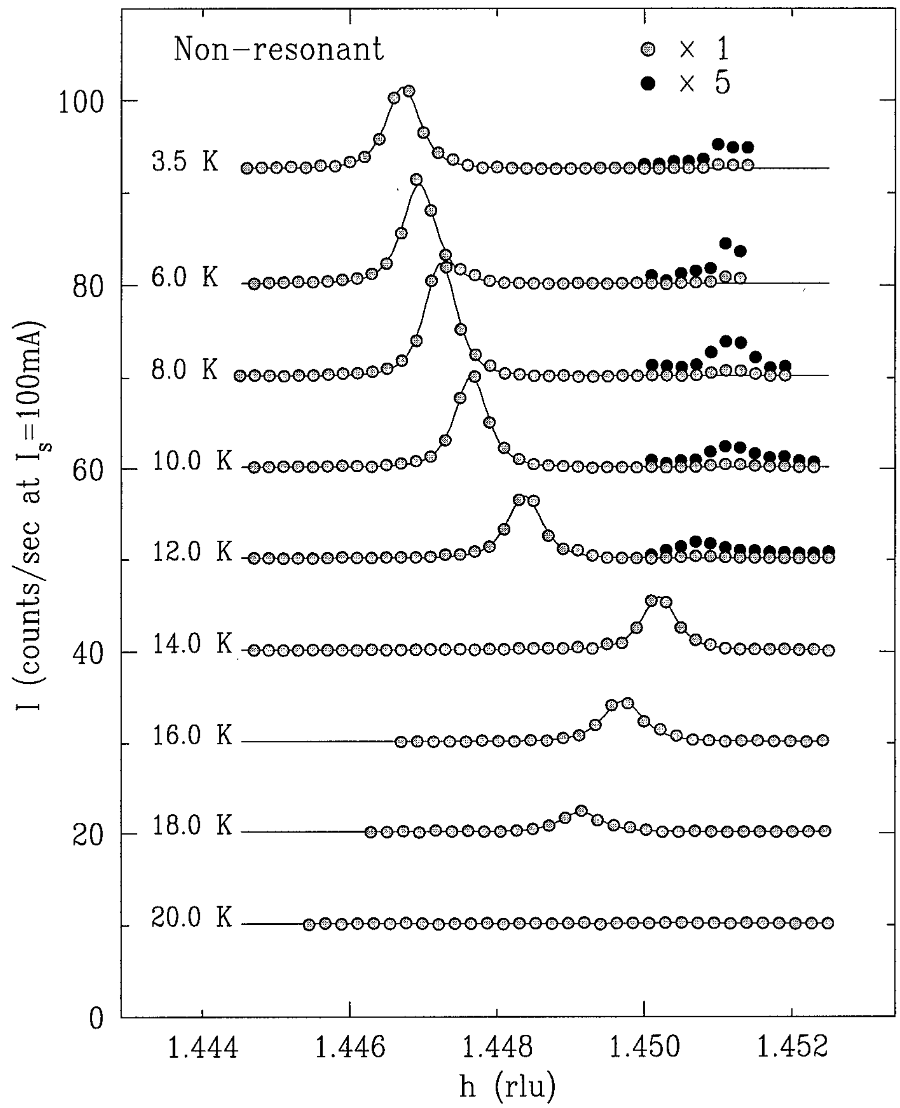

Figure 5.9 Selected scans of the measurements of non-resonant magnetic scattering at the $(2 - q_a, 0, 0)$ reflection taken at an energy of 7.0 keV. The lines represent the results of the fits described in the text. To increase the visibility of a second peak, part of the data has been multiplied by 5 (solid circles).

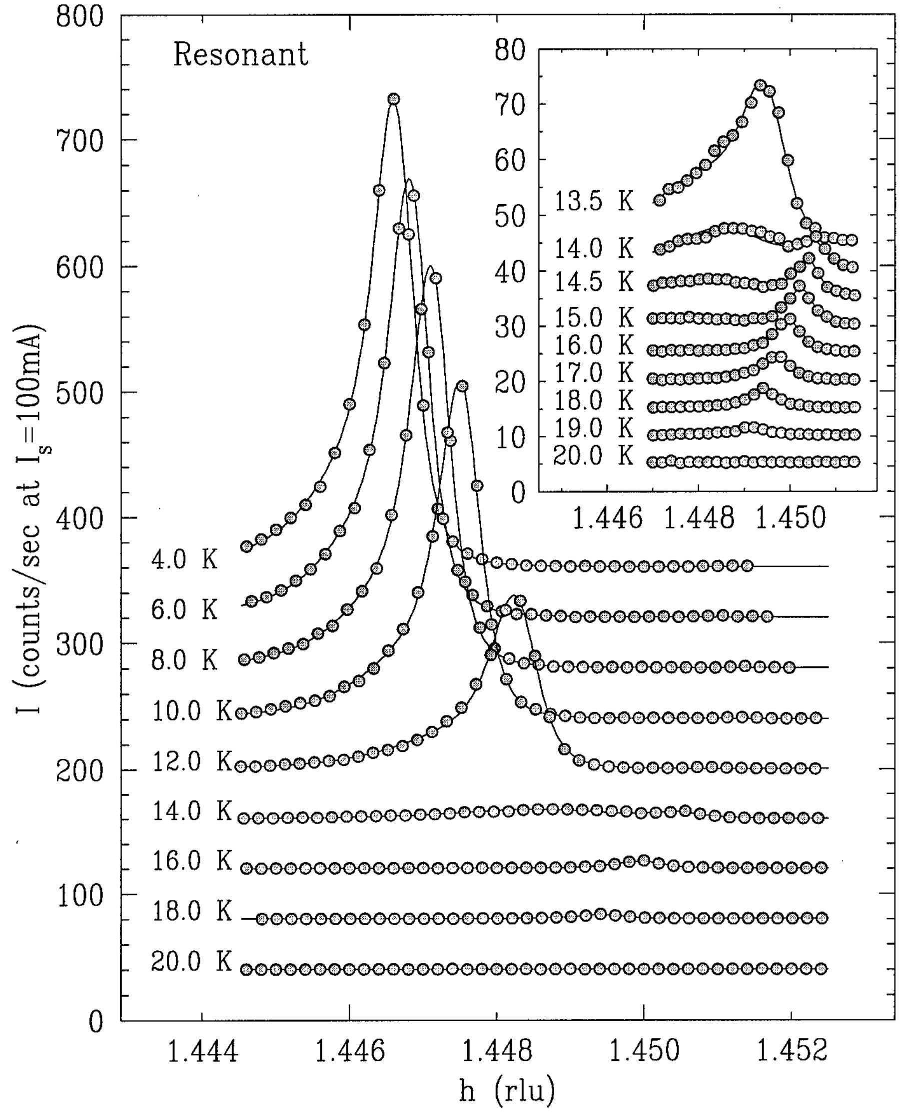

Figure 5.10 Selected scans of the measurements of the XRES at the $(2 - q_a, 0, 0)$ magnetic reflection taken at the Gd L_2 absorption edge. The inset shows some of the resonant scans on a expanded intensity scale. Note the presence of a broad and sharp component at 13.5 K, and the reversal in the motion of the magnetic satellite.

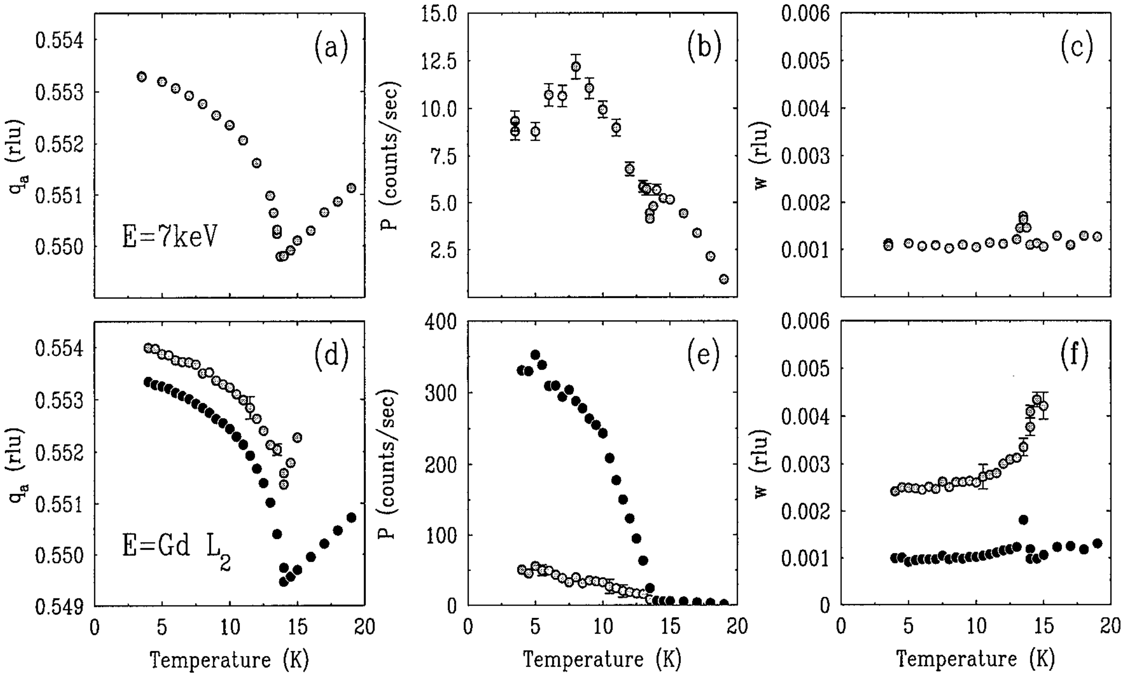

Figure 5.11 The results of fits to the complete data set obtained from the non-resonant (a,b,c) and resonant (d,e,f) measurements showing the evolution of position, intensity and width of these peaks. The transition temperatures observed in the resonant and non-resonant intensities are $T_R = 13.6 \pm 0.1$ K and $T_N = 19.4 \pm 0.3$ K, respectively.

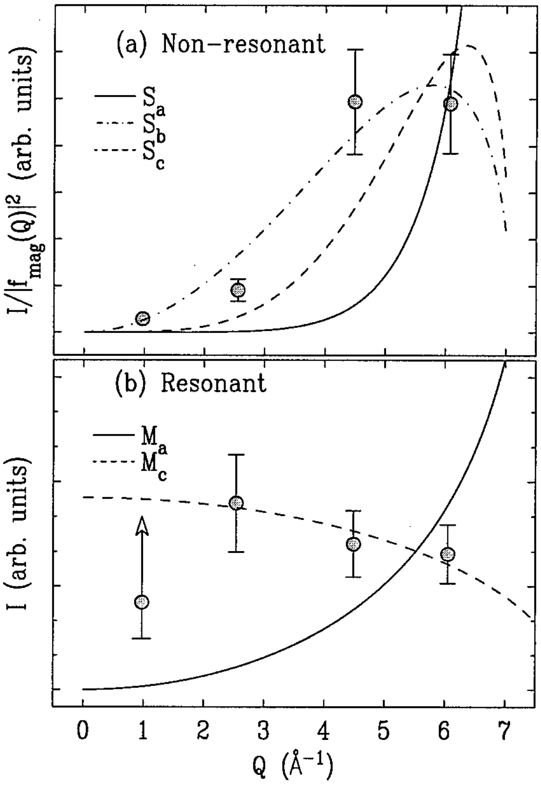

Figure 5.12 The **Q**-dependence of the integrated intensity of magnetic satellites along the $[h, 0, 0]$ direction at 3.6 K, obtained off-resonance (a) and on-resonance (b). The lines show the **Q**-dependence of the integrated intensity expected from eqs. 5.1 and 5.2 for ordered components of the Gd $5d$ magnetic moment M and the Gd $4f$ spin S along the **a**- (——), **b**- (- · · - -) and **c**-axis (– – –), respectively.

From eqs. 5.1 and 5.2, the absence of significant resonant scattering at the magnetic wave vector between 13.6 K and 19.4 K, and the presence of non-resonant scattering implies that, in this temperature region, the ordered moment is oriented in the basal plane and transverse to the modulation wave vector (e. g. **M** || **b** for the **a**-axis modulation), as was hypothesized based on the magnetization data [Can95] and as was found for $ErNi_2B_2C$ by neutron diffraction [Sin95, Zar95]. Below 13.6 K, however, the observation of resonant enhancement implies that an ordered component of the moment exists in the scattering (**a**,**c**)-plane.

In order to determine, more precisely, the direction of the moment below 13.6 K, we have carefully measured the integrated intensity of a series of satellites along the **a***-axis both on and off the resonance condition at the lowest temperature accessible (3.5 K). To ensure that we actually recorded the full integrated intensity, the analyzer crystal was removed and all slits downstream of the sample were opened until 2θ and χ scans displayed a plateau for all diffraction peaks that were studied. The integrated intensities, I, measured by rocking the crystal at a fixed scattering angle, are shown in Fig. 5.12. With the exception of the lowest angle satellite[2], the **Q**-dependence of the resonant scattering (Fig. 5.12b) is well described by a component of the ordered moment along the **c**-axis. The **Q**-dependence of the non-resonant scattering (Fig. 5.12a) is well described by a component of the moment along the **b**-axis.

From these measurements, we deduce that below 13.6 K the moment remains transverse to the propagation direction and acquires a component out of the basal plane. We cannot, however, determine the relative phase shift $\Delta\phi$ between the two components of the moment at low temperature from the present measurements. The magnetic structure may be described in one of two ways, as sketched in Fig. 5.13:

(a) If the components are out of phase ($\Delta\phi \neq 0$), a modified spiral-like structure results. Different magnitudes of the **b**- and **c**-components of the spin would lead to an elliptical projection onto the (**b**,**c**)-plane (see Fig. 5.13a). With the disappearance of the **c**-component at 13.6 K this structure is degenerate with the planar spin modulation described above. The low symmetry ($2mm$) of the [100]-direction is likely to induce fanning or bunching of the spiral which, in turn, would result in a rich spectrum of higher harmonic satellites.

---

[2] We point out that for both the resonant and non-resonant measurements the lowest **Q** satellite is subject to the greatest systematic uncertainty since the angle between the incident beam and the sample surface is only about seven degrees. If the surface of the sample was misscut with respect to the diffracting planes by a small amount (1–2°), or if the polished surface was rounded, the measured integrated intensity of this peak would strongly decrease. In Fig. 5.12, the error bars have been approximated by assuming a 2.5° misscut of the sample surface and 5% other systematic errors.

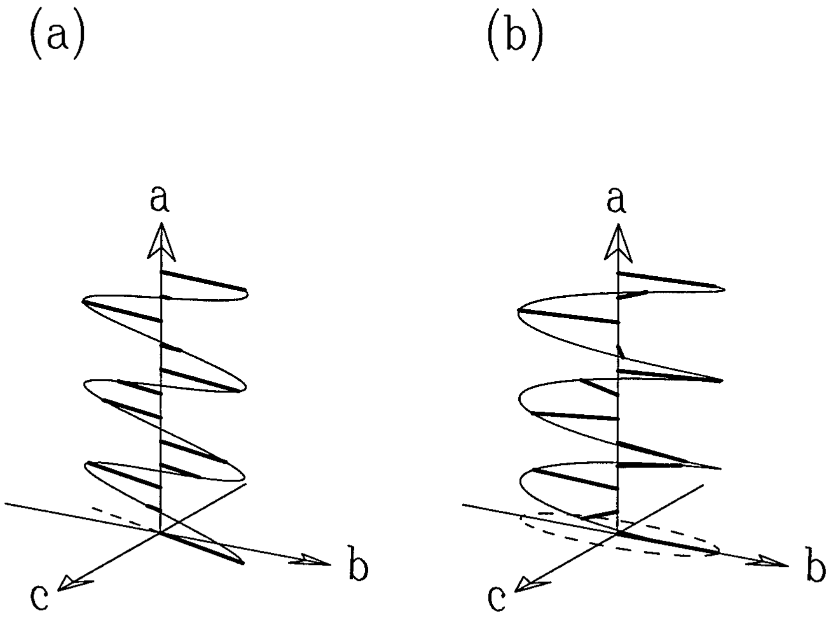

Figure 5.13 The two components of the ordered magnetic moment along the **b**- and **c**-axes feature the same modulation wave vector $\mathbf{q}_a \approx 0.55\ \mathbf{a}^\star$. However, our measurements did not yield any information on the relative phase shift $\Delta\phi$ between the two oscillations. Two possible structures with $\Delta\phi = 0$ (transverse wave, (a)) and $\Delta\phi = \pi$ (spiral-like, (b)) are displayed here.

(b) If the two components are in phase ($\Delta\phi = 0$), the structure is a transverse spin modulation as described above for 13.6 K < T < 19.4 K, but with the moment rotated away from the **b**-axis in the (**b**,**c**)-plane (for the modulation along the **a**-axis), as shown in Fig. 5.13b. In this case, the stronger decrease of the **c**-component of the moment with increasing temperature corresponds to a decrease in the angle between the moment and the **b**-axis until, at 13.6 K, the moments lock-in along the **b**-axis.

However, the determination of the relative phase $\Delta\phi$ will have to await further measurements of higher harmonic satellites by neutron or XRES experiments.

Having described the basic elements of the magnetic structures observed in $GdNi_2B_2C$ below T_N=19.4 K, we briefly discuss some other features found in the XRES and non-resonant scattering data of figs. 5.9, 5.10 and 5.11.

The non-resonant data are adequately fit using a Lorentzian-squared line shape. This line shape was chosen simply as an empirical description of the data. The resolution function was not deconvolved from the data. The results of these fits to the nonresonant scattering data are shown in Fig. 5.11, where we plot the position, q_a (5.11a), peak intensity, P (5.11b), and longitudinal width, w (5.11c), of the peak.

The fits had to be modified to achieve reasonable agreement with the XRES data. The appearance of two clearly distinguishable peaks between 14 K and 15 K (see inset in Fig. 5.10) motivated us to include two peaks in all fits below 15 K, where a single peak was not sufficient to approximate the data. Below 13.6 K, all scans show strongly asymmetric line shapes. The physical reasons for this asymmetry are not fully understood, especially since neither the non-resonant magnetic scattering nor the charge reflections exhibit significant asymmetry. Most likely it is due to strain in the near surface layers. We point out that the resonant scattering measurements are more sensitive to the near surface region as a result of the strong absorption effects at the L_2 edge. Nevertheless, reasonable fits to the resonant data were achieved by including asymmetry in both peaks.

To minimize the number of free parameters, the asymmetry and the background were fixed for all temperatures. The results of these fits are presented in Fig. 5.11 (d), (e) and (f). The filled circles indicate the position, q_{a1}, peak intensity, P_1 and longitudinal width, w_1, of the first peak, while the shaded circles indicate the corresponding parameters of the second peak. Above 15 K, the intensity of the second peak was constrained to be $P_2 = 0$.

Figs. 5.11(a) and (d) show the magnitude of the modulation wave vector, $\mathbf{q}_a$, measured at the $(2 - q_a, 0, 0)$ satellite, as a function of temperature. It decreases with decreasing temperature until, at approximately 13.6 K, this movement reverses direction. Below this temperature, a second reflection with lower, but finite intensity (solid circles in Fig. 5.9) indicates that a small fraction of the sample does not undergo the second transition at 13.6 K. Instead, the modulation wave vector of these domains continues to decrease with decreasing temperature. The reversal in the motion of the magnetic satellite is reminiscent of what is observed at the transition in pure Er from a **c**-axis modulated (CAM) structure (with the ordered moment along the **c**-axis) above 52 K to a cycloidal structure between 52 K and 18 K, upon the development of a component of the ordered moment in the basal plane [San94, Gib86, Cow92, Jen93].

Finally, we turn our attention to the transition at 13.6 K. In a narrow range around this temperature, the data taken at the Gd L_2 edge is best characterized by two peaks, one broad and the other sharp as shown in figs. 5.10 and 5.11. The presence of two peaks in the resonant scattering measurements is reminiscent of earlier measurements [Hil96a] of the XRES from $HoNi_2B_2C$. These experiments and theoretical arguments [Alt95] suggest that the origin of a second peak of lower intensity and broader width might be related to structural defects or strain in the "near surface" region of the sample.

In summary, resonant and non-resonant magnetic x-ray scattering techniques have been applied to determine the magnetic structure of $GdNi_2B_2C$. We find that below the Néel temperature, $T_N = 19.4$ K, the magnetic moments order in a transverse spin modulation with a wave vector $\mathbf{q}_a \approx 0.55\ \mathbf{a}^\star$ ($\mathbf{b}^\star$). A second phase transition occurs at about 13.6 K. Between 19.4 K and 13.6 K, the ordered magnetic moment lies in the basal plane of the tetragonal structure, along the **b**- (**a**-) axis. In this temperature range, the modulation wave vector decreases with decreasing temperature. Below 13.6 K, an additional component along the **c**-direction develops while the modulation wave vector increases with decreasing temperature. Our findings are in good agreement with the magnetization measurements on single crystals described in the introduction [Can95] and provide further information about the systematics of magnetic ordering in the $R\mathrm{Ni_2B_2C}$ family. In particular, there is evidence of the nesting vector close to 0.6 rlu in the non-magnetic Lu compound, in $\mathrm{GdNi_2B_2C}$, where CEF effects can be neglected, and in presence of both magnetism and CEF-effects (Ho, Er and Tb compounds). Therefore, it appears to be a general feature of this class of compounds, as predicted by theory [Rhe95].

$\mathbf{ErNi_2B_2C}$

In $\mathrm{ErNi_2B_2C}$, superconductivity is observed below $T_C = 10.5$ K[Cav94a, Eis94, Cho95b]. The onset of long range antiferromagnetic order below $T_N = 6.0$ K lowers the upper critical field, H_{C2}, especially if the field is applied perpendicular to the $(0, 0, 1)$-axis. Previous neutron diffraction experiments, carried out on powder[Sin95] and single crystal[Zar95] samples, show that $\mathrm{ErNi_2B_2C}$ orders in a transverse spin density wave with modulation wave vector $\mathbf{q}_a = (0.55, 0, 0)$ and with alignment of the magnetic moments parallel to the $(0, 1, 0)$-axis of the crystal. The tetragonal symmetry of the crystal also implies the existence of domains with modulation wave vector $\mathbf{q}_b = (0, 0.55, 0)$ and alignment of the moments along $(1, 0, 0)$. As the temperature is lowered, higher harmonic satellites were observed to develop[Sin95, Zar95], which shows that the spin density wave "squares up"; the modulation wave vector is approximately independent of temperature[Sin95, Zar95]. A similar magnetic structure was observed in the Gd compound[Det96], while $TbNi_2B_2C$ forms a longitudinal spin density wave with approximately the same wave vector[Der96].

More recently, small angle neutron scattering has been used to study the vortex structure of $ErNi_2B_2C$[Yar96, Esk97]. At high fields, these experiments observed a square flux-line lattice, while at low fields the flux lines order in the hexagonal lattice more typically found in type-II superconductors[Esk97, Kog97]. In addition, a significant coupling between the magnetic ordering and the flux lines was observed, as evidenced by rotation of the vortex lines away from the direction of the applied field below the Néel transition, coincident with disordering of the flux-line lattice[Yar96]. These data demonstrate how, in a magnetic superconductor, the vortex lattice structure may be coupled to the magnetic-order parameter.

In this paper, we report the results of x-ray diffraction measurements on $ErNi_2B_2C$ and demonstrate the existence of an interaction between the crystal structure and the magnetic-order parameter by means of conventional crystalline electric field (CEF) coupling.

Single crystals of $ErNi_2B_2C$ were grown at the Ames Laboratory using a high-temperature flux growth technique[Can94, Cho95b]. Platelets extracted from the flux were examined by x-ray diffraction and were found to be high quality single crystals with the $(0,0,1)$-axis perpendicular to their flat surface. Magnetization measurements were performed as a function of temperature and magnetic field, using a Quantum Design superconducting quantum interference device (SQUID) magnetometer on single crystals from a similar batch as those used in the x-ray experiments. The details of these measurements have been reported elsewhere[Cho95b, Can96]. The sample was cut perpendicular to the $(1,0,0)$ direction and the resulting face was mechanically polished to obtain a flat, oriented surface for x-ray diffraction. After polishing, the crystal was annealed at 900°C in a vacuum of 10^{-7} torr for 36 hours. The sample dimensions after polishing were approximately $3 \times 1.5 \times 0.5$ mm^3.

The synchrotron experiments were carried out at the bending magnet beamline X22C of the National Synchrotron Light Source, using a Ge$(1,1,1)$ double bounce monochromator and an asymmetric cut Ge$(1,1,1)$ analyzer. A Ni-coated toroidal focusing mirror upstream of the monochromator was used to eliminate higher harmonics in the incident beam. The sample was mounted on the cold finger of a Heliplex closed cycle refrigerator (base temperature 3.5 K) so that its $(h,0,l)$-zone was coincident with the vertical scattering plane of the diffractometer. The mosaic spread of the $(h,0,0)$ reflections was characterized by a full width at half maximum (FWHM) of 0.04°. For the measurements of the crystal lattice distortion, the incident photon energy was tuned to 8 keV, well below the Er $\mathrm{L}_{1,2,3}$ and the Ni K absorption edges.

Above $\mathrm{T}_N = 6$ K, clearly defined Bragg peaks (h,k,l) with a characteristic width (FWHM) of 0.003 Å^{-1} were observed at $h+k+l=2n$, where n is an integer. The only structure present in these peaks is a slight asymmetry that is also seen in scans through the incident beam. We therefore have taken these peaks to be resolution limited.

Fig. 5.14 shows longitudinal scans across the $(2,0,0)$ Bragg peak for selected temperatures. As the sample is cooled below T_N, the peak first broadens and then splits, consistent with a tetragonal to orthorhombic phase transition. The high- and low-**Q** peaks then correspond to the $(0,2,0)$ and $(2,0,0)$ Bragg peaks of separate domains that are rotated by 90° relative to each other around their $(0,0,1)$ axes. No hysteresis was observed when these measurements were repeated on warming.

Fig. 5.14 shows longitudinal scans through the $(2,0,0)$ Bragg peak for selected temperatures. As the sample is cooled below $\approx$6.3 K, the peak first broadens and then splits, consistent with a tetragonal to orthorhombic phase transition. The high- and

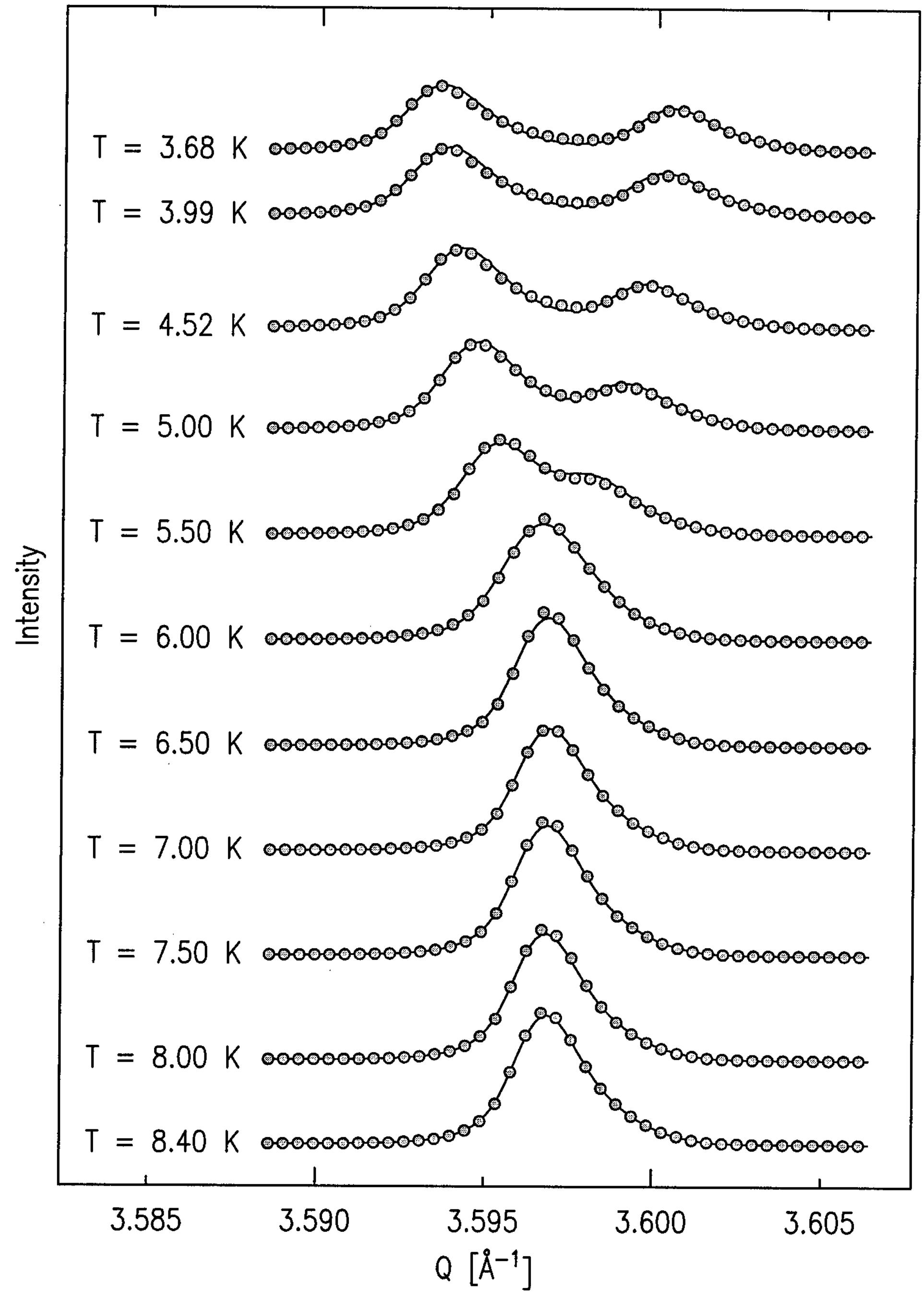

Figure 5.14 Representative longitudinal scans of the $(2,0,0)$ Bragg peak at selected temperatures. The solid lines represent the results of least-squares fits as described in the text. The scan taken at 8.40 K was assumed to be resolution limited and was used as a reference scan for the fitting procedure.

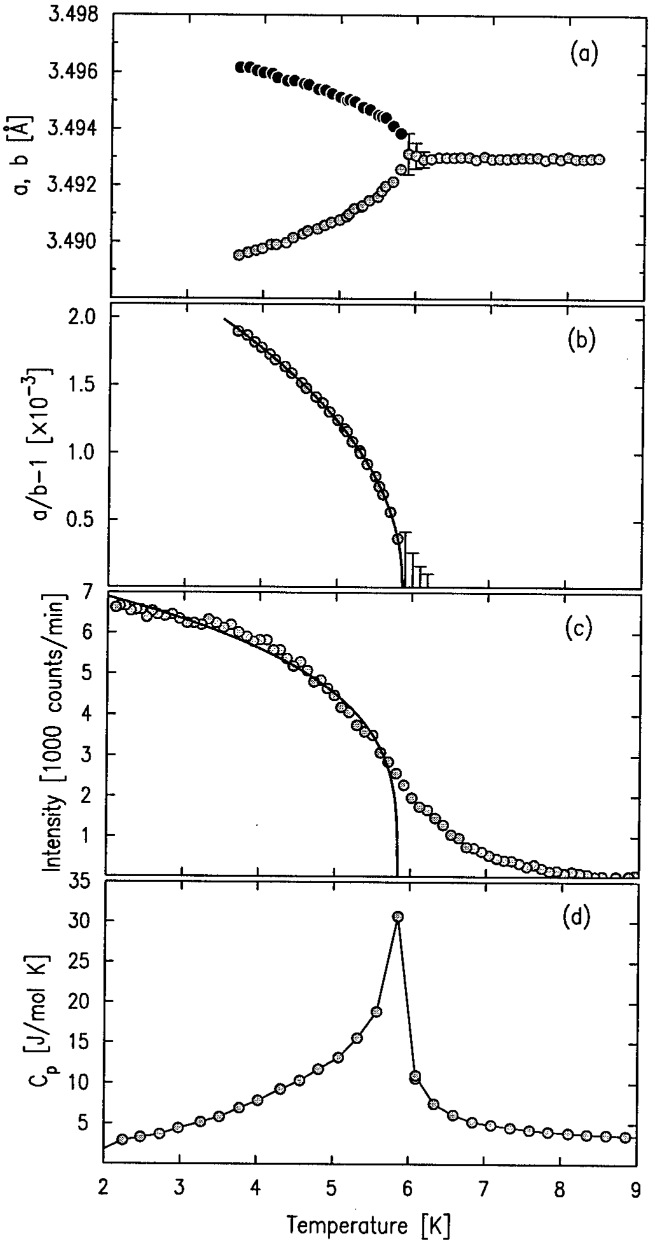

Figure 5.15 (a) The a and b lattice parameters extracted from a set of longitudinal scans of the $(2,0,0)$ Bragg peak. (b) The distortion-order parameter, $a/b-1$. The line represents a least-squares fit to a power law, $A(1-\mathrm{T}/\mathrm{T}_N)^{2\beta}$, as discussed in the text. (c) Intensity of a magnetic Bragg reflection, from Ref. [Sin95]. The line represents a least-squares fit to a power law. (d) Specific heat, C_p, in zero applied field, from Ref. [Cho95b].

low-**Q** peaks then correspond to the $(0,2,0)$ and $(2,0,0)$ Bragg peaks of separate domains that are rotated by 90° relative to each other around their $(0,0,1)$ axes. No hysteresis was observed when these measurements were repeated on warming. Despite the relative ease encountered in other rare-earth borocarbides[Det96, Hil96a, Det97], we were unable to observe x-ray magnetic scattering at the Er L_3 resonance (8.358 keV) in this material. We believe this is a result of the strong absorption arising from the combination of Ni in the sample and in the mirror, and the presence of the nearby Ni-K edge (8.333 keV).

Fig. 5.15 summarizes the temperature dependence of the $(2,0,0)$ Bragg peak as measured on cooling. The lattice parameters, a and b, were extracted by fitting each scan to the convolution of a resolution limited reference scan (8.40 K) with two Gaussian lineshapes with a fixed width. The results of this procedure are displayed in Fig. 5.15(a). In the temperature range between 5.9 and 6.3 K, the raw data shows a slight broadening of the $(2,0,0)$ Bragg peak and, within the resolution of this experiment, it is not possible to distinguish two separate peaks. This broadening is therefore represented by the error bars shown in Fig. 5.15(a) and (b). The line in Fig. 5.15(b) shows the result of fitting the splitting, $a/b-1$, to a power law in the reduced temperature. For the fit shown in the figure, $T_N = 5.9 \pm 0.2$ K. In Fig. 5.15(c), we show the intensity of a magnetic Bragg reflection as measured by neutron powder diffraction [Sin95]. A least-squares fit to a power law, represented by the line, indicates a ordering temperature $T_N \approx 5.9 \pm 0.5$ K. While this ordering temperature agrees with the values obtained from the splitting and from magnetization measurements (Fig. 5.15(d)), it is lower than those reported by Sinha *et al.* (T_N = 6.8 K, Ref. [Sin95]), obtained from a fit to a Brillouin function, and by Zarestky *et al.* ($T_N \approx 7$ K, Ref. [Zar95]). We attribute the differences in T_N to critical scattering observed above the ordering temperature. Finally, in Fig. 5.15(d), we present the specific heat of $ErNi_2B_2C$ as measured by Cho *et al.* (Ref. [Cho95b]) in zero applied field. These authors observed a large, lambda shaped anomaly with a peak at 5.9 ± 0.2 K, which they associated with the transition of the Er sublattice from paramagnetism to antiferromagnetic order.

To verify that the symmetry at low temperatures is indeed orthorhombic, we studied a sample prepared from crushed single crystals at the high-resolution powder diffractometer H1A of the High Flux Beam Reactor at Brookhaven National Laboratory. A full profile analysis, using the FULLPROF-code[Rod93], was performed on the data taken at $T = 3.4$ K. The results are consistent with an orthorhombic distortion as mentioned above. Due to low counting statistics and some strain broadening, however, it was not possible to determine from the refinement if the magnetic modulation wave vector is oriented along the long (a) or the short (b) basal plane axis.

This type of magneto-elastic distortion is common in rare-earth compounds (see for example Ref. [Mor90] and references therein). Quantitative calculations of the shape of the magnetic orbitals and the resulting magneto-elastic distortion require precise evaluation of the competing CEF, elastic and magnetic terms in the Hamiltonian[Mor90], and have not been performed. Nonetheless, we may draw some qualitative conclusions about the other materials in the series.

For the Gd member of the $R\mathrm{Ni}_2\mathrm{B}_2\mathrm{C}$ family, which orders with an antiferromagnetic structure very similar to that of the Er compound, we do not expect a magneto-elastic distortion, since the Gd^{3+} ion in its ground state, ${}^8S_{7/2}$, has spherical symmetry. Indeed, no magneto-elastic effects were observed in an earlier high-resolution x-ray study[Det96] of this material. In addition, no magneto-elastic effects were observed in high resolution x-ray experiments on the Sm and Nd compounds[Hil96a, Det97]. In the Sm compound, the moments are aligned parallel to (0, 0, 1), so that magneto-strictive effects would change the a/c ratio without breaking the crystal symmetry. In $\mathrm{HoNi}_2\mathrm{B}_2\mathrm{C}$ a small magnetostriction was observed as an increase in the mosaic width of nuclear reflections in earlier neutron experiments[Gol94]. For $TbNi_2B_2C$, which orders into a longitudinal spin density wave state with modulation wave vector $(0.55, 0, 0)$, we expect a magneto-elastic tetragonal to orthorhombic distortion similar to that of the Er compound. High resolution x-ray diffraction experiments to probe the structure of this material are planned.

$NdNi_2B_2C$ and $SmNi_2B_2C$

In this section, we present determinations of the magnetic structures of $NdNi_2B_2C$ and $SmNi_2B_2C$ by means of x-ray resonant exchange scattering (XRES) . The integrated intensity of a number of magnetic reflections was measured as a function of the Bragg angle and compared to model calculations for various magnetic structures. The two compounds were found to have the same magnetic modulation wave-vector but different moment directions. A resonant feature observed below the Sm L_3-absorption edge, similar to unexplained effects found in other light rare earth compounds, is identified as quadrupolar XRES and is used to refine the details of the moment direction.

Here, we demonstrate that it is possible to determine moment directions using resonant x-ray magnetic scattering. We have chosen to study two related compounds, $NdNi_2B_2C$ and $SmNi_2B_2C$, both of which order in a commensurate antiferromagnetic structure with propagation vector $(\frac{1}{2}, 0, \frac{1}{2})$. As detailed in the introduction, these materials are interesting as members of the recently discovered [Nag94, Cav94a, Cav94b, Eis94, Sie94a] rare-earth nickel boron carbide family, which includes some antiferromagnetic superconductors.

The experiments were carried out at beamline X22C of the National Synchrotron Light Source. The samples were mounted in a closed cycle refrigerator such that the $(h0l)$-zone was coincident with the diffraction plane (Fig. 5.16). The mosaic spreads of the $(00l)$ reflections were approximately 0.09° and 0.14° full width at half maximum for the Nd- and Sm- compounds, respectively.

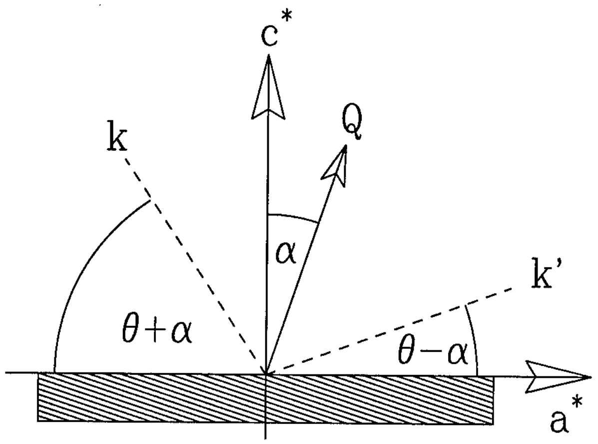

Figure 5.16 The scattering geometry used in the present measurements with respect to the **a**-, **b**-, and **c**-axes of the sample. The incident x-ray polarization is directed out of the scattering plane (σ polarization), along the **b**-axis. The alignment of the crystal was such that reflections $(h, 0, l)$ with positive index $h > 0$ have positive asymmetry angles, $\alpha > 0$.

For the sample orientation shown in Fig. 5.16, the x-ray resonant scattering cross-section (the nonresonant scattering contribution was observed to be negligible) may be written as

$$I \propto \left| \sum_n e^{i\mathbf{Q}\cdot\mathbf{r}_n} F_n^{\mathrm{XRES}}(\mathbf{k}, \hat{\epsilon}, \mathbf{k}', \hat{\epsilon}', \hat{z}_n) \right|^2 \cdot \frac{\sin(\theta+\alpha)\sin(\theta-\alpha)}{2\mu\sin(\theta)\cos(\alpha)\sin(2\theta)}. \tag{5.3}$$

Here $\mathbf{k}$,$\hat{\epsilon}$ and $\mathbf{k}', \hat{\epsilon}'$ are the wave vector and polarization of the incident and scattered x-ray beams, respectively, and $\hat{z}_n$ is the moment direction at n-th site. α represents the "asymmetry" angle between the scattering vector, $\mathbf{Q} = \mathbf{k}' - \mathbf{k}$, and the surface normal, $\mathbf{c}^*$ (Fig. 5.16). μ is the linear absorption coefficient and 2θ is the scattering angle. The Lorentz factor, $1/\sin(2\theta)$, as well as an angular factor required to correct for the fraction of the incident beam intercepted by the sample, $\sin(\theta+\alpha)$, are included to allow a comparison between the calculated cross section and the measured integrated intensity, I. The resonant scattering amplitude, F_n^{XRES}, contains both dipole (E1) and quadrupole (E2) resonances, with the former typically dominant. At the RE $L_{2,3}$-edges, these correspond to $2p \leftrightarrow 5d$ and $2p \leftrightarrow 4f$ transitions, respectively. The E2 transition is generally observed a few eV below the absorption edge, due to the stronger core-hole – excited electron interaction in the intermediate state. The two processes contribute distinct angular factors and it is these which we will exploit to determine the moment directions.

The E1-resonances produce first and second order harmonic satellites of the charge peaks, while E2-resonances give rise to satellites of up to fourth order [Gib88, Gib91, Han88]. For a commensurate antiferromagnet the odd orders contribute to the magnetic scattering and we need only consider terms of 1st and 3rd order in $\hat{z}_n$. For the present experiment, with a σ-polarized incident beam (i.e perpendicular to the scattering plane), these are [Hil96b],

$$
\begin{aligned}
F^{\mathrm{XRES}}_{\mathrm{E1,1st}}(\mathbf{k},\mathbf{k}') &= -iF^{(1)}_{\mathrm{E1}} \begin{pmatrix} 0 \\ -D' \end{pmatrix} && (5.4) \\
F^{\mathrm{XRES}}_{\mathrm{E2,1st}}(\mathbf{k},\mathbf{k}') &= -iF^{(1)}_{\mathrm{E2}} \begin{pmatrix} C \\ -\cos(2\theta)D' \end{pmatrix} && (5.5) \\
F^{\mathrm{XRES}}_{\mathrm{E2,3rd}}(\mathbf{k},\mathbf{k}') &= -i\frac{F^{(3)}_{\mathrm{E2}} - F^{(1)}_{\mathrm{E2}}}{\sin^2(2\theta)} \begin{pmatrix} C^3 \\ -D'D\sin^2(2\theta) - C^2[D - \cos(2\theta)D'] \end{pmatrix} \\
&\quad -i\frac{F^{(3)}_{\mathrm{E2}}}{\sin^2(2\theta)} \begin{pmatrix} C[2\cos(2\theta)D'D - (D')^2 - D^2] \\ C^2\cos(2\theta)D' + D[D - \cos(2\theta)D']^2 \end{pmatrix}, && (5.6)
\end{aligned}
$$

where we have adopted a column vector notation, such that the top element describes the $\sigma \rightarrow \sigma$ scattering and the bottom element the $\sigma \rightarrow \pi$ scattering. $C := (\hat{k}' \times \hat{k}) \cdot \hat{z}_n$, $D := \hat{k} \cdot \hat{z}_n$, and $D' := \hat{k}' \cdot \hat{z}_n$. The amplitude factors, $F^{(1)}_{\mathrm{E1}}$, $F^{(1)}_{\mathrm{E2}}$, and $F^{(3)}_{\mathrm{E2}}$, are a combination of Clebsch-Gordan coefficients, the resonant energy denominator and radial dipole or quadrupole matrix elements, respectively [Hil96b]. They are independent of the scattering geometry.

A few points regarding the present scattering geometry are in order. First, in the absence of an in-plane (π) polarized component of the incident beam, the E1 terms are not sensitive to the component of the ordered moment perpendicular to the scattering plane (i.e. along the **b**-axis). Second, the magnetic scattering intensity is not symmetric in α, in contrast to charge scattering for which the intensities are identical for reflections at α and $-\alpha$ (($\pm h0l$) Bragg peaks).

We first investigated $NdNi_2B_2C$, for which the modulation wave-vector is known to be $(\frac{1}{2}, 0, \frac{1}{2})$ with the moment direction along the (100) direction [Lyn97]. The measurements were made at the maximum of the Nd L_2 resonance. Above the Néel-temperature, $T_N = 4.5$ K [Can00c], only charge reflections (h, k, l) with $h + k + l = 2n$ were observed. The resonant scattering at the Nd L_3 energy was too weak to be observed in these measurements. Below T_N, satellites of the charge peaks appeared at $(h, k, l) \pm \mathbf{q}$ with $\mathbf{q}=(\frac{1}{2}, 0, \frac{1}{2})$. Peak intensities were $\sim$50 counts s^{-1}. The integrated intensities of pairs of equivalent satellites, $(\pm\frac{1}{2}, 0, l)$, corresponding to opposite asymmetry angles, $\pm\alpha$, were measured at T = 3.7 K by performing rocking scans with the analyzer crystal removed and the detector slits set to accept the full scattered beam. These data were then numerically integrated [Det96]. The results of such a procedure are plotted as open circles in Fig. 5.17, together with the calculated dipole integrated intensity (dashed line) from eqns (5.3) and (5.4) for $\hat{z}_n \parallel (1, 0, 0)$. The data are well described by such a structure and we conclude that our results are consistent with the neutron work [Lyn97], with the caveat that, for dipolar transitions, the x-ray measurement is not sensitive to any **b**-axis component of the magnetic moment.

With this reassurance, we next turn to $SmNi_2B_2C$, for which there is no previous microscopic information. In scans taken along the high symmetry directions below the Néel temperature, $T_N = 9.8$ K [Can00c], magnetic satellites were again observed at $(h, k, l) \pm \mathbf{q}$, with $\mathbf{q} = (\frac{1}{2}, 0, \frac{1}{2})$. The integrated intensities of the magnetic reflections were recorded at the L_2 resonance and are plotted in Fig. 5.17 (closed circles), along with the calculated dipole scattering from a moment parallel to $(0, 0, 1)$ (solid line).

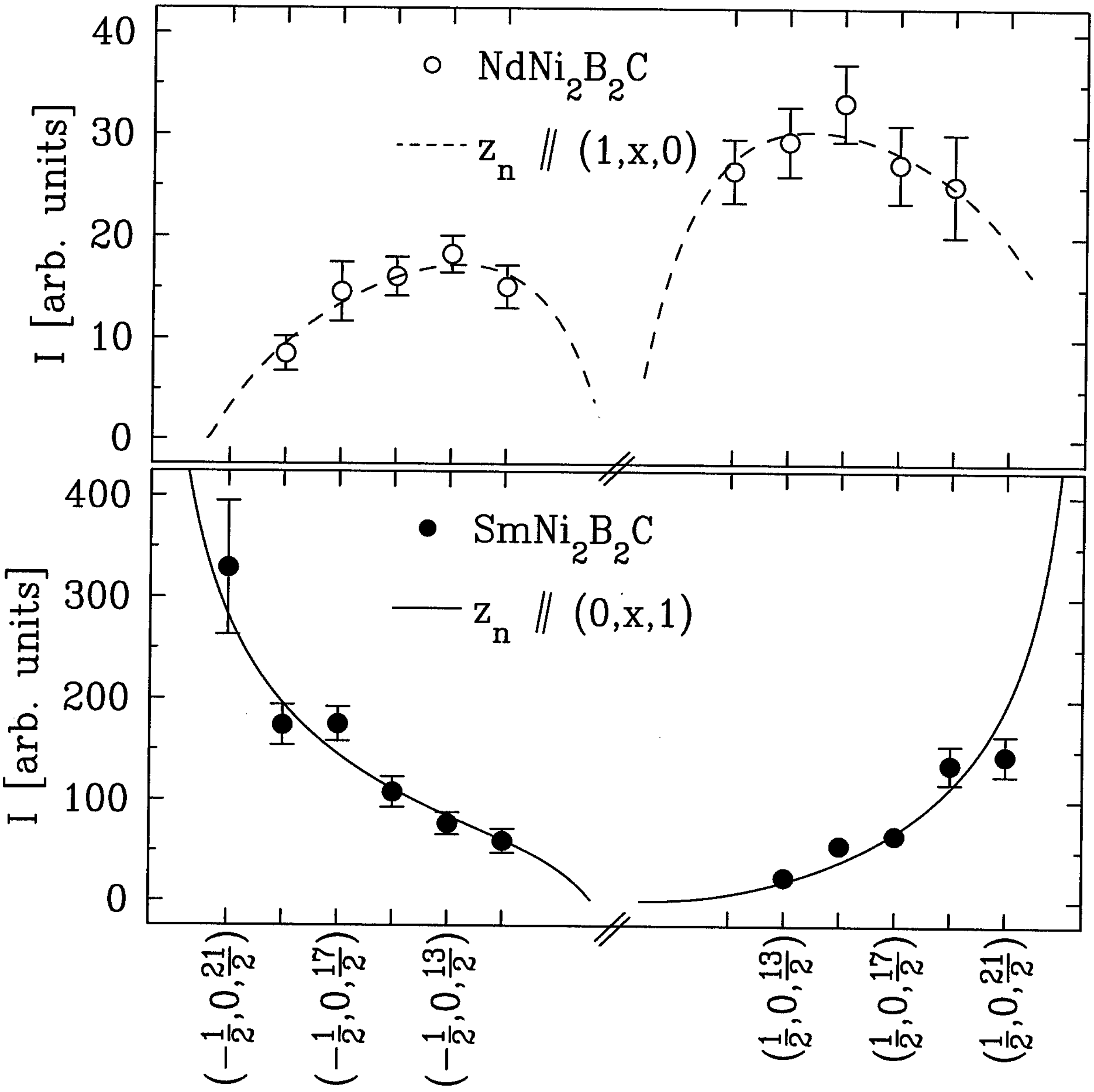

Figure 5.17 The integrated intensity of magnetic reflections of $SmNi_2B_2C$ (•) and $NdNi_2B_2C$ (∘) along with model calculations for a magnetic moment parallel to the **c** (——) and **a** (– – –) axes of the samples. The symbol x is used to remind the reader that these measurements are not sensitive to components of the magnetic moment along the **b**-axes.

While both compounds have the same modulation wave vector, their integrated intensities exhibit strikingly different behaviors as a function of the scattering angle. These differences result entirely from the different moment orientations in the two compounds and demonstrate the sensitivity of this technique to the moment direction. Both sets of data are well described by eqns. (5.3) and (5.4), assuming a magnetic moment direction along $(1, x, 0)$ for $NdNi_2B_2C$ and along $(0, x, 1)$ for $SmNi_2B_2C$, with only one adjustable parameter (the overall amplitude) for each sample. Due to the multipole expansion in the single-atom matrix elements, the XRES scattering amplitude is a discrete sum rather than a continuous Fourier transform of the moment density, so that no magnetic form factor is required to fit the data [Han88].

A second, independent data set was then obtained for $SmNi_2B_2C$ at the Sm L_3-absorption edge. As for pure Sm [Wat95], the resonant signal at the Sm L_3-edge was roughly one order of magnitude weaker than at the L_2-edge. Further, as observed in other light rare-earth compounds [Wat95, Zhe96, Hil95], energy scans across the Sm L_3-edge showed two separate peaks. These scans are shown in Fig. 5.18, uncorrected for absorption effects. The double peak structure is present at all satellites, $(-\frac{1}{2}, 0, l)$, though the relative intensity of the low energy peak decreases with increasing Bragg angle.

The angular dependence of this lower energy resonance is a clear indication that is does *not* originate from E1 transitions (compare with Fig. 5.17) and we therefore ascribe it to E2 processes [Gib88, Gib91]. The intensity ratio of the two L_3 features was extracted for each magnetic Bragg reflection by fitting the data to a sum of two Lorentzian-squared functions and is plotted in Fig. 5.19. We may compare this to the theoretical quadrupole to dipole ratio, which is proportional to $\left|(F^{\mathrm{XRES}}_{\mathrm{E2,1st.}} + F^{\mathrm{XRES}}_{\mathrm{E2,3rd}})/F^{\mathrm{XRES}}_{\mathrm{E1,1st.}}\right|^2$, remembering that for $\mathbf{q} = (\frac{1}{2}, 0, \frac{1}{2})$ the first and the third harmonic satellites coincide.

The E2 amplitude factors, $F^{(1)}_{\mathrm{E2}}$ and $F^{(3)}_{\mathrm{E2}}$, may be approximated by their free-ion val-

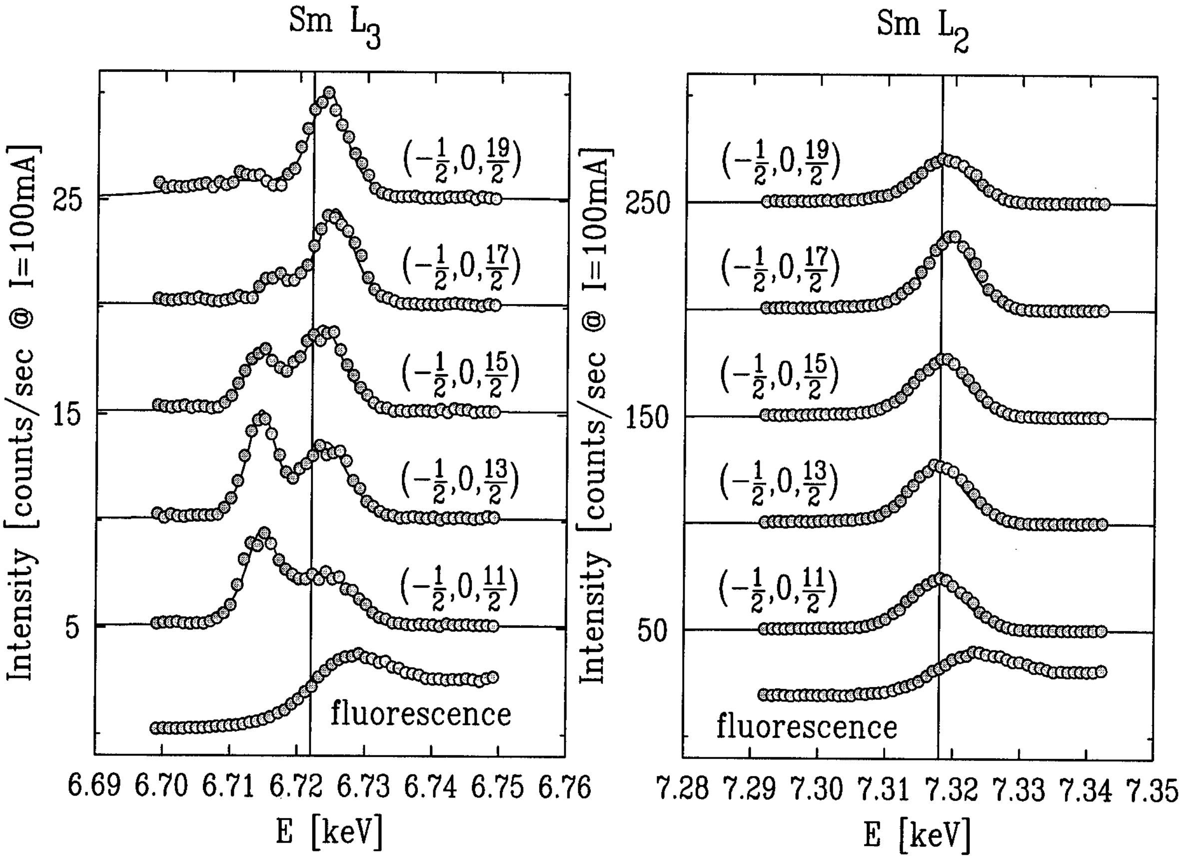

Figure 5.18 Energy scans of the $(-\frac{1}{2}, 0, l)$ magnetic reflection across the Sm $L_{2,3}$ absorption edges. The fluorescence yield is plotted as an energy reference. Note that an absorption correction (not performed) would strongly increase the E1 features above the edge. The solid lines represent fits to the Sm L_3 (Sm L_2) data using two (one) Lorentzian-squared line shapes, respectively.

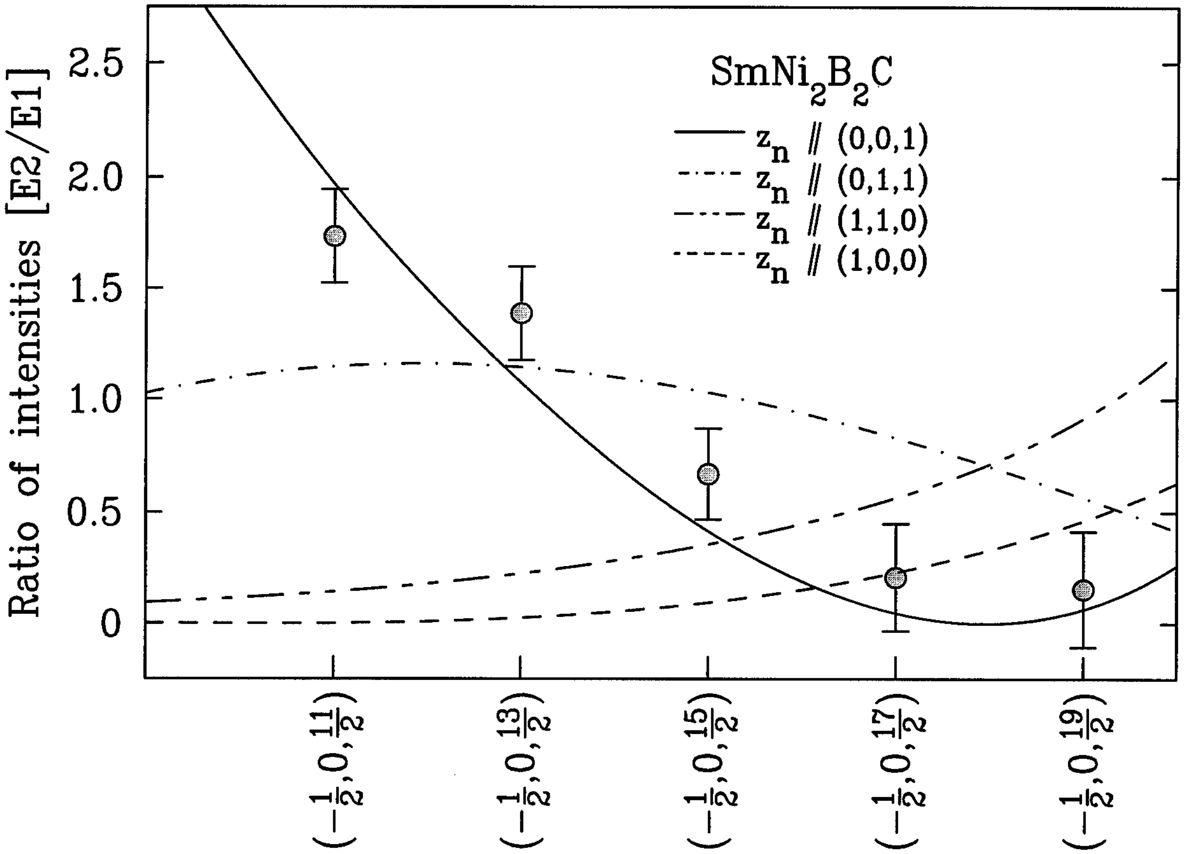

Figure 5.19 The ratio of the intensities of dipolar and quadrupolar scattering along with model calculations for several directions of the magnetic moments.

ues, since they describe intra-atomic transitions ($2p \leftrightarrow 4f$). We have used $F^{(1)}_{\mathrm{E2}}/F^{(3)}_{\mathrm{E2}} = 2$ [Ham94, Kön96a]. The only adjustable parameter is then an overall amplitude proportional to $F^{(1)}_{\mathrm{E2}}/F^{(1)}_{\mathrm{E1}}$. Note that an absorption correction, which has not been performed, would affect only this factor. The solid line in Fig. 5.19 is the result of such a calculation for an ordered moment along the $(0, 0, 1)$ direction. The dot-dashed line represents the result of the same calculation for a moment along the (0,1,1) direction. Clearly the latter does not fit the data satisfactorily. A least-squares fit to the data reveals that the magnetic moments lie within about 20° of the **c**-axis. Thus, by measuring the quadrupolar scattering, which is sensitive to a **b**-axis spin component, we can conclude that – within the accuracy of our measurement – the moments are along the (0,0,1) direction in $\mathrm{SmNi_2B_2C}$.

We note that there are no indications of quadrupolar contributions to the Sm $\mathrm{L_2}$ resonance. This is consistent with calculations which indicate that the absolute quadrupolar contributions to the $\mathrm{L_2}$ resonant signal is $\sim$4 times weaker than at the $\mathrm{L_3}$-edge [Kön96a].

In summary, x-ray resonant exchange scattering was observed at the Nd $\mathrm{L_2}$-absorption edge in $\mathrm{NdNi_2B_2C}$ and both the Sm $\mathrm{L_2}$- and $\mathrm{L_3}$-absorption edges in $\mathrm{SmNi_2B_2C}$. Below their respective Néel temperatures, $T_N = 4.5$ K and 9.8 K, the compounds order antiferromagnetically with a modulation wave vector of $\mathbf{q} = (\frac{1}{2}, 0, \frac{1}{2})$ (or the tetragonally equivalent $\mathbf{q} = (0, \frac{1}{2}, \frac{1}{2})$). The angular dependence of the resonant scattering intensity was used to determine the direction of the magnetic moments. A second resonant peak observed below the Sm $\mathrm{L_3}$-absorption edge in energy scans of the magnetic reflections was attributed to quadrupolar transitions. This leads us to believe that similar $\mathrm{L_3}$ features observed in pure Sm [Wat95] and several Nd compounds [Zhe96, Hil95] are also quadrupolar in origin.

Finally, the significance of this work lies in the demonstration of the ability of x-ray resonant exchange scattering to determine moment directions with no *a priori* information. It is hoped that these results will extend the utility of the technique in future works.

6 SUMMARY

In summary, we have studied the magnetic structure of several rare-earth nickel borocarbides, $R\mathrm{Ni_2B_2C}$, using x-ray resonant exchange scattering (XRES). A large variety of magnetic structures exists in these materials, ranging in complexity from the simple antiferromagnet with modulation wave vector $\mathbf{q} = (0,0,1)$ observed at low temperatures in $\mathrm{HoNi_2B_2C}$, through the commensurate structure with $\mathbf{q} = (\frac{1}{2},0,\frac{1}{2})$ of the Nd and Sm compounds, to the incommensurate intermediate temperature phase of $\mathrm{HoNi_2B_2C}$ with its multiple modulation wave vectors.

XRES utilizes atomic absorption edges to obtain large enhancements in the magnetic scattering cross section [Gib88, Han88]. This technique can offer distinct advantages over the more conventional neutron techniques, for example for materials that contain neutron opaque elements (Cd, Sm, Eu, Gd, etc.), or very small samples. Its element specifity makes it particularly interesting for mixed spin systems, since, in principle, it is possible to determine the temperature dependence and direction of the ordered moment of each sublattice with a model-independent procedure [Det96, Det97, Isl00b], in contrast to neutron-scattering methods. In addition, x-ray magnetic scattering offers the ability to study surface magnetism [Wat96a], and the potential to resolve orbital and spin contributions through the use of XRES sum rules [Car94, Luo93] or the non-resonant x-ray scattering cross section [Gru00]. Finally, the order-of-magnitude increase in **Q**-resolution afforded by x-ray measurements at synchrotron sources allows a more detailed investigation of the behavior of the magnetic structure over large (several micrometer) length scales [Hil96a].

In the present work, we illustrated the main elements of the theory underlying XRES, with special attention to the dependence of the scattering amplitude upon the experimental geometry, the orientation of the magnetic moments, and the mechanism leading to the formation of magnetic satellite peaks. Also, we briefly described the interactions determining the magnetic order in the rare-earth borocarbides, and demonstrated how magnetic and crystalline electric field (CEF) interactions compete and induce magnetic anisotropy.

Next, we reported the results of the XRES experiments we performed on $HoNi_2B_2C$, $GdNi_2B_2C$, $ErNi_2B_2C$, $NdNi_2B_2C$ and $SmNi_2B_2C$. For temperatures below 5 K, the Ho compound orders in a simple antiferromagnetic state with modulation wave vector $\mathbf{q} = (0, 0, 1)$, while between 5 K and 6.1 K an incommensurate antiferromagnetic phase with two modulation wave vectors, $\mathbf{q}_a = (0.59, 0, 0)$ and $\mathbf{q}_c = (0, 0, 0.92)$ is observed. Furthermore, our high resolution x-ray studies showed that the **c**-axis modulation consists of two separate wave vectors [Hil96a]. $GdNi_2B_2C$ orders antiferromagnetically below $T_N = 19.4$ K with $\mathbf{q} = (0.55, 0, 0)$. Between 19.4 K and 13.6 K, the magnetic moments are aligned along the **b**-axis of the crystal and the modulation wave vector decreases with decreasing temperatures. Below 13.6 K an additional component along the **c**-axis develops, and the modulation wave vector increases upon lowering of the temperature [Det96]. In $ErNi_2B_2C$, the paramagnetic-to-antiferromagnetic phase transition at $T_N \approx$ 6 K is accompanied by spontaneous magnetostriction which lowers the lattice symmetry from tetragonal to orthorhombic [Det00]. The antiferromagnetic structures of the Nd and Sm compounds are characterized by a modulation wave vector $\mathbf{q} = (\frac{1}{2}, 0, \frac{1}{2})$, while the moment directions were determined as (1, 0, 0) and (0, 0, 1), respectively [Det97]. In $SmNi_2B_2C$, we observed a quadrupolar resonance below the Sm L_3 absorption edge in addition to the usual dipole resonance above the absorption edge, Our measurements of these materials have not only demonstrated that high resolution synchrotron x-ray measurements can confirm and refine magnetic neutron diffraction experiments, but that furthermore XRES is a tool capable of *ab initio* structure determinations. In particular, we have shown that by measuring the integrated intensity of selected magnetic Bragg reflections and comparing them with model calculation of the **Q**-dependence, it is possible to determine the orientation of magnetic moments in antiferromagnetically ordered phases.

BIBLIOGRAPHY

[Alt95] M. Altarelli, M. D. Núñez-Regueiro and M. Papoular, Phys. Rev. Lett. **74** 3840 (1995).

[Alt94] S. L. Altmann and P. Herzig, *Point group theory tables*, Clarendon press (1994).

[Bat64] B. W. Batterman and H. Cole, Rev. Mod. Phys. **36**, 681 (1964).

[Bet29] H. A. Bethe, *Termaufspalltung in Kristallen*, Ann. Physik [5] **3**, 133 (1929).

[Ble53] B. Bleaney, and K. W. H. Stevens, Rept. Progr. Phys. **16**, 108 (1953).

[Blu85] M. Blume, J. Appl. Phys. **57**, 3615 (1985).

[Blu88] M. Blume and D. Gibbs, Phys. Rev. B **37**, 1779 (1988).

[Bou73] P. Boutron, Phys. Rev. B **7**, 3226 (1973).

[Bud95] S. L. Bud'ko, M. B. Fontes, D. Aliaga-Guerra, and M. B. Baggio-Saitovitch, Phys. Rev. B **52**, 305 (1995).

[Brü96] T. Brückel, M. Lippert, T. Köhler, J. R. Schneider, W. Prandl, V. Rilling, and M. Schilling, Acta Crystallogr. Sect. A **52**, 427 (1996).

[Can94] P. C. Canfield, B. K. Cho, D. C. Johnston, D. K. Finnemore and M. F. Hundley, Physica C **230**, 397 (1994).

[Can95] P. C. Canfield, B. K. Cho and K. W. Dennis, Physica **215 B**, 337 (1995).

[Can96] P. C. Canfield, S. L. Bud'ko, and B. K. Cho, Physica C **262**, 249 (1996).

[Can97a] P. C. Canfield, S. L. Bud'ko, B. K. Cho, A. Lacerda, D. Farrell, E. Johnston-Halperin, V. A. Kalatsky, and V. L. Pokrovsky, Phys. Rev. B **55**, 970 (1997).

[Can97b] P. C. Canfield, private communication (1997).

[Can00a] P. C. Canfield, (to be published).

[Can00b] P. C. Canfield and S. L. Bud'ko, J. Alloys Compounds (to be published).

[Can00c] P. C. Canfield *et al.*, (to be published).

[Car90] P. Carra and M. Altarelli, Phys. Rev. Lett **64**, 1286 (1990).

[Car93] P. Carra, B. T. Thole, M. Altarelli, and X. Wang, Phys. Rev. Lett. **70**, 694 (1993).

[Car94] P. Carra and B. T. Thole, Rev. Mod. Phys. **66**, 1509 (1994).

[Car95] P. Carra, M. Fabrizio, and B. T. Thole, Phys. Rev. Lett. **74**, 3700 (1995).

[Cav94a] R. J. Cava, H. Takagi, H. W. Zandbergen, J. J. Krajewski, W. F. Peck, Jr., T. Siegrist, B. Batlogg, R. B. van Dover, R. J. Felder, K. Mizuhashi, J. O. Lee, H. Eisaki and S. Uchida, Nature **367**, 252 (1994).

[Cav94b] R. Cava, H. Takagi, B. Batlogg, H. W. Zandbergen, J. J. Krajewski, W. F. Peck, Jr., R. B. van Dover, R. J. Felder, T. Siegrist, K. Mizuhashi, J. O. Lee, H. Eisaki, S. A. Cater and S. Uchida, Nature **367**, 146 (1994).

[Cav97] R. J. Cava, private communication (1997).

[Cha96] L. J. Chang, C. V. Tomy, D. McK. Paul, and C. Ritter, Phys. Rev. B **54**, 9031 (1996).

[Cho95a] B. K. Cho, M. Xu, P. C. Canfield, L. L. Miller, and D. C. Johnston, Phys. Rev. B **52**, 3676 (1995).

[Cho95b] B. K. Cho, P. C. Canfield, L. Miller, D. C. Johnston, W. P. Beyermann and A. Yatskar, Phys. Rev. B **52** 3684 (1995).

[Cho95c] B. K. Cho, P. C. Canfield, D. C. Johnston, Phys. Rev. B **52**, R3844 (1995).

[Cho95d] B. K. Cho, Ph.D. Thesis, Iowa State University (1995).

[Cho96a] B. K. Cho, P. C. Canfield, and D. C. Johnston, Phys. Rev. B **53**, 8499 (1996).

[Cho96b] B. K. Cho, B. N. Harmon, D. C. Johnston and P. C. Canfield, Phys. Rev. B **52**, R3844 (1996).

[Cho96c] B. K. Cho, P. C. Canfield, and D. C. Johnston, Phys. Rev. Lett. **77**, 163 (1996).

[Coe94] R. Coehoorn, Physica C **228**, 331 (1994).

[Cow92] R. A. Cowley and J. Jensen, J. Phys. **C 4**, 9673 (1992).

[Cul78] B. D. Cullity, *Elements of X-Ray Diffraction*, second edition, Addison-Wesley, Reading MA (1978).

[deB72] F. de Bergevin and M. Brunel, Phys. Lett. A **39**, 141 (1972).

[deB81a] F. de Bergevin and M. Brunel, Acta Crystallogr. Sect. A **37**, 314 (1981).

[deB81b] F. de Bergevin and M. Brunel, Acta Crystallogr. Sect. A **37**, 324 (1981).

[Ded93] P. H. Dederichs, *Friedeloszillationen, RKKY Wechselwirkung und Zwischenlagenkopplung*, in P. H. Dederichs, P. Grünberg, and W. Zinn (eds.), 24. IFF-Ferienkurs *Magnetismus von Festkörpern und Grenzflächen*, Vorlesungsmanuscripte, Forschungszentrum Jülich GmbH (1993).

[Der95a] P. Dervenagas, M. Bullock, J. Zarestky, P. Canfield, B. K. Cho, B. Harmon, A. I. Goldman, and C. Stassis, Phys. Rev. B **52**, R9839 (1995).

[Der95b] P. Dervenagas, J. Zarestky, C. Stassis, A. I. Goldman, P. C. Canfield, B. K. Cho, Physica B **212**, 1 (1995).

[Der96] P. Dervenagas, J. Zarestky, C. Stassis, A. I. Goldman, P. C. Canfield, and B. K. Cho, Phys. Rev. B **53**, 8506 (1996).

[Det96] C. Detlefs, A. I. Goldman, C. Stassis, P. C. Canfield, B. K. Cho, J. P. Hill, and D. Gibbs, Phys. Rev. B **53**, 6355 (1996).

[Det97] C. Detlefs, A. H. M. Z. Islam, A. I. Goldman, C. Stassis, P. C. Canfield, J. P. Hill, and D. Gibbs, Phys. Rev. B **55**, 680 (1997).

[Det00] C. Detlefs, A. H. M. Z. Islam, T. Gu, A. I. Goldman, C. Stassis, P. C. Canfield, J. P. Hill, D. Gibbs, and T. Vogt, (unpublished).

[Dha96] S. K. Dhar, R. Nagarajan, Z. Hossain, E. Tominez, C. Godart, L. C. Gupta, and R. Vijayaraghavan, Sol. St. Commun. **98**, 985 (1996).

[Eis94] H. Eisaki, H. Takagi, R. J. Cava, K. Mizuhashi, J. O. Lee, B. Batlogg, J. J. Krajewski, W. F. Peck, Jr. and S. Uchida, Phys. Rev. B **50**, 647 (1994).

[Ell57] R. J. Elliott, R. B. Judd, and W. A. Runciman, Proc. Roy. Soc. **A240**, 509 (1957).

[ElM94] M. El Massalami, S. L. Bud'ko, B. Giordanengo, M. B. Fontes, J. C. Mondragon, and E. M. Baggio-Saitovitch, Physica C **235-240**, 2563 (1994).

[Ewa17] P. P. Ewald, Ann. Physik **54**, 519 (1917).

[Ewa37] P. P. Ewald, Z. Krist. (A) **97**, 1 (1937).

[Ewa65] P. P. Ewald, Rev. Mod. Phys. **37**, 46 (1965).

[Esk97] M. R. Eskildsen, P. L. Gammel, B. P. Barber, A. P. Ramirez, D. J. Bishop, N. H. Andersen, K. Mortensen, C. A. Bolle, C. M. Lieber, and P. C. Canfield, Phys. Rev. Lett. **78**, 1968 (1997).

[Fer77] W. A. Fertig, D. C. Johnston, L. E. DeLong, R. W. McCallum, M. B. Maple, and B. T. Matthias, Phys. Rev. Lett. **38**, 987 (1977).

[Fis75] Ø. Fischer, A. Treyvaud, C. Chevrel, and M. Sergen, Solid State Commun. **17**, 721 (1975).

[Fis86] G. Fischer: *Lineare Algebra*, 9. Auflage, Friedr. Vieweg & Sohn, Braunschweig (1986).

[Fis90] Ø. Fischer, in *Ferromagnetic Materials*, edited by K. H. J. Buschow and E. P. Wohlfarth, North Holland, Amsterdam (1990).

[Fis93] P. J. Fischer, *Zirkularer Magnetischer Röntgendichroismus and den* $L_{2,3}$*-Kanten der* $4f$*-Elemente*, Ph.D. Thesis, Munich University of Technology (1993).

[Fuj94] H. Fujii, S. Ikeda, T. Kimura, S. Arisawa, K. Hirata, H. Kumakura, K. Kadowaki, and K. Togano, Jpn. J. Appl Phys. **33**, L590 (1994).

[Ful66] P. Fulde and K. Maki, Phys. Rev. **141**, 275 (1966).

[Fre72] A. J. Freeman and J. P. Desclaux, Int. J. Magnetism **3**, 311 (1972).

[Gas96] U. Gasser, P. Allenspach, F. Fauth, W. Henggeler, J. Mesot, A. Furrer, S. Rosenkranz, P. Vorderwisch, and M. Buchgeister, Z. Phys. B **101**, 345 (1996).

[Gib85] D. Gibbs, D. E. Moncton, K. L. D'Amico, J. Bohr, B. Grier, Phys. Rev. Lett. **55**, 234 (1985).

[Gib86] D. Gibbs, J. Bohr, J. D. Axe, D. E. Moncton and K. L. D'Amico, Phys. Rev. B **34**, 8182 (1986).

[Gib88] D. Gibbs, D. R. Harshmann, E. D. Isaacs, D. B. McWhan, D. Mills and C. Vettier, Phys. Rev. Lett. **61**, 1241 (1988).

[Gib91] D. Gibbs, G. Grübel, D. R. Harshman, E. D. Isaacs, D. B. McWhan, D. Mills, and C. Vettier, Phys. Rev. B **43**, 5663 (1991).

[Gol94] A. I. Goldman, C. Stassis, P. C. Canfield, J. Zarestky, P. Dervenagas, B. K. Cho, D. C. Johnston and B. Sternlieb, Phys. Rev. B **50**, 9668 (1994).

[Gol97] A. I. Goldman, private communication (1997).

[Gri94] T. E. Grigereit, J. W. Lynn, Q. Huang, A. Santoro, R. J. Cava, J. J. Krajewski, W. F. Peck Jr., Phys. Rev. Lett **73**, 2756 (1994).

[Gru00] G. Grübel *et al.*, (unpublished).

[Gup95] L. C. Gupta, R. Nagarajan, Z. Hossain, C. Mazumdar, S. K. Dhar, C. Godart, C. Levy-Clement, B. D. Padalia, and R. Vijayaraghavan, J. Magn. Magn. Matr. **140-144**, 2053 (1995).

[Gup97] L. C. Gupta, private communication (1997).

[Häm91] K. Hämäläinen, D. P. Siddons, J. B. Hastings, and L. E. Berman, Phys. Rev. Lett. **67**, 2850 (1991).

[Ham94] M. Hamrick, Ph.D. Thesis, Rice University, (1994).

[Han88] J. P. Hannon, G. T. Trammel, M. Blume and D. Gibbs, Phys. Rev. Lett. **61**, 1245 (1988).

[Hel94] G. Helgesen, J. P. Hill, T. R. Thurston, D. Gibbs, J. Kwo, and M. Hong, Phys. Rev. B **50**, 2990 (1994).

[Hel95] G. Helgesen, J. P. Hill, T. R. Thurston, and D. Gibbs, Phys. Rev. B **52**, 9446 (1995).

[Hil95] J. P. Hill, A. Vigilante, D. Gibbs, J. L. Peng and R. L. Greene, Phys. Rev. B **52**, 6575 (1995).

[Hil96a] J. P. Hill, B. Sternlieb, D. Gibbs, C. Detlefs, A. I. Goldman, C. Stassis, B. K. Cho and P. C. Canfield, Phys. Rev. B **53**, 3487 (1996).

[Hil96b] J. P. Hill and D. F. McMorrow, Acta Crystallogr. Sect. A **52**, 236 (1996).

[Hil97] J. P. Hill, C.-C. Kao, and D. F. McMorrow, Phys. Rev. B **55**, 8662 (1997).

[Hut64] M. T. Hutchings, *Point Charge Calculations of Energy Levels of Magnetic Ions in Crystalline Electric Fields*, in F. Seitz and D. Turnbull (eds.), *Solid State Physics, Advances in Research and Applications*, Vol. 16, Academic Press, New York and London (1964).

[Isa89] E. D. Isaacs, D. B. McWhan, C. Peters, G. E. Ice, D. P. Siddons, J. B. Hastings, C. Vettier, and O. Vogt, Phys. Rev. Lett **62**, 1671 (1989).

[Isa95] E. D. Isaacs, P. Zschack, C. L. Broholm, C. Burns, G. Aeppli, A. P. Ramierez, R. W. Erwin, N. Stüchli, and E. Bucher, Phys. Rev. Lett. **75**, 1178 (1995).

[Isl00a] A. H. M. Z. Islam, C. Detlefs, A. I. Goldman, P. C. Canfield, J. P. Hill, L. D. Gibbs, and K. D. Finkelstein, (unpublished).

[Isl00b] A. H. M. Z. Islam, C. Detlefs, A. I. Goldman, P. C. Canfield, J. P. Hill, L. D. Gibbs, A. Zheludev, and T. Vogt, (unpublished).

[Jac75] J. D. Jackson: *Classical Electrodynamics*, Second edition, John Wiley & sons (1975).

[Jen93] J. Jensen and R. A. Cowley, Europhys. Lett. **21**, 705 (1993).

[Jud57] R. B. Judd, Proc. Roy. Soc. **A241**, 414 (1957).

[Kas56] T. Kasuya, Progr. Theor. Phys. (Japan) **16**, 45 (1956).

[Kön96a] H. König, private communication (1996).

[Kön96b] H. König, *Absorption polarisierter Röntgenstrahlung als Probe lokaler Festkörpereigenschaften*, Ph.D. Thesis, European Synchrotron Radiation Facility, Grenoble and Max-Planck-Institut für Festkörperforschung, Stuttgart (1996).

[Kog97] V. G. Kogan, M. Bullock, B. Harmon, P. Miranović, Lj. Dobrosavljević-Grujić, P. L. Gammel and D. J. Bishop, Phys. Rev. B **55**, R8693 (1997).

[Kra30] H. A. Kramers, Konikl. Ned. Akad. Wetenschap., Proc. **33**, 959 (1930).

[Lea62] K. R. Lea, M. J. M. Leask, and W. P. Wolf, J. Phys. Chem. Solids **23**, 1381 (1962).

[Lin95] M. S. Lin, J. H. Sieh, Y. B. You, Y. Y. Hsu, J. W. Chen, S. H. Lin, Y. D. Yau, J. C. Ho, and H. C. Ku, Physica C **249**, 403 (1995).

[Lov84] S. W. Lovesey, *Theory of neutron scattering from condensed matter*, Clarendon Press, Oxford (1984).

[Luo93] Jin Luo, G. T. Trammel and J. P. Hannon, Phys. Rev. Lett. **71**, 287 (1993).

[Luo94] Jin Luo, Ph.D. Thesis, Rice University, (1994).

[Lyn96] J. W. Lynn, Q. Huang, S. K. Sinha, Z. Hossain, L. C. Gupta, R. Nagarajan, and C. Godart, J. Appl. Phys. **79**, 5857 (1996).

[Lyn97] J. W. Lynn, S. Skanthakumar, Q. Huang, S. K. Sinha, Z. Hossain, L. C. Gupta, R. Nagarajan, and C. Godard, Phys. Rev. B **55**, 6584 (1997).

[Lyn00a] J. W. Lynn, J. Alloys Compounds (to be published).

[Mac80] K. Machida, K. Nohura, and T. Masubara, Phys. Rev. Lett. **42**, 918 (1980).

[Map82] M. B. Maple and O. Fischer (eds.), *Superconductivity in Ternary Compounds*, Vols. I and II of *Topics in Current Physics*, Springer, Berlin (1982).

[Mas95] M. E. Massalami, S. L. Bud'ko, B. Giordanengo, and E. M. Baggio-Saitovitch, Physica C **224**, 41 (1995).

[Mat94a] G. Materlik, C. J. Sparks, and K. Fischer (Eds.) *Resonant anomalous x-ray scattering*, North-Holland, Amsterdam (1994).

[Mat94b] L. F. Mattheiss, Phys. Rev. B **49**, 13 279 (1994).

[Mat94c] L. F. Mattheiss, Solid State Comm. **91**, 587 (1994).

[Moo66] H. A. Mook, Phys. Rev. **148**, 495 (1966).

[Mor90] P. Morin and D. Schmitt, in *Ferromagnetic materials*, Vol. 5, eds. K. H. J. Buschow and E. P. Wohlfarth, North-Holland, Amsterdam (1990).

[Mov94] R. Movshovich, M. F. Hundley, J. D. Thomson, P. C. Canfield, B. K. Cho, and A. V. Chubukov, Physica C **230**, 381 (1994).

[Nag94] R. Nagarajan, C. Maxumundar, Z. Hossain, S. K. Dhar, K. V. Golparrishnan, L. C. Gupta, C. Godart, B. D. Padalia and R. Vijazarahgavan, Phys. Rev. Lett **72**, 274 (1994).

[Nam85] K. Namikawa, M. Ando, T. Nakajima, and H. Kawata, J. Phys. Soc. Japan **54**, 4099 (1985).

[Nee32] L. Neel, Ann. Phys. **17**, 64 (1932).

[Pic94] W. E. Pickett and D. J. Singh, Phys. Rev. Lett **72**, 3702 (1994).

[Pla70] P. M. Platzman and N. Tzoar, Phys. Rev. B **2**, 3556 (1970).

[Pra95] K. Prassides, A. Lappas, M. Buchgeister, and P. Verges, Europhys. Lett. **29**, 641 (1995).

[Ram81] T. V. Ramakrishnan and C. M. Varma, Phys. Rev. B **24**, 137 (1981).

[Rat96] K. D. D. Rathnayaka, D. G. Naugle, B. K. Cho and P. C. Canfield, Phys. Rev. B **53**, 5688 (1996).

[Rhe95] J. Y. Rhee, X. Wang and B. N. Harmon, Phys. Rev. B **51**, 15585 (1995).

[Rod93] J. Rodriguez-Carvajal, Physica B **192**, 55 (1993).

[Rud54] M. A. Ruderman and C. Kittel, Phys. Rev. **96**, 99 (1954).

[San94] M. K. Sanyal, D. Gibbs, J. Bohr and M. Wulff, Phys. Rev. B **49**, 1079 (1994).

[She76] R. N. Shelton, R. W. McCallum, and H. Adrian, Bull. Am. Phys. Soc. **21**, 383 (1976).

[She81] G. K. Shenoy, B. D. Dunlap, and F. Y. Fradin (eds.), *Proceedings of the International Conference on Ternary Superconductors*, North-Holland, Amsterdam (1981).

[Shu49] C. G. Shull and J. S. Smart, Phys. Rev. **79**, 1256 (1949).

[Sie94a] T. Siegrist, H. W. Zandbergen, R. J. Cava, J. J. Krajewski and W. F. Peck, Jr., Nature **367**, 254 (1994).

[Sie94b] T. Siegrist, R. J. Cava, J. J. Krajewski, W. F. Peck, Jr., J. Alloys Compounds **216**, 135 (1994).

[Sin82] S. K. Sinha, G. W. Crabtree, D. G. Hinks, and H. A. Mook, Phys. Rev. Lett. **48**, 950 (1982).

[Sin84] S. K. Sinha, H. A. Mook, O. A. Pringle, D. G. Hinks, in *Superconductivity in Magnetic and Exotic Materials*; Proceedings of the 6th Taniguchi International Symposium, Kashikjima, Japan, edited by T. Matsubara and A. Kotani, Springer Series in Solid-State Sciences, Vol. 52, Springer, New York (1984).

[Sin95] S. K. Sinha, J. W. Lynn, T. E. Grigereit, Z. Hossain, L. C. Gupta, R. Nagarajan and C. Godart, Phys. Rev. B **51**, 681 (1995).

[Sta97] C. Stassis, M. Bullock, J. Zarestky, P. Canfield, A. I. Goldman, G. Shirane, and S. M. Shapiro, Phys. Rev. B **55**, R8678 (1997).

[Sta00] C. Stassis and A. I. Goldman, J. Alloys Compounds (to be published).

[Ste97] B. Sternlieb *et al.*, J. Appl. Phys. **81**, 4937 (1997).

[Str96] J. Strempfer, T. Brückel, U. Rütt, J. R. Schneider, K.-D. Liss, and T. Tschentscher, Acta Crystallogr. Sect. A **52**, 438 (1996).

[Ste52] K. W. A. Stevens, *Matrix Elements and Operator Equivalents Connected with the Magnetic Properties of Rare Earth Ions*, Proc. Phys. Soc. Lond. **A65**, 209 (1952).

[Tak96] H. Takeya, T. Hirano, and K. Kadowaki, Physica C **256**, 220 (1996).

[Tem80] D. H. Templeton and L. K. Templeton, Acta Crystallogr. Sect. A **36**, 237 (1980).

[Tho92] B. T. Thole, P. Carra, F. Sette, and G. van der Laan, Phys. Rev. Lett. **68**, 1943 (1992).

[Tin64] M. Tinkham, *Group theory and quantum mechanics*, McGraw-Hill (1964).

[Tom95] C. V. Tomy, M. R. Lees, L. Afalfiz, G. Balakrishnan, and D. McK. Paul, Phys. Rev. B **52**, 9186 (1995).

[Tom96] C. V. Tomy, L. A. Afalfiz, M. R. Lees, J. M. Martin, D. McK Paul, and D. T. Adroja, Phys. Rev. B **53**, 307 (1996).

[Tra53] G. T. Trammel, Phys. Rev. **92**, 1387 (1953).

[Vog95a] T. Vogt, A. Goldman, B. Sternlieb, and C. Stassis, Phys. Rev. Lett **75**, 2628 (1995).

[Vog95b] T. Vogt, C. Stassis, A. Goldman, P. Canfield, and B. Cho, Physica B **215**, 159 (1995).

[Wat95] D. Watson, E. M. Forgan, W. G. Stirling, W. J. Nutall, S. C. Perry, M. M. R. Costa, and D. J. Fort, J. Magn. Magn. Mater. **140-144**, 7434 (1995).

[Wat96a] G. M. Watson, D. Gibbs, G. H. Lander, B. D. Gaulin, L. E. Berman, H. Matzke, and W. Ellis, Phys. Rev. Lett. **77**, 751 (1996).

[Wat96b] G. M. Watson, E. M. Forgan, W. J. Nutall, W. G. Stirling, and D. Fort, Phys. Rev. B **53**, 726 (1996).

[Wig31] E. Wigner, *Gruppentheorie und ihre Anwendung auf die Quantenmechanik der Atomspektren*, Friedr. Vieweg & Sohn, Braunschweig (1931).

[Wil61] M. K. Wilkinson, W. C. Koehler, E. O. Wollan, and J. W. Cable, J. Appl. Phys. **32**, 48S (1961).

[Whi83] R. M. White, *Quantum Theory of Magnetism*, Springer Series in Solid-State Sciences, Vol. 46, Springer, Berlin (1983).

[Yar96] U. Yaron, P. L. Gammel, A. P. Ramirez, D. A. Huse, D. J. Bishop, A. I. Goldman, C. Stassis, P. C. Canfield, K. Mortensen, and M. R. Eskildsen, Nature **382**, 236 (1996).

[Yat96] A. Yatskar, N. K. Budraa, W. P. Beyermann, P. C. Canfield, and S. L. Bud'ko, Phys. Rev. B **54**, R3772 (1996).

[Yos57] K. Yosida, Phys. Rev. **106**, 893 (1957).

[Zan94] H. W. Zandbergen, W. G. Sloof, R. J. Cava, J. J. Krajewski, and W. F. Peck Jr., Physica C **226**, 365 (1994).

[Zar95] J. Zarestky, C. Stassis, A. I. Goldman, P. C. Canfield, P. Dervenagas, B. K. Cho and D. C. Johnston, Phys. Rev. B **51**, 678 (1995).

[Zhe96] A. Zheludev, J. P. Hill, and D. J. Buttrey, Phys. Rev. B **54**, 7216 (1996).

ACKNOWLEDGMENTS

This work would have been impossible without the constant support of my advisor, Alan I. Goldman. His guidance, patience, physical insight and the countless stimulating discussions we have had over the last three years provided the foundation this thesis is build on.

I have also benefited enormously from my frequent discussions with Paul C. Canfield and Bruce N. Harmon. Both of them were always willing to answer even my most stupid questions friendly and patiently. Finally, Bruce was my first contact to the Physics Department in Ames and, is ultimately responsible for my coming here.

The experimental part of this thesis would have been impossible without the help of John P. Hill and Doon Gibbs of the Physics Department of Brookhaven National Lab. The friendly work atmosphere, their knowledge and the excellent condition of their equipment will always make a beamtime at X22C a pleasant experience.

I would also like to thank my past and current office and lab mates, Stefan Kycia, A. H. M. Zahirul Islam, Tianqu Gu, and Brian J. Hostetter, for their help inside and outside the lab and for the many discussions about physics, computers, physicists and other life forms.

I am also indebted to many physicists and non-physicist at the ISU Physics Department and Ames Lab, far too many actually to list every one of them here.

Finally, I wish to thank my family for their support and my girlfriend, Maria Rosa Asenjo, for enduring life with a physicist and also — on the frequent occasion of beam-

times — for enduring life without a physicist.

This work was performed at Ames Laboratory under Contract No. W-7405-Eng-82 with the U.S. Department of Energy. The work at Brookhaven National Laboratory was carried out under contract No. DE-AC02-76CH00016, Division of Materials Science, U.S. Department of Energy. The United States government has assigned the DOE Report Number IS-T 1821 to this thesis.

M98004646

Report Number (14) IS-T--1821

Publ. Date (11) 19981008
Sponsor Code (18) DOE/ER , XF
UC Category (19) UC-400 , DOE/ER

DOE